

NATIONAL INSTITUTE FOR FUSION SCIENCE

Frontier of Advanced Pulsed Power Technology
and its Application to Plasma and Particle Beam

Edited by Hiroaki Ito and Tetsuo Ozaki

(Received - Sep. 28. 2021)

NIFS-PROC-121

Nov. 08, 2021

This report was prepared as a preprint of work performed as a collaboration research of the National Institute for Fusion Science (NIFS) of Japan. The views presented here are solely those of the authors. This document is intended for information only and may be published in a journal after some rearrangement of its contents in the future.

Inquiries about copyright should be addressed to the NIFS Library, National Institute for Fusion Science, 322-6 Oroshi-cho, Toki-shi, Gifu-ken 509-5292 JAPAN.

E-mail: tosho@nifs.ac.jp

<Notice about copyright>

NIFS authorized Japan Academic Association For Copyright Clearance (JAC) to license our reproduction rights and reuse rights of copyrighted works. If you wish to obtain permissions of these rights, please refer to the homepage of JAC (<http://jaacc.org/eng/>) and confirm appropriate organizations to request permission.

Frontier of Advanced Pulsed Power Technology and its Application to Plasma and Particle Beam

Edited by Hiroaki Ito and Tetsuo Ozaki

January 7-8, 2021
National Institute for Fusion Science
Toki, Gifu, Japan

Abstract

The papers presented at the symposium on “Frontier of Advanced Pulsed Power Technology and its Application to Plasma and Particle Beam” held on January 7-8, 2021 at the virtual conference are collected. The papers in this proceeding reflect the present status and recent progress in the experimental and theoretical works on high power particle beams and high energy density plasmas produced by pulsed power technology.

Keyword: high power particle beam, high energy density plasma, pulsed power technology, z-pinch, x-ray, inertial fusion, pulsed discharge, high power electromagnetic wave, material processing, biological application

Some figures are in color only CD-ROM (PDF).

Preface

The symposium entitled “Frontier of Advanced Pulsed Power Technology and its Application to Plasma and Particle Beam” was organized as a part of the General Collaborative Research of National Institute for Fusion Science (NIFS) and held on January 7-8, 2021 at the virtual conference. During the 2 days of symposium, 26 papers were presented. The total number of participants was 68 including students and researchers from universities and a company.

The purpose of the symposium has been to provide a forum to discuss important technical developments, important applications, increased understandings, new trends and the future in the field of high power particle beams, high energy density plasmas, electromagnetic wave source and inertial fusion, etc. using the pulsed power technology. the pulsed power technology and its application. Therefore, the papers in this proceeding reflect the present status and progress in the research fields related to the pulsed power technology in Japan. It is my pleasure if the symposium contributed to the progress in the science and technology using pulsed power technology and could provide some kind of opportunity for all participants, especially for young scientists.

We would like to express our sincere thanks to all of the participants, authors and the staff of NIFS.

Hiroaki Ito
University of Toyama

Tetsuo Ozaki
National Institute for Fusion Science

List of Participants

K. Takahashi	Iwate University
S. Abe	Iwate University
R. Saito	Iwate University
K. Uchimidou	Iwate University
M. Sato	Gunma University
R. Namiki	Gunma University
K. Ono	Gunma University
R. Matsuo	Gunma University
T. Memichi	Gunma University
S. Kawata	Utsunomiya University
K. Takayama	High Energy Accelerator Research Organization
K. Okamura	High Energy Accelerator Research Organization
J. Hasegawa	Tokyo Institute of Technology
T. Kawamura	Tokyo Institute of Technology
T. Jinnai	Tokyo Institute of Technology
K. Matsuda	Tokyo Institute of Technology
G. Imada	Niigata Institute of Technology
W. Jiang	Nagaoka University of Technology
T. Sugai	Nagaoka University of Technology
F. Yu	Nagaoka University of Technology
P. N. Thanh	Nagaoka University of Technology
S. Yijie	Nagaoka University of Technology
K. Inui	Nagaoka University of Technology
M. Ohta	Nagaoka University of Technology
H. Okazaki	Nagaoka University of Technology
S. Matsumoto	Nagaoka University of Technology
N. H. Phat	Nagaoka University of Technology
Z. Longyu	Nagaoka University of Technology
R. Xiaojing	Nagaoka University of Technology
K. Nagao	Nagaoka University of Technology
Y. Junxiang	Nagaoka University of Technology
Q. Q. Qian	Nagaoka University of Technology
Y. Bingyu	Nagaoka University of Technology

T. Ishida	Nagaoka University of Technology
A. Kamada	Nagaoka University of Technology
H. Kuno	Nagaoka University of Technology
T. Deguchi	Nagaoka University of Technology
H. Suzuki	Nagaoka University of Technology
Y. Xiaohang	Nagaoka University of Technology
G. Ziyi	Nagaoka University of Technology
L. Yuheng	Nagaoka University of Technology
T. Kikuchi	Nagaoka University of Technology
T. Sasaki	Nagaoka University of Technology
K. Takahashi	Nagaoka University of Technology
N. Watanabe	Nagaoka University of Technology
N. Suzutani	Nagaoka University of Technology
L. Zhehao	Nagaoka University of Technology
S. Watanabe	Nagaoka University of Technology
T. Sugai	Nagaoka University of Technology
H. Ito	University of Toyama
T. Takezaki	University of Toyama
K. Ishibashi	University of Toyama
Y. Sagano	University of Toyama
R. Tanaka	University of Toyama
K. Osawa	University of Toyama
S. Kato	University of Toyama
M. Takao	University of Toyama
T. Yamada	University of Toyama
R. Hasegawa	University of Toyama
Y. Tanaka	University of Toyama
Y. Fukada	University of Toyama
T. Nunome	University of Toyama
T. Oguchi	University of Toyama
R. Ando	Kanazawa University
Y. Soga	Kanazawa University
H. Ishi	Kanazawa University
A. Tokuchi	Pulsed Power Japan laboratory Ltd.
T. Ozaki	National Institute for Fusion Science

Contents

1. Development of Compact Resonant High Voltage Pulse Generator Driven by SiC-MOSFET and Its Uses for Discharge Generation
Ryo Saito, Katsuyuki Takahashi, Koichi Takaki (Iwate University), Tatsuya Terazawa (Energy support Corporation)
2. Characterization and Improvement of LTD Module for Excimer Laser Excitation using SiC-MOSFET
Yuki Okazaki, Yan Bingyu, Tatuya Deguti, Taichi Sugai (Nagaoka University of Technology), Akira Tokuchi (Pulsed Power Laboratory Ltd.), Weihua Jiang (Nagaoka University of Technology)
3. Measuring active species by waveform control in water treatment equipment using pulse discharge
Phung Nhat Thanh, Sugai Taiti, Weihua Jiang (Nagaoka University of Technology)
4. Effect of Applied Electric Field Direction on Material Irradiation of Laminar Atmospheric Pressure Plasma jet with Double Coaxial Tube Structure
Kazuto Ishibashi, Hiroaki Ito (University of Toyama)
5. Review of the Massive Ion Inertial Fusion Driver for Future Inertial Fusion and our Understanding of Fusion Technology
K. Takayama, T. Adachi, T. Kawakubo, K. Okamura (High Energy Accelerator Research Organization), Y. Yuri (National Institutes for Quantum and Radiological Science and Technology, Takasaki Advanced Radiation Research Institute), J. Hasegawa, K. Horioka (Tokyo Institute of Technology), T. Kikuchi, T. Sasaki, and K. Takahashi (Nagaoka University of Technology)
6. Characteristics of pulsed ion beam emitted from plasma focus device with different anode shapes
Yuto Sagano, Takuho Yamada, Takanori Nunome, Hiroaki Ito, Taichi Takezaki (University of Toyama)
7. One-dimensional PIC-MCC Analysis of Inertial Electrostatic Confinement Plasma
Kazuhiro Matsuda, Jun Hasegawa (Tokyo Institute of Technology)
8. Numerical simulation for behavior of multi-ion-species plasma in perpendicular magnetic field
Taichi Takezaki, Kyohei Osawa, Seigo Kato, Takuya Oguchi (University of Toyama), Kazumasa Takahashi, Toru Sasaki, Takashi Kikuchi (Nagaoka University of Technology), and Hiroaki Ito (University of Toyama)
9. Relaxation Process of Electron Beam Injected into a Malmberg–Penning Trap
Ishii Hiroshi, Yukihiro Soga (Kanazawa University), Youngsoo Park (National Institute of Technology, Anan College), Nozomi Suzutani, Takashi Kikuchi (Nagaoka University of Technology)
10. Analysis of cluster ions directly generated from laser ablation plasma cooled in ambient helium gas

Takuma Jinnai, Jun Hasegawa (Tokyo Institute of Technology)

11. Influence of Frequency on Electrostatic Potential with Space Charges Generated by Rectangular AC Corona Discharges
Kakeru Uchimido, Katsuyuki Takahashi, Koichi Takaki (Iwate University), Nozomi Takeuchi (Tokyo Institute of Technology), Shinichi Yamaguchi, Hidemi Nagata (Shishido Electrostatic, Ltd.)
12. Comparison of Plasma Characteristics of High-Power Pulsed Sputtering (HPPS) Glow Discharge and Hollow-Cathode Discharge
Shoki Abe, Katsuyuki Takahashi, Seiji Mukaigawa, Koichi Takaki, Ken Yukimura (Iwate University)
13. Evaluation of Electron Beam Characteristics using a Virtual Cathode Oscillator
Michihiro Ohta, Kentaro Inui, Kazuki Nagao, Taichi Sugai, Weihua Jiang (Nagaoka University of Technology)
14. Electron Beam Shape Dependence of Output Microwave Characteristics in Reflex Triode Virtual Cathode Oscillator
Ryota Tanaka, Yusei Fukada, Hiroaki Ito (University of Toyama)
15. Analysis of Observation Signal of Microwave Discharge in Rectangular Waveguide
T. Sugai (Nagaoka University of Technology), Z. Shaw, J. Dickens, A. Neuber (Texas Tech University)
16. Droop Compensation in Marx generator
Shounosuke Matsumoto, Weihua Jiang, Taichi Sugai (Nagaoka University of Technology), Akira Tokuchi (Pulsed Power Laboratory Ltd.)
17. Development and evaluation of bipolar Marx circuits
Nguyen Huu Phat, Akira Kamada, Xiaojing Ren, Taichi Sugai (Nagaoka University of Technology), Akira Tokuchi (Pulsed Power Laboratory Ltd.), Weihua Jiang (Nagaoka University of Technology)

Development of Compact Resonant High Voltage Pulse Generator Driven by SiC-MOSFET and Its Uses for Discharge Generation

Ryo SAITO, Katsuyuki TAKAHASHI*, Koichi TAKAKI*, Tatsuya TERAZAWA**

Faculty of Science and Engineering, Iwate University

**Agri-Innovation Center, Iwate University*

***Energy support Corporation*

ABSTRACT

A leakage inductance resonance (LIR) high voltage pulse generator driven by SiC-MOSFET with a low on-resistance and a high blocking voltage is developed. A transformer is used to generate high voltage pulses. LC resonant circuit is composed by the leakage inductance in the transformer winding and the stray capacitance in the secondary circuit. The maximum output voltage and the full width at half maximum are 13.6 kV and 94 ns, respectively, at an input voltage of 1 kV, a load resistance of 10 M Ω , and a turns ratio of 1:7. The maximum energy transfer efficiency is 91% of the input energy with a load resistance of 2 k Ω . The pulse voltage is applied to a wire to wire electrode to generate streamer discharges, and the ozone production efficiency is evaluated. A thin wire with a diameter of 0.05 mm is used as the wire electrode. The ozone production efficiency increases with increasing gap distance, and its maximum value is 67 g/kWh. The results show the LIR pulse generator has a potential to realize a highly efficient and compact radical generator.

Keywords

Pulsed power, Silicon Carbide, MOSFET, Streamer discharge, Ozone

1. Introduction

A non-thermal plasma produces various kind of reactive oxygen species and has been studied for its promising applications such as purification of exhaust gas by removing nitrogen oxides^[1], keeping freshness of fruit and vegetables by removing ethylene gas^[2] and sterilization treatment^[3]. O radical and ozone are oxygen species and mainly contribute these applications as oxidants^[4]. Production efficiency of these active species is affected by pulse width of applied voltages. Short pulse discharges can reduce the energy loss associated with gas heating and enable highly efficient active species production^[5].

One of the most important components of the pulsed

power generator is a switch. Generally, spark gap switches have been used, but it is difficult to implement in application fields because of their rapid deterioration, operation instability and large size. To solve this problem, semiconductor power devices have been used as the switches. Bipolar power semiconductor devices such as IGBTs and SI-Thyristors can achieve high capacity, but inferior in high-speed operation^[6]. Compared to them, MOSFETs are relatively small capacity and high-speed device. However, realization of further performance is extremely difficult based on the physical property of the conventional silicon (Si) material. Silicon carbide (SiC) has been attracting much attention as a high-performance material

capacitor i_C , the current flows the primary circuit i_{L1} and the output current i_O are measured using a current transformer (Bergoz, CT-D1.0-B). The voltage of an energy storage capacitor v_C , the drain source voltage v_{DS} and the output voltage v_O are measured using voltage probes (Tektronix P6015A).

Two thin stainless wires (SUS316L) with a diameter of 0.05 mm and a length of 40 mm are parallelly placed and used as the high voltage and grounded electrodes. The gap distance varies at 4, 8 and 12 mm. The pulse repetition rate is 830 pps. The efficiency of ozone production by discharge is evaluated. To measure ozone produced by discharge, the electrode is placed in a 0.9 L sealed plastic container. The air inside of the container is stirred by a fan. Ozone concentration is measured using an ozone detector tube (GASTEC, No. 18M) one minute after the discharge operation.

3. Results and Discussion

3.1 Evaluation of LIR pulsed power generator characteristics

Fig. 3 shows the typical waveforms of voltage and current for each part of LIR pulsed power generator when V_{DD} is 1 kV and the load resistance R_L is 10 M Ω . The maximum value and the full width at half maximum of v_O are 13.6 kV and 94 ns, respectively. This approximately satisfies eq. (1).

Fig. 4 shows the maximum value of v_O ($v_{O(MAX)}$) as a function of R_L . $v_{O(MAX)}$ decreases with decreasing R_L . This is because the resonant current flowing in C_S shown in Fig. 2 divided to R_L .

Fig. 5 shows the energy transfer efficiency η to the output side as a function of R_L . The η is given by following equations:

$$u_1 = \int v_C \cdot i_C dt \quad (2)$$

$$u_O = \int v_O \cdot i_O dt \quad (3)$$

$$\eta = u_O / u_1 \quad (4)$$

where u_1 and u_O is the energy consumed in the primary circuit and that in the load resistor, respectively. When

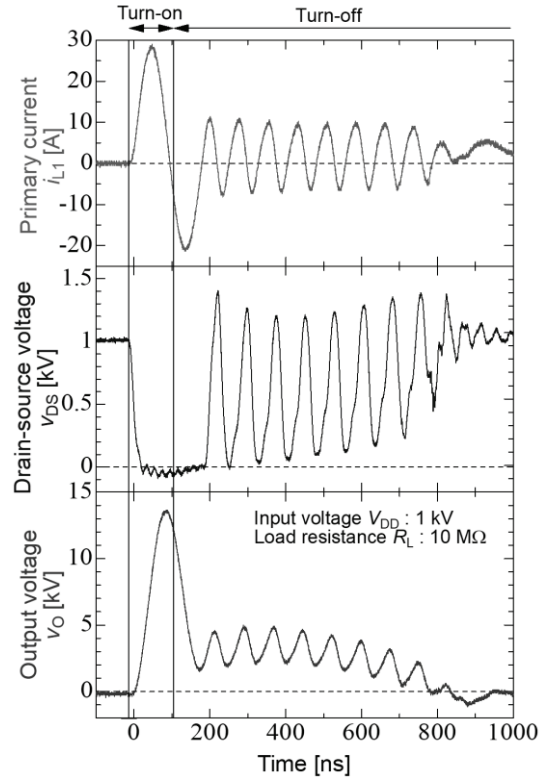


Fig. 3 Typical waveforms of voltage and current for each parts of leakage inductance resonance pulse generator

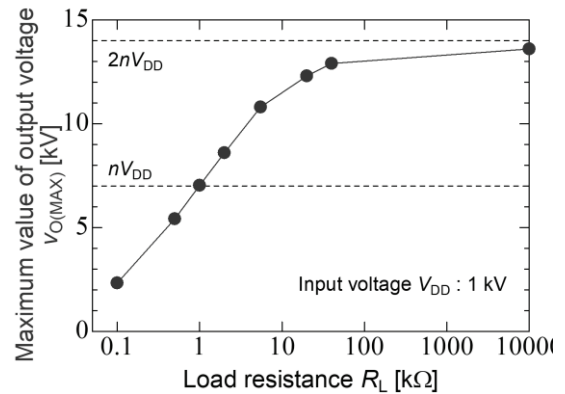


Fig. 4 Maximum value of output voltage as a function of load resistance

the R_L is 2 k Ω , the η has a maximum value of 91% and the u_O is 4.5 mJ, because the impedances of primary side and secondary side are matched.

The size of the LIR pulsed generator is 130 mm in width, 70 mm in depth and 90 mm in height. This circuit size can be reduced to 100 mm in width, 50 mm in depth and 80 mm in height, by designing the driver

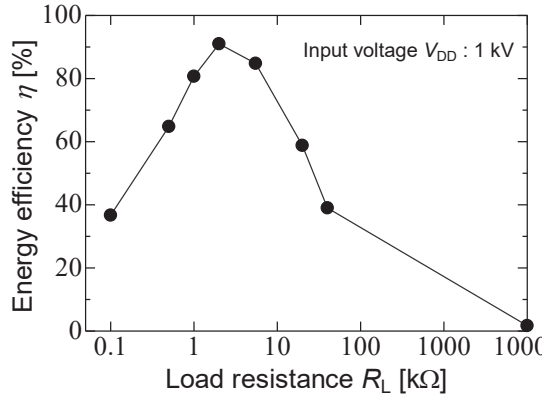


Fig. 5 Energy transfer efficiency to output side as a function of load resistance

circuit on a printed circuit board using smaller IC packages.

3.2 Evaluation of wire-to-wire discharge using LIR pulsed power generator

Fig. 6 shows a typical image of the discharge when the gap distance is 4 mm. Fig. 7 shows the waveforms of the output voltage, the discharge current and the electrode impedance during pulsed discharge when the gap distance is 4 mm. The maximum value and the full width at half maximum of v_O are 8.0 kV and 89 ns, respectively. The maximum value of the discharge current is 1.4 A. The electrode impedance decreased rapidly with the rise of the discharge current and reached about 5 kΩ, which shows that the discharge phase shifts from streamer discharge to glow-like discharge rapidly^[10]. The output voltage rapidly decreases when the electrode impedance decreases with discharge initiation, which contribute to prevention of a transition into spark discharge.

Fig. 8 shows the maximum value of the output current ($i_{O(MAX)}$) as a function of $v_{O(MAX)}$ for different gap distances. $i_{O(MAX)}$ increases with increasing $v_{O(MAX)}$. When the gap distance is 4 mm and the $v_{O(MAX)}$ is 8.5 kV, the $i_{O(MAX)}$ is 2.1 A. When the applied voltage higher than 8.5 kV, spark discharge occurs. The appearance of discharges and the waveform of the discharge current are not affected by a blown air with an air velocity of 20 m/s. Fig. 9 shows the ozone

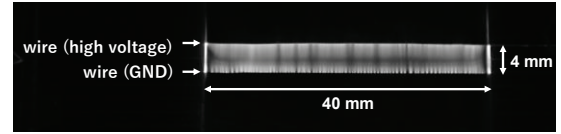


Fig. 6 Typical image of wire-to-wire discharge

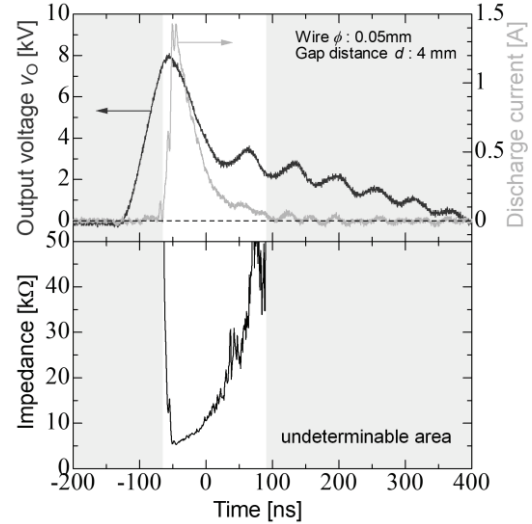


Fig. 7 Typical waveforms of output voltage, discharge current and electrode impedance during discharge

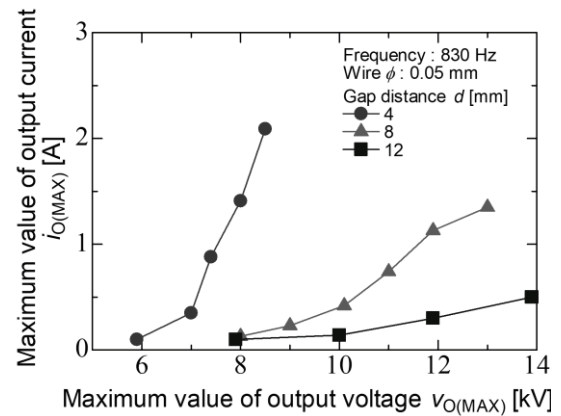


Fig. 8 Maximum value of output current as a function of maximum value of output voltage for different gap distances.

production efficiency as a function of input energy for different gap distances. The ozone production efficiency increases with increasing the gap distance. When the gap distance is 12 mm and the input energy is 0.10 W, the ozone production efficiency has a maximum value of 67 g/kWh.

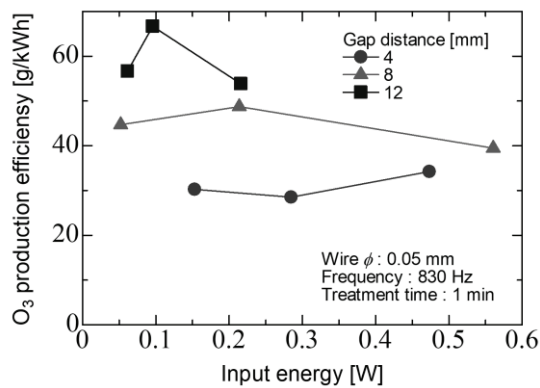


Fig. 9 Ozone production efficiency as a function of input energy for different gap distances

4. Conclusions

Electrical characteristics of the LIR pulsed generator using the resonance phenomenon between the leakage inductance in a transformer winding and the stray capacitance in the secondary circuit are evaluated. The output voltage of 13.6 kV and full width half maximum of 94 ns are obtained with an input voltage of 1 kV and a load resistance of 10 M Ω . When a load resistance is 2 kW, the energy transfer efficiency has a maximum value of 91% and the output energy is 4.5mJ. When pulsed discharges are generated at wire-to-wire electrodes using the LIR pulsed generator, glow like discharges are observed. The ozone production efficiency increased with increasing the gap distance, and its maximum value is 67 g/kWh when the gap distance is 12mm.

Acknowledgments

Part of this work has been supported by Adaptable and Seamless Technology Transfer Program through Target-driven R&D (A-STEP) Tryout, Grant Number JPMJTM20AM.

References

[1] Y. S. Mok *et al.*, “Positive pulsed corona discharge process for simultaneous removal of SO and NO_x from iron-ore sintering flue gas”, *IEEE Trans. Plasma Sci.*, **27**, 4, pp. 1188–1196 (1999).
 [2] E.A.Filimonova *et al.*, “Simulation of Ethylene

Conversion Initiated by a Streamer Corona in an Air Flow”, *Plasma Phys. Reports.*, **27**, 8, pp.708-714 (2001).

[3] D. Dobroynin *et al.*, “Inactivation of bacteria using dc corona discharge: role of ions and humidity”, *New J Phys.*, **13**, 10, pp. 1367-2630 (2011).
 [4] K. Takahashi *et al.*, “Influence of Pulse Width on Radical Production in ns-pulsed Discharge Reactor”, *IEEJ. Trans. FM.*, **138**, 3, pp. 84-90 (2018).
 [5] R. Ono *et al.*, “Effect of pulse width on the production of radicals and excited species in a pulsed positive corona discharge”, *J. Phys. D: Appl. Phys.*, **44**, 48, pp. 1-14 (2011).
 [6] G. Wang *et al.*, “Performance comparison of 1200V 100A SiC MOSFET and 1200V 100A silicon IGBT”, *IEEE Energy Conversion Congress and Exposition* (2013).
 [7] M. Bhatnagar *et al.*, “Comparison of 6H-SiC, and 3C-SiC, and Si for Power Devices”, *IEEE Trans. Electron Devices*, **40**, 3, pp. 645-655 (1993).
 [8] J. Mankowski *et al.*, “A Review of Short Pulse Generator Technology”, *IEEE Trans. Plasma Sci.*, **28**, 1, pp. 102-108 (2000).
 [9] N. Y. Babaeva *et al.*, “Two-Dimensional Modeling of Positive Streamer”, *IEEE Trans. Plasma Sci.*, **26**, 1, pp. 41-45 (1998).
 [10] W. J. M. Samaranayake *et al.*, “Pulsed Streamer Discharge Characteristics of Ozone Production in Dry Air”, *IEEE Trans. Dielectrics Electrical Insulation*, **7**, 2, pp. 254-260 (2000).

Characterization and improvement of LTD module for excimer laser excitation using SiC-MOSFET

Okazaki Yuki, Yan Bingyu, Deguti Tatuya, Sugai Taichi, Tokuti Akira* and Weihua Jiang

Extreme Energy Density Research Institute, Nagaoka University of Technology.

** Pulsed Power Japan Laboratory Ltd.*

ABSTRACT

An excimer laser is a type of gas laser, and a pulse power supply is used for its oscillation. The purpose of this study is to develop and improve a pulsed power supply for excimer laser excitation. The LTD method is used as the power supply method. The problem with conventional LTD is that the output current is insufficient. Therefore, in this research, the switch was changed from Si-MOSFET to SiC-MOSFET, and the module was designed according to the laser device. As a result, we were able to obtain an output current of 16.7 kA, which exceeds the output of the conventional LTD.

Keywords

pulsed power, power semiconductor device, excimer laser, MOSFET, LTD(Linear Transformer Driver)

1. Introduction

1.1 Pulsed power

Pulsed power is the technic that compresses or superimposes energy in one time to obtain a large output instantaneously. Figure 1 shows an overview of pulse power.

1.2 Excimer laser

An excimer laser is a laser that uses a halogen and a rare gas called excimer that are temporarily converted into molecules by excitation. Rare gas and halogen, which are normally monoatomic molecules, are excited to temporarily become diatomic molecules. This is called excimer. An excimer laser is a laser that emits light when the excimer returns to the ground state. The features of excimer lasers are short wavelength, high output, and high efficiency. Although excitation methods include discharge excitation and electron beam excitation, discharge excitation by LTD is assumed in this research.

1.3 LTD(Linear Transformer Driver)

LTD (Linear Transformer Driver) is one of the methods to obtain a pulsed power. Pulsed power is obtained by inductively superimposing voltage pulses.

The features of LTD are as follows.

- Simple structure and easy to modularize
- Each module is grounded and the potential is stable.
- There is no upper limit to the output voltage
- Output waveform can be controlled
- Maximum current is limited by switch performance

Application fields of LTD include accelerator power supply and laser power supply. Figure 2 shows the equivalent circuit of LTD.

2. Purpose of research

2.1 Conventional problems

The problem with conventional excimer laser excitation LTD power supplies is that the output current is insufficient. Since the current was insufficient with the conventional circular LTD, it was necessary to connect two conventional circular LTDs in parallel in order to obtain sufficient current to oscillate the excimer laser.

2.2 Improvement points

In order to improve these problems, we made two improvements in this study. The switch was changed

from Si-MOSFET to SiC-MOSFET to increase the current. In addition, the shape of the LTD module has been changed from a circular shape to a race track shape to accommodate the laser chamber shape. Figure 3 and 4 show external views of a single substrate and a stack of substrates, respectively.

2.3 Constitution of RT-LTD

The single- stage of the RT module is configured to combine two U-shaped LTD boards and share one RT-shaped magnetic core. Figure 5 shows the configuration of a single stage RT-LTD module. The LTD power supply consists of stacking these modules.

3. Experimental Setup

3.1 Experiment contents

The experiment was carried out under three conditions: the output to the pseudo load resistor of the RT-LTD substrate alone, the output to the pseudo load resistor in the stacked state, and the output to the laser chamber in the stacked state.

3.2 Experimental conditions

3.2.1 Output of the board alone

The operating voltage of the switch was 18-30V, the charging voltage to the capacitor was 200 V to 800 V, the command pulse width was 200ns, and the load resistance was 0.125 Ω .

3.2.2 Output to pseudo load resistor in stacked state

Initially, the output voltage was measured at 2.5 Ω of the load resistor when the number of stack stages was 24, the operating voltage of the switch was 20, 26, and 30 V, the charging voltage to the capacitor was 800 V, and the command pulse width was 100 ns. Then, the output current was measured at 0.3125 Ω of the load resistor when the number of stack stages was 24, the operating voltage of the switch was 30 V, the charging voltage to the capacitor was 100-300 V, and the command pulse width was 100ns.

3.2.3 Output to the laser chamber in a stacked state

The output voltage was measured with 24 stack stages, a switch operating voltage of 20-30 V, a capacitor charging voltage of 900-1000 V, a command pulse width of 80 ns, chamber medium air, and chamber air pressure of 0.2-0.3 atm.

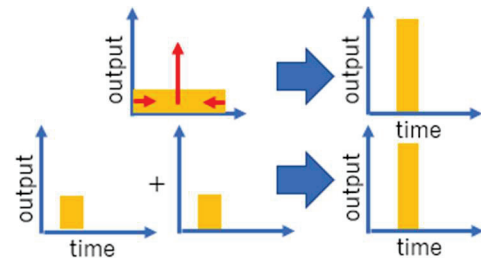


Fig. 1 Image of pulse power

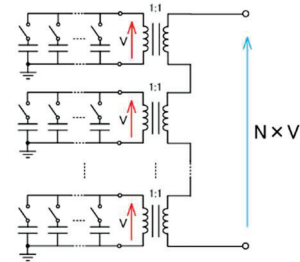


Fig. 2 LTD equivalent circuit

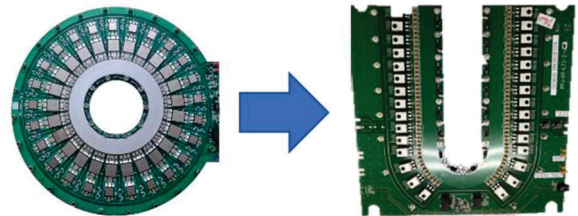


Fig. 3 Conventional LTD and RT- LTD

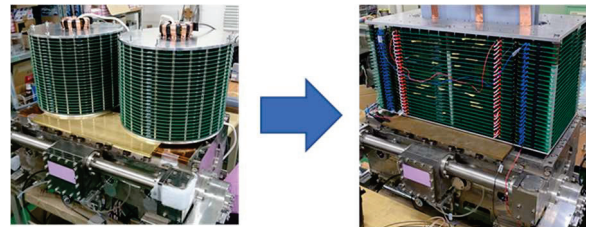


Fig. 4 Conventional LTD and RT- LTD(Stack)

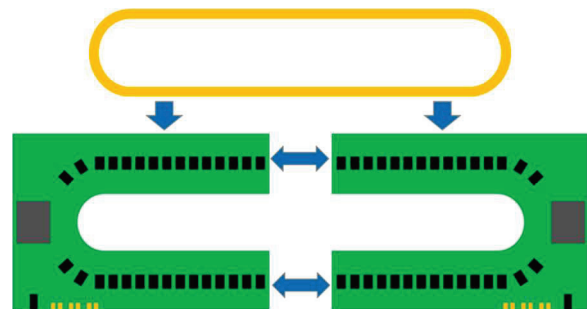


Fig. 5 RT-LTD module configuration

4. Results and Discussion

4.1 Output of the board alone

Figure 6 shows the output voltage waveform of the substrate alone. When charging 800 V, the maximum voltage output is 690 V, which is 86% of 800 V. We also confirmed that the higher the operating gate voltage of the SW is, the higher the maximum voltage is, even with the same pulse width command.

4.2 Output to pseudo load resistor in stacked state

Figure 7 shows the output voltage waveform in stacked state at 2.5Ω of the load resistor. Figure 8 shows the output current waveform in stacked state at 0.3125Ω of the load resistor.

When charging 800 V with V_{gs} 30 V, a maximum voltage of 17.1 kV was obtained at 2.5Ω of the load resistance. Also, as with the result of the board alone, it was confirmed that the higher the gate voltage of the SW is, the higher the maximum voltage is, even with the same command pulse width. Regarding the maximum current at 0.3125Ω of the load resistor, the maximum current was 16.7 kA when charging 300 V.

4.3 Output to the laser chamber in a stacked state

Figure 9 and 10 show the output waveform to the laser chamber in a 24-stage stack when charging 900 V and 1000V, respectively. Figure 11 shows the comparison of output waveforms to the laser chamber at 0.2 atm and 0.3 atm.

As with the output to the load resistor, it was confirmed that the higher the gate voltage of the SW is, the faster the current rise is and the larger the maximum current is, which is consistent with the characteristics of the switch.

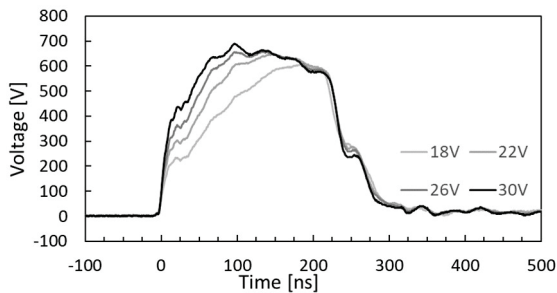


Fig. 6 Output voltage waveform of the board alone

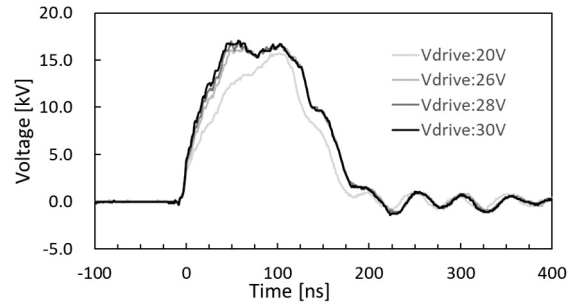


Fig. 7 Output voltage waveform to pseudo load

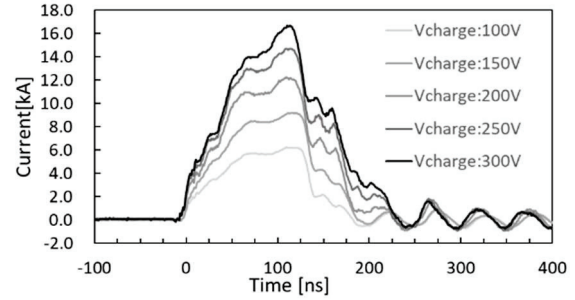


Fig. 8 Output current waveform to pseudo load resistor in a 24-stage stack

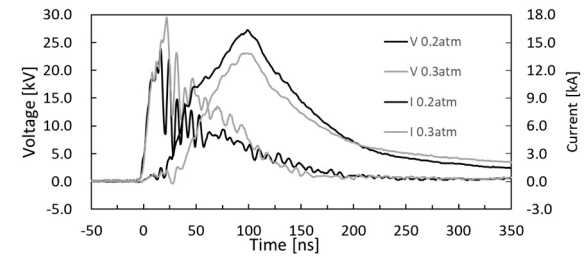


Fig. 9 Output waveform to the laser chamber in a 24-stage stack when charging 900 V

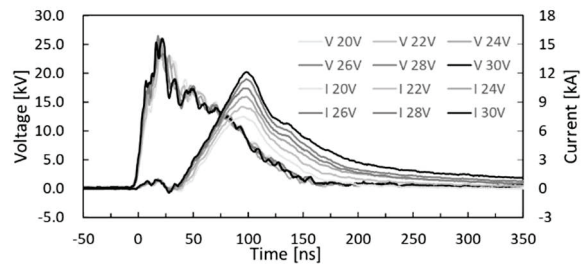


Fig. 10 Output waveform to the laser chamber in a 24-stage stack when charging 1000 V

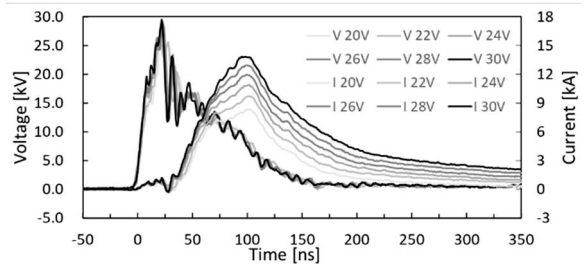


Fig. 11 Comparison of output voltage waveform to laser chamber in 24-stage stack at 0.2 atm and 0.3 atm

As with the output to the load resistor, it was confirmed that the higher the gate voltage of the SW is, the faster the current rise is and the larger the maximum current is, which is consistent with the characteristics of the switch.

When charging at 1000 V, where more current flows, the current waveform has a characteristic that the slope changes in the middle, and this characteristic seems to appear when large current flows. Whether this is due to the characteristics of the switch or the medium and other condition of the chamber will be analyzed in the future to investigate the cause.

5. Conclusions

The characteristics of the new LTD module designed according to the load shape were evaluated, and the following results were obtained.

1. Characteristics of resistive load

- Maximum voltage: 17.1 kV (89% of 19.2 kV (24x2x800 V))
- Maximum current: 16.7 kA (117% of 14.22 kA (30x2x237 A))

2. Characteristics under chamber load

- Maximum voltage: 29.5 kV (0.3 atm, Vdrive: 30 V, Vcharge: 1000 V)
- Maximum current: 16.16 kA (0.2 atm, Vdrive: 30 V, Vcharge: 1000 V)

It was confirmed that the maximum current increased from the past. In the future, we will check the output by controlling the waveform, the effect of equalizing the electric field applied to the chamber, and the discharge form in the laser chamber.

References

- [1] Maeda Mituo., "Excimer Laser", Academic Publishing Center,1993.

Measuring active species by waveform control in water treatment equipment using pulse discharge

Phung Nhat Thanh, Taichi Sugai, Weihua Jiang

Nagaoka University of Technology (1603-1 Kamitomioka, Nagaoka Niigata, 940-2188, Japan)

ABSTRACT

The effect of waveform control of pulse discharge on producing active species (Ozone) in water treatment equipment at atmospheric pressure is performed in this study. The concentration of ozone is measured by using ozone monitor connected with water treatment equipment. According to the previous studies, when the pulse width is lengthened, there is more loss at a latter part of a pulse. To confirm it, the peak voltage at a latter part of a pulse is lowered, and ozone concentration is measured for each case. From the results of this experiment, it is shown that the latter part of pulse discharge is inefficient for producing ozone. In addition, an effect of interval between two pulses is also investigated in this study for optimization of pulse power characteristics for producing ozone in water treatment equipment. It is shown that increasing interval between two pulses led to increasing energy efficiency in producing ozone. Therefore, shortening pulse width and lengthening the interval between two pulses is more efficient in production of ozone in water treatment equipment at atmospheric pressure.

Keywords

Ozone, Water treatment, Pulse power, Atmospheric pressure, Pulse width, Interval, Voltage control, Plasma

1. Introduction

Every shape and rising time of applied pulsed high-voltage effect mainly to efficiency of active species (OH radical and ozone) production and water treatment, so investigation of influences of pulse waveforms and rising time of applied pulsed voltage are very necessary for optimizing plasma-based water treatment system and active species producing process. In the previous studies for the plasma-based active species production, effects of pulse width, peak voltage and repetition rate of pulsed voltage have been investigated and confirmed in experiments [1]-[2]. According to these studies, the increase of pulse width and peak voltage will lead to producing larger amount of ozone. However, with too long pulse width and high peak voltage lead to lowering energy efficiency of producing ozone based on plasma discharge in atmospheric pressure. In addition, experiments from [2] has shown that latter part of long pulse discharge lowers the energy efficiency for producing active species based on plasma discharge

in atmospheric pressure.

From mentioned above previous studies, it is concluded that latter part of long pulse width with different average electric power will lower the energy efficiency for producing active species. However, the effect of latter part of long pulse with approximately similar electric power has not been investigated, so we conduct an experiment with waveform as Fig. 1(a) first in this study.

After that, an effect of interval between pulses on producing ozone is investigated. Ozone produced from the first pulse discharge may be decomposed by other active species which are also produced by high-voltage pulse discharge. And the interval between two pulses is expected that effect this ozone decomposing process. To confirm it, we conduct experiment with lots of different pulse interval with waveform as Fig. 1(b) in the next part of this study.

2. Experimental Setup

As shown in Fig. 2, the water treatment system is composed of a reactor module and water tank. We

used LTD (Linear Transformer Driver) system as pulsed power generator in our experiments.

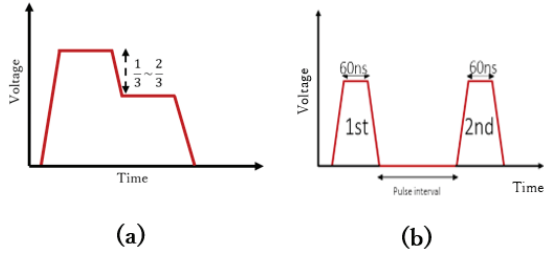


Fig. 1. Outline of waveforms generated by LTD system.

- (a) Two-step waveform with lower part.
- (b) Double-pulses waveform with interval.

Our solid-state LTD system was used to generate high-voltage pulse with complex waveforms which have not been able to be generated before due to limitation of normal pulsed power generators. Operation principles, structure and specification of the LTD system, which is used in these experiments, have been described detailly in [3]-[4]. The number of stacked LTD modules was twenty-three.

In the reactor module of water treatment system, we have wire-to-cylinder coaxial electrodes installed in the acrylic cylinder, with an inner diameter of 40 mm. The wire electrode is made of stainless-steel wire (diameter = 0.28 mm), and the cylindrical electrode is made of stainless-steel wire mesh.

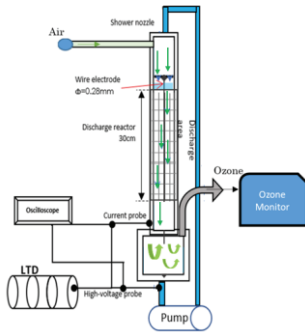


Fig. 2. Draft of water treatment system.

By using LTD system, positive pulsed voltage is applied to the wire electrode in the reactor and the cylindrical electrode is grounded to generate the pulsed streamer discharge. Air is pumped into the water treatment system with 16.5 L/min flow rate to increase pressure in reactor module and produced

ozone can flow out of the water treatment system. The gas outlet pipe is connected with an ozone monitor to measure the amount of exhausted ozone from the reactor.

3. Results and Discussion

3.1 Effect of two-step waveform with lower part

Ozone produced by three voltage waveforms with different peak voltage of the latter part, are performed in this section. Fig. 3 shows three different output voltage and current waveforms of the reactor in water treatment system. The output voltage and current were measured by using a 1:1000 high-voltage probe (PMK, PHV4002) and a 0.5 V/A current probe (Pearson, Model6595), respectively.

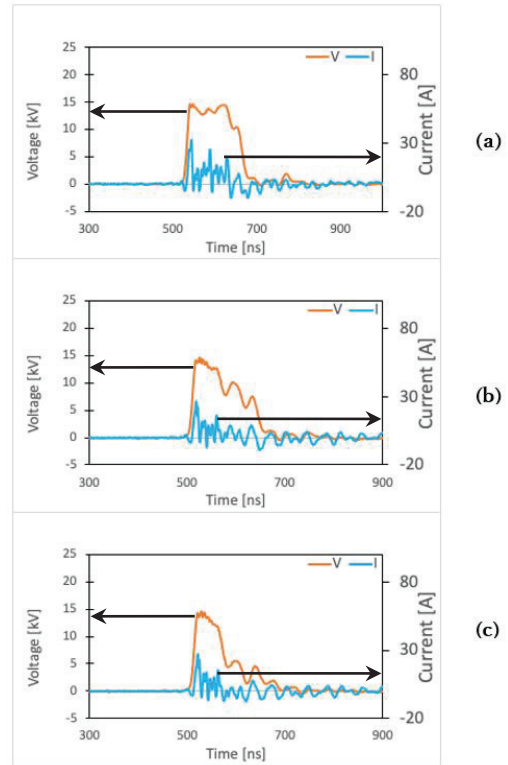


Fig. 3. Output voltage-current of reactor with two-step waveform and different peak of the latter part.

- (a) $2^{\text{nd}} \text{ peak} = 1^{\text{st}} \text{ peak}$.
- (b) $2^{\text{nd}} \text{ peak} / 1^{\text{st}} \text{ peak} = 2/3$.
- (c) $2^{\text{nd}} \text{ peak} / 1^{\text{st}} \text{ peak} = 1/3$.

In order to generate pulse in these waveforms, in the first part of pulse, MOSFETs of 23 LTD modules were turned on during first 60 ns. After that in the second part of pulse, some MOSFETs of LTD modules were turned off to reduce peak voltage in

next 60 ns, and finally all LTD modules were turned off. Numbers of MOSFETs of LTD modules were turned ON and OFF in the first and second part of pulse are shown in Table I.

Table I. Number of ON-state LTD modules in the first and second part of the pulse.

Case	Number of ON-state LTD modules	
	First part	Second part
a	23	23
b	23	15
c	23	7

Table II. Frequency and discharge energy of pulse in each case of two-steps waveform.

Case	Frequency [Hz]	Discharge energy [mJ]
a	50	10.3
b	75	6.95
c	100	5.21

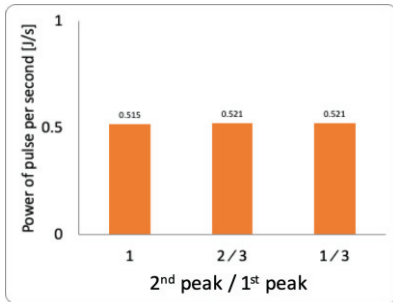


Fig. 4. Calculated result of power of pulse per second for each case of two-steps waveform.

Because peak voltage of the second part of pulse is reduced, discharge energy of pulse in three cases is very different. Therefore, to gain approximately similar electrical power in all cases, frequency of pulse was adjusted for each case. As shown in Table II, frequency in each case was adjusted according to discharge energy in order to achieve approximately similar electrical power in one second for each case. The electrical power in one second for each case was also calculated and performed in Fig. 4.

Produced ozone in reactor was measured by UV Ozone monitor (HARE, model-620), concentration of ozone produced by each waveform in Fig. 3 was

shown in Fig. 5(a). The decrease of peak voltage in second part leads to increasing concentration of produced ozone. As in Fig. 5(b), the energy efficiency of producing ozone increase when the voltage in second part is reduced.

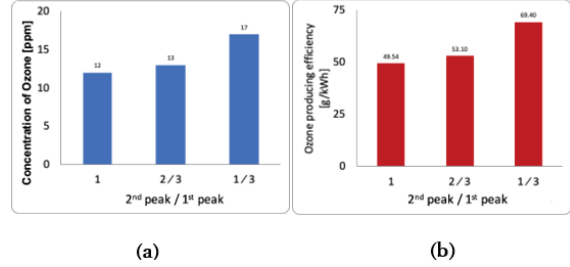


Fig. 5. Results of production of ozone by applying two-steps waveform according to rate of second and first peak voltage.

- (a) Results of concentration of ozone
- (b) Results of efficiency of producing ozone

3.2 Effect of interval in double-pulses waveform

The output voltage and current waveforms of the reactor module is shown as in Fig. 6. Intervals of four double-pulses waveforms are 1, 2, 5, and 10 μ s, respectively, and pulse width of all pulses is 60 ns. Frequency of two pulses burst is 50 Hz, i.e., 100 pulses/s. In addition, the measurement by 100 Hz output of single pulse, i.e., 10 ms interval of double-pulses, was also carried out and compared with those by double-pulses waveform. As in Fig. 6 and Fig. 7, the discharge current of the first pulse in double-pulses waveform is different with the second pulse, despite of the same peak voltage in the first and second pulse. And the discharge energy for each case is shown in Table. III. As shown in Table. III, in the case of interval of 1 μ s and 2 μ s, the discharge energy of second pulse decreased clearly. In the case of 5- μ s and 10- μ s pulse interval, the difference of the first and second pulsed energy was smaller, the discharge energy of the first and second pulsed is approximately similar in these cases. The possible reason of that phenomenon is the decrease of electric field by ion concentration to region close to wire electrode, the first pulsed discharge has left some positive charge in the gas that plays a role in weakening the electric field near the electrode when

the second pulsed voltage is applied to the electrode, which is described in detail in our previous paper [5]

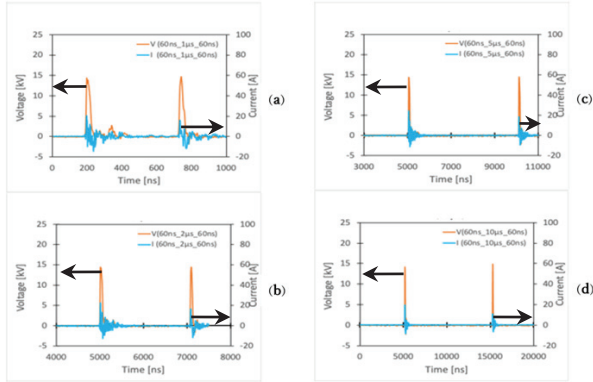


Fig. 6. Output voltage-current of reactor with double-pulses waveform and different interval.

(a) Pulse interval = 1 μs. (b) Pulse interval = 2 μs. (c) Pulse interval = 5 μs. (d) Pulse interval = 10 μs.

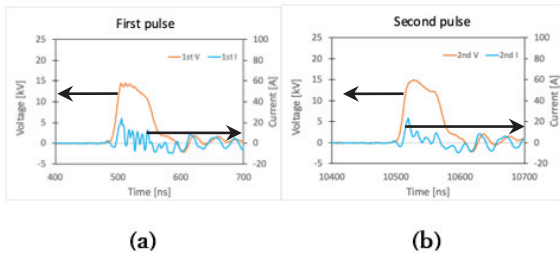


Fig. 7. Enlarged waveform of output voltage-current of reactor with 10 μs pulse interval.

(a) First pulse (b) Second pulse

Table III. Discharge energy of the first and second pulse in each case of double-pulses.

Interval	1 st Pulse discharge energy [mJ]	2 nd Pulse discharge energy [mJ]
1 μs	5.27	3.55
2 μs	5.58	3.53
5 μs	5.64	5.1
10 μs	5.75	5.32

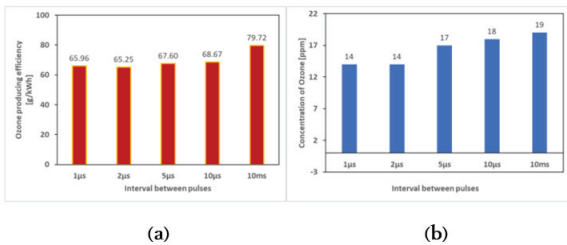


Fig. 8. Results of producing ozone by double-pulses discharge, varied with pulse interval.

(a) Results of concentration of ozone (b) Results of efficiency of producing ozone

The amount of ozone produced by double-pulses discharge with each different interval is shown in Fig. 8(a). Concentration of produced ozone is decreased when interval between pulses is reduced. As in Fig. 8(b), the energy efficiency of the interval from 1 to 10 μs was approximately similar. However, when the interval between two pulses is lengthened to 10 ms, energy efficiency of producing ozone is increased.

4. Conclusions

When the peak voltage of the latter part is reduced, the pulse power per one second is kept approximately similar for each case, concentration of produced ozone and energy efficiency will be increased. In addition, when interval between pulsed discharges is lengthened, ozone is produced greater and energy efficiency is increased. Finally, it can be expected that by shortening pulse width, production of ozone in water treatment system may be greater.

References

- [1] H. Tamaribuchi, D. Wang, T. Namihira, S. Katsuki, H. Akiyama, “Effect of pulse width on generation of ozone by pulsed streamer discharge”, Kumamoto University, 2-39-1 Kurokami, Kumamoto 860-8555, Japan.
- [2] R. Ono, Y. Nakagawa, and T. Oda, “Effect of pulse width on the production of radicals and excited species in a pulsed positive corona discharge”, *J. Phys. D, Appl. Phys.*, vol. 44, no. 48, pp. 485201-1–485201-9, 2011.
- [3] W. Jiang, H. Sugiyama, and A. Tokuchi, “Pulsed power generation by solid-state LTD”, *IEEE Trans. Plasma Sci.*, vol. 42, no. 11, pp. 3603–3608, Nov. 2014.
- [4] W. Jiang, “Solid-state LTD module using power MOSFETs”, *IEEE Trans. Plasma Sci.*, vol. 38, no. 10, pp. 2730–2733, Oct. 2010.
- [5] M. R. Kazemi, T. Sugai, A. Tokuchi, and W. Jiang, “Study of pulsed atmospheric discharge using solid-state LTD”, *IEEE Trans. Plasma Sci.*, vol.45, No.8, pp. 2323-2327, 2017.

Effect of Applied Electric Field Direction on Material Irradiation of Laminar Atmospheric Pressure Plasma jet with Double Coaxial Tube Structure

Kazuto Ishibashi and Hiroaki Ito

University of Toyama, 3190 Gofuku, Toyama 930-8555, Japan.

ABSTRACT

Recently, various studies on atmospheric pressure plasma jets (APPJ) have been conducted for applications to materials and medical field. In these applications, it is important to control the production of ionic and active species. We have developed the laminar flow APPJ using a double coaxial glass tube to increase the production of reactive species. The outer nitrogen gas flows independently in parallel to the core gas of helium and then interacts outside of the glass tube. In this study, we evaluated the effect of the direction of the applied electric field in the laminar flow APPJ on the material surface treatment.

Keywords

Keywords: atmospheric pressure plasma jet, double coaxial tube structure, barrier discharge, organic compound

1. Introduction

Low-temperature plasma like atmospheric pressure plasma has the characteristic that its ion and neutral species remain at room temperature, whereas only electrons have high temperature. Therefore, the atmospheric pressure plasma generates a variety of active components like charged particles, radicals, and reactive as well as excited species. It is possible to irradiate a heat-sensitive material and a human body without any heat damage, but with high chemical reactivity. Due to the operation at atmospheric pressure, atmospheric pressure plasma jets (APPJs) have been actively studied as valuable tools for surface processing [1], and agricultural and biomedical fields [2], such as chronic wound healing [3, 4], tooth bleaching [5], sterilization [6], and cancer treatment [7,8]. These applications strongly depend on plasma-generated reactive oxygen species and reactive nitrogen species. In order to meet the requirements of research and industrial application, it is very important for APPJs to increase and control productions of reactive species.

We have developed the double-coaxial plasma jet with the double coaxial glass tube instead of the

conventional single tube plasma jet to increase the ion species and active species [9]. In previous study, it was found from the comparison of the optical emission spectrum of the He/N₂ mixed gas plasma jet with single glass tube and the laminar plasma jet that the emission line intensity related to energetic active species, such as N₂ second positive (337 nm), N₂ first negative (391 nm), and OH (309 nm), in the double coaxial APPJ are stronger than those in the conventional APPJ. In addition, we evaluated the hydrophilicity improvement of polyethylene terephthalate (PET) treated by the APPJ. The treatment of PET films with the laminar APPJ improved surface hydrophilicity in comparison with the He APPJ.

We have developed two types of double coaxial plasma jet with the electric field applied in the perpendicular and parallel direction to the gas flow, respectively. This study reports the effect of the applied electric field direction in the laminar flow APPJ on the material surface treatment.

2. Experimental Setups

The double coaxial plasma jet has two independent

paths for central and surrounding gas flows. Thus, two different gases can be introduced into the glass tube and control each flow rate independently. Figure 1 shows a cross-sectional view of two types of double coaxial plasma jets with different directions of applied electric field. One is that the electric field is applied perpendicular to the gas flow as shown in Fig. 1(a). The other is that the electric field is applied parallel to the gas flow as shown in Fig. 1(b). For convenience, the plasma jets in which the directions of the applied electric field are perpendicular and parallel to the gas flow are defined as "Radial discharge type" and "Axial discharge type", respectively.

The glass tube in the radial type plasma jet consists of inner, intermediate, and outer glass tubes, and the size of each tube is shown in Table 1. The copper rod electrode was placed inside the inner tube to prevent sputtering by the plasma. The discharge is generated in the radial direction by applying the high voltage between the rod electrode and the copper tape wrapped around the intermediate tube. On the other hand, the glass tube in the axial type plasma jet consists of inner and outer glass tubes, and the size of each tube is

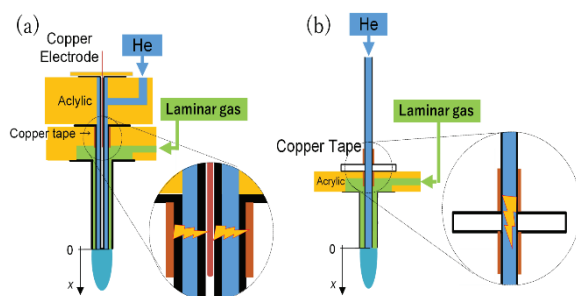


Fig.1 Cross-sectional view of double coaxial plasma jet device (a) Radial discharge type (b) Axial discharge type

Table 1 Size of each glass tube in radial type APPJ

Tube type	Inner dia.	Outer dia.	Length
Inner	3 mm	4 mm	80 mm
Intermediate	6 mm	10 mm	70 mm
Outer	13 mm	17 mm	45 mm

Table 2 Size of each glass tube in axial type APPJ

Tube type	Inner dia.	Outer dia.	Length
Inner	6 mm	10 mm	100 mm
Outer	13 mm	17 mm	40 mm

shown in Table 2. The inner glass tube has a flange to prevent from arcing between electrodes and is used as a dielectric barrier. The copper tapes are wrapped to both sides of the flange of the inner tube as an electrode. Thus, the discharge occurs in the axial direction, which is parallel to the gas flow.

Helium (99.99 %) gas was used for an inner gas flow to produce the core plasma due to the dielectric-barrier discharge, and nitrogen gas was used for a surrounding gas flow. Each flow rate was controlled by a mass flow controller (8500MC-S3-1-2, KOFLOC Co., Ltd.). Helium gas was passed through the inner path with a flow rate of 3–7 L/min. On the other hand, nitrogen gas was passed through the outer path with 0–8 L/min. The sinusoidal voltage with a peak value of 7 kV and a frequency of 20 kHz was used to induce the dielectric-barrier discharge in both radial and the axial type plasma jets.

The waveforms of voltage and current signals applied on the APPJ were measured by a high voltage probe (P6015A, Tektronix, Inc.) and a current transformer (4100, Pearson Electronics, Inc.). The optical emission spectrum from the plasma jet were evaluated at different positions in free jet region by using a spectrometer (EPP2000, StellarNet Inc.) in a wavelength range of 200–1000 nm with a typical full width at half maximum of 2.5 nm.

In order to study the effect of the applied electric field direction in the double coaxial plasma jet the decomposition of organic compounds by the APPJ irradiation were carried out. Methylene blue and indigo carmine were used as organic compounds. The initial concentration of each methylene blue and indigo carmine aqueous solution was set to 26 and 40 $\mu\text{mol/L}$, respectively. The volume of solutions was 10 mL. In addition, the surface treatment by the plasma jet was performed. The hydrophilicity of the acrylic surface was evaluated by measuring the contact angle of water droplets before and after plasma irradiation. The $\theta/2$ method was used for the measurement of contact angle. In the material treatment experiments, the helium and nitrogen gas flow rates were set to 5 and 2 L/min, respectively. Each material was placed at 15 mm from the exit of the plasma jet.

3. Experimental Results and Discussion

3.1 Methylene blue irradiation experiment

Figure 2 shows the change in color of the methylene blue solution treated with the APPJ every 5 minutes. The methylene blue is gradually decomposed and the color became lighter with increasing the treatment time. It can be seen that the color of the methylene blue solution treated with the radial discharge type is lighter than that treated with the axial discharge type at the irradiation time of 20 minutes.

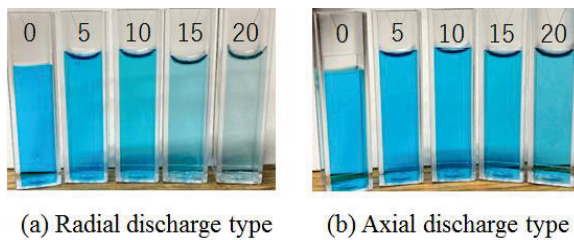


Fig.2 Color change of methylene blue solution treated with APPJ every 5 minutes: (a) Radial discharge type and (b) Axial discharge type

Figure 3 shows the effect of the applied electric field direction on the decomposition rate of the methylene blue solution as a function of the treatment time. The solid circles and triangles are the decomposition rates for the radial and axial discharge type APPJs, respectively. It is evident from Fig. 3 that the radial discharge type APPJ has a much higher decomposition rate than the axial discharge type. The decomposition rate reached about 89% after 20-minute treatment with the radial discharge type APPJ,

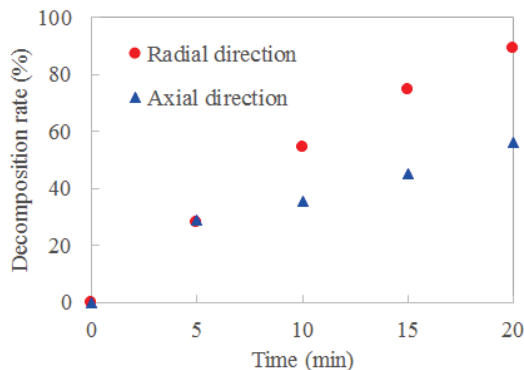
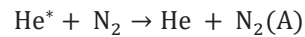


Fig.3 Dependence of applied electric field direction and treatment time on decomposition rate of methylene blue solution

while it was about 56% with the axial discharge type APPJ. Ozone is hardly derived from oxygen molecules in the APPJ and does not really contribute to the decomposition of the methylene blue, since nitrogen gas is used as the surrounding gas. Therefore, hydroxyl (OH) radicals generated by the following reaction with nitrogen are considered to mainly contribute to the decomposition. It is turned out that the APPJ with the radially applied electric field can generate more OH radicals than one with the axially applied electric field.



3.2 Indigo carmine irradiation experiment

Figure 4 shows the influence of the applied electric field direction on the decomposition rate of the indigo carmine solution at various treatment time. Indigo carmine is an organic compound that is easy to detect ozone, since it has a double bond of carbon in its molecular structure which is easily oxidized by ozone. Thus, oxygen was used as the laminar flow gas to generate ozone. As seen in Fig.4, the radial discharge type increase the decomposition rate in comparison with the axial one. After the 10-minute treatment time, the decomposition rate was about 74% in the axial direction, while it was about 92% in the radial direction. The generation of ozone in the plasma jet is explained as the following reaction. Two oxygen radicals are formed by the electron impact on an oxygen molecular and then ozone is produced by combining the oxygen radicals with other oxygen molecule. Therefore, the production of ozone is

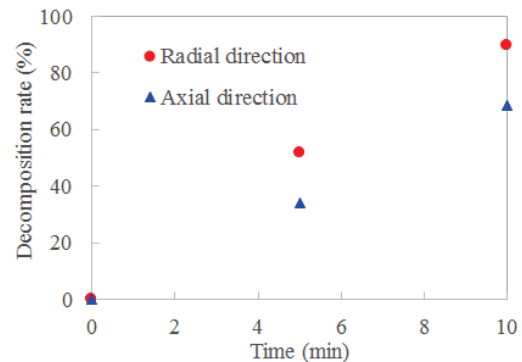
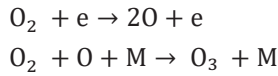


Fig.4 Dependence of applied electric field direction on decomposition rate of indigo carmine solution at various treatment time

considered to be higher in the radial discharge type APPJ.



3.3 Acrylic irradiation experiment

The experiments on the hydrophilicity improvement of acrylic was conducted to evaluate the influence of the applied electric field direction in the laminar He-N₂ plasma jet on the surface treatment. The surface properties of the untreated and plasma-treated samples are characterized by the water contact angle. Figure 5 shows the photo of water droplet on the untreated and plasma-treated acrylics, where the treatment time is 120 s. The water droplet on the untreated acrylic is an almost semicircle, while the water droplet on the plasma-treated acrylic spreads as if it was pulled by the acrylic. The contact angle decreased and the hydrophilicity was improved by both radial and axial discharge APPJs irradiation, as seen in Fig. 5.

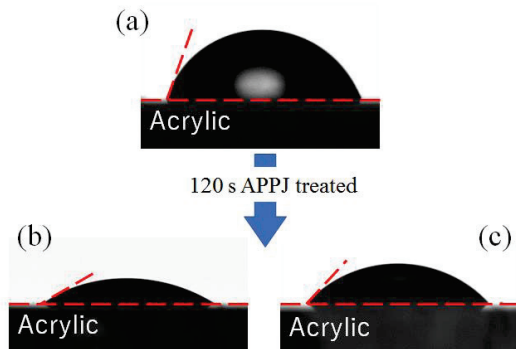


Fig.5 Photo of contact angle on (a) untreated, (b) radial type APPJ treated, and (c) axial type APPJ treated acrylic materials

Figure 6 shows the contact angle as a function of the treatment time for the radial and axial discharge type APPJs. The acrylic was placed at 15 mm downstream from the tip of APPJ. The contact angle dramatically decreases at the treatment time of 10s in both axial and radial discharge APPJs and levels off in the axial one, while gradually decrease with an increase of the time in the radial one. The contact angle of water droplets on the acrylic is smaller in the radial discharge APPJ than in the axial one after 120 second treatment time, resulting in the contact angle of 30° with the radial

APPJ and 48° with the axial one.

The hydrophilicity on the material surface is improved by the decomposition of organic matter and the formation of hydrophilic groups on the material surface by OH radicals. It is evident from the solid material irradiation experiments that the radial discharge APPJ increases the OH radical production in comparison with the axial discharge APPJ.

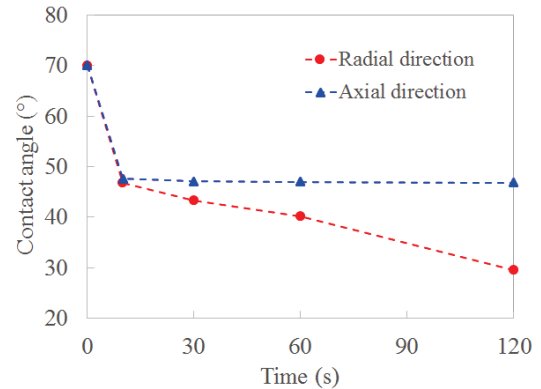


Fig.6 Contact angle as a function of treatment time for radial and axial discharge APPJs

3.4 V – Q Lissajous

Figure 7 shows the V – Q Lissajous diagram for radial and axial discharge APPJs. It can be seen that the area of Lissajous figure in the radial discharge type is larger than in the axial one. The area enclosed by the V – Q Lissajous curve corresponds to the energy introduced into the plasma per one cycle of the applied voltage. The input energy is estimated from Fig. 7 to be 1.93 mJ and 0.91 mJ for the radial and axial discharge APPJs, respectively. The input energy in the radial APPJ is twice higher as compared with the axial one, so that it is considered that the radial APPJ can

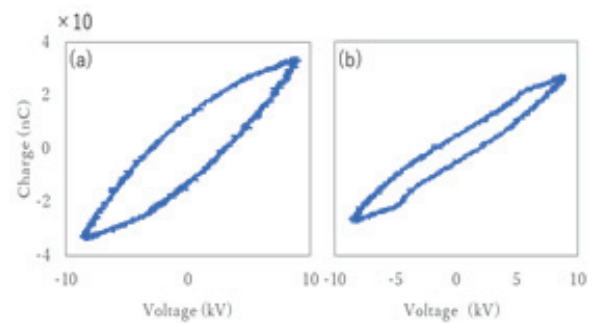


Fig.7 Comparison of V – Q Lissajous diagram for (a) radial and (b) axial APPJs

significantly generate ionic and active species. This result is in good agreement with the effect of the applied electric field on the material irradiation.

4. Conclusions

The influence of material treatment was evaluated for two types of double coaxial atmospheric pressure plasma jet with different applied electric field directions. In the APPJ-treated methylene blue, the color of the methylene blue solution became lighter for both radial and axial discharge APPJs. The radial APPJ increased the decomposition rate in comparison with the axial APPJ. This is because the radial type can produce more OH radical than the axial one. In the decomposition of indigo carmine, the radical APPJ had a higher decomposition rate than the axial one. This result indicates that the radial direction is also superior to the axial direction in ozone production. In the treatment of the acrylic surface, the contact angle decreased and the hydrophilicity was improved by both radial and axial APPJs. Comparing the radial and axial types, the radial APPJ significantly improved the hydrophilicity on the surface. We found from the results of the $V - Q$ Lissajous that twofold input energy was introduced into the radial APPJ. Therefore, the radial APPJ can greatly produce ionic and active species and contribute to the material treatment.

References

- [1] J. Lai, B. Sunderland, J. Xue, S. Yan, W. Zhao, M. Folkard, B. D. Michael and Y. Wang, "Study on hydrophilicity of polymer surfaces improved by plasma treatment", *Applied Surface Science*, vol. 252, pp. 3375 – 3379 (2006).
- [2] W. Chen, *et al.*, "Treatment of enterococcus faecalis bacteria by a helium atmospheric cold plasma brush with oxygen addition," *J. Appl. Phys.*, vol.112, p.013304 (2012).
- [3] N. Barekzi and M. Laroussi, "Fibroblast cell morphology altered by low temperature atmospheric pressure plasma", *IEEE Trans. Plasma Sci.*, vol.42, pp.2738–2739, (2014).
- [4] S. Fathollah, *et al.*, "Investigation on the effects of the atmospheric pressure plasma on wound healing in diabetic rats", *Sci. Rep.*, vol.6, p.19144, (2016).
- [5] S. H. Nam, *et al.*, "High-efficiency tooth bleaching using non-thermal atmospheric pressure plasma with low concentration of hydrogen peroxide", *J. Appl. Oral Sci.*, vol.21, pp.265-270 (2013).
- [6] S. Ikawa, *et al.*, "Effects of pH on Bacterial Inactivation in Aqueous Solutions due to Low-Temperature Atmospheric Pressure Plasma Application", *Plasma Process. Polym.*, vol.7, pp. 33-42 (2010).
- [7] G. Fridma, A. Gutsol, A. B. Shekher, V. N.Vasilets, and A. Fridman. "Applied Plasma Medicine" *Plasma Process. Polym.* vol.4, pp. 503 – 533 (2005).
- [8] D. B. Graves, "Reactive species from cold atmospheric plasma: Implications for cancer therapy", *Plasma Process. Polym*, vol.11, pp. 1120– 127, (2014).
- [9] H. Ohashi, K. Oyama, T. Mitani, K. Naiki, T. Nakayama, and H. Ito, "A Versatile Laminar Flow Atmospheric Pressure Plasma Jet Using a Double Coaxial Glass Tube", *IEEE Trans. on Plasma Science*, vol.45, pp. 2481-2485 (2017).

Review of the Massive Ion Inertial Fusion Driver for Future Inertial Fusion and our Understanding of Fusion Technology

K. Takayama¹, T. Adachi¹, T. Kawakubo¹, K. Okamura¹, Y. Yuri², J. Hasegawa³, K. Horioka³,
T. Kikuchi⁴, T. Sasaki⁴, and K. Takahashi⁴

¹*High Energy Accelerator Research Organization, Accelerator Laboratory,
Tsukuba, Ibaraki 305-0801, Japan*

²*National Institutes for Quantum and Radiological Science and Technology,
Takasaki Advanced Radiation Research Institute, Takasaki 370-1292, Japan*

³*Tokyo Institute of Technology, Ookayama, Tokyo 152-8550, Japan*

⁴*Nagaoka University of Technology, Nagaoka, Niigata 940-2188, Japan*

ABSTRACT

Review of the recently proposed massive ion inertial fusion scheme [1] is given., The driver accelerator complex can accelerate giant cluster ions as well as lead or bismuth ions, toward 120 GeV by using induction acceleration over the entire energy region. The proposed two-way multiplex induction synchrotron that is the main accelerator would be equivalent to 10 synchrotrons of the same size for a single beam. Crucial issues that must be solved hereafter are addressed.

Key Words: massive ion, inertial fusion, two-way multiplex induction synchrotron, direct beam irradiation

1. Introduction

First of all, it must be pointed out that the Fission Reactor Technology had been so quickly established in 14 years from the discovery of nuclear fission [2]. It is true that most of crucial basic physics and technologies such as understanding of the interactions between neutron and materials and uranium enrichment had been accomplished in developing atomic bombs through World War II at the cost of 200 B\$ in the present currency, involving obtainable brightest talents. This quick development was strongly motivated by US government that wanted to collect the huge investment to develop atomic bombs. In addition, it is inseparably related to the political situation after WWII, that is, cold war. Energy source replacing fossil fuels should have appeared to be quite attractive to victorious countries. In this sense, it may be unfair that we argue the historical development of Nuclear Fission Technology compared with other fundamental

technology, especially Nuclear Fusion Technology.

It is well known that nuclear fusion is more natural in nature and steadily occurs as a result of the confinement of fuel nucleus by the attraction of gravity, releasing tremendously enormous energy. However, the gravity is not available to realize artificial nuclear fusion on our globe. Instead, the inertial force triggered by an atomic bomb had been utilized for the first demonstration by humankind. Unfortunately, we had seen this artificial nuclear fusion as a hydrogen bomb, which caused vanishing of beautiful tropical islands surrounded by coral reefs and left a huge mass of residual radioactive materials on the earth in a global scale behind explosion. Since then, our end-less struggling to realize the controlled thermo-nuclear fusion continues, exploring a wide variety of schemes to overcome Lawson criterion [3]. As well-known, available driving forces are limited to the inertial force or Lorentz force. The latter has been quite popular

since the beginning of fusion research in a context of peaceful use of nuclear force or energy. This trial has not accomplished yet, although it took 70 years from the first proposal and 90 years from our first recognition of nuclear fusion in stars [4]. We are waiting for news from ITER that has already spent 20 B\$, holding our breath. Meanwhile, two approaches based on the former, where Laser Driven Inertial Fusion (LDIF) was proposed in 1970's and LBL initiated Heavy Ion Driven Inertial Fusion scheme (HIDIF) in the end of 70's and Europe followed this in 1980's. Large scale activities on LDIF seem to have taken a break since 2014 when NIFS, which had been extensively developed at the expense of 3 B\$, completed its study as Energy Science [5]. Present situation of the HIDIF is still far even from a single-shot demonstration of fusion, because the study has not been authorized by Governments as a core mission so far and only supported with an insufficient budget.

In this situation, the original massive ion fusion driver [1] has been recently proposed by the research forum consisting of members who have specialized in plasma physics, heavy ion fusion, pulsed power, ion source, fluid dynamic, and accelerator beam physics. Its notable properties will be characterized as follows.

- (1) Massive ion bunches of a total number of 100 are simultaneously provided from a single two-way multiplex induction synchrotron at 1 Hz.
- (2) Driver ions are heavy ions such as Pb or Bi and giant cluster ions such as C-60 or Si-100, energy of which is around 40 MeV/u.
- (3) Massive ion beams directly and unilaterally irradiate a spherical target of 10 mm in diameter.

2. Brief review of the proposed scenario

Its details are described in Ref. xx. Low charge state heavy ions such as Pb^{1+} or Bi^{1+} including cluster ions can be accelerated through the entire energy region by using induction accelerators, such as induction microtrons and induction synchrotrons.

The massive ion driver is an accelerator complex to accelerate giant cluster ions toward 120 GeV. It consists of 10 induction microtrons as injectors, a

multistage permanent magnet ring as stacking rings, and a two-way multiplex induction synchrotron as its main driver. A permanent stacking ring is placed between the injector and main accelerator, where massive ions are stacked to increase the beam intensity. The two-way multiplex induction synchrotron, which can accommodate both a forward and backward beam in a five-story beam line, is an advanced accelerator that makes maximum use of the guiding magnetic flux density and induction accelerating fields. Fig. 1 shows a schematic of the accelerator complex, where a massive ion beams of 40 MJ is produced in the main accelerator with an orbit circumference of 4 km. The accelerated beams are subject to sophisticated bunch compression in the driver ring before extraction, which is realized by independent and digital control of many induction acceleration cells. The forward/backward beams are extracted from individual extraction regions and guided to the fusion reactor region, performing further drift compression.

Figure 2 shows a schematic view of induction microtron. The cross-section of accelerator tunnel, where the stacking rings are placed on the upper floor and the main ring is placed on the lower floor of underground, is depicted in Fig. 1. The extraction region for the forward/backward beams is zoomed up in Fig. 3. Major beam and machine parameters are listed in Table 1.

3. Crucial issues

There are a lot of crucial issues that have to be solved hereafter. They may be classified in two categories of accelerator technology issue and beam physics issue and will be mentioned 1 by 1 as follows.

3.1 Driver

Ion source

Low charge state laser ablation ion source (LAIS) is a possible candidate for Pb and Bi. Recently Takahashi group of NagaokaTech demonstrated the LAIS for Pb^{1+} using a Pb compound liquid target with a low melting temperature [6]. This is one of milestones for the proposed scheme. Its operation at 40 Hz may be

the next target. Meanwhile, it is known through current R&D works at TokyoTech that it is not easy to generate high current C-60 and Si-100 ion beams with high charge-state. We may need any break-through idea.

Beam handling in the driver ring

Beam transfer from the stacking rings to the main driver ring has not been designed yet. It seems to be acrobatic beam handling. A combination of kicker magnets, septum magnets, and Lambertson magnets may work for this purpose. In order to maintain the same circumference of the forward/backward beams along the ring, the inner/outer paths have to change at an even number of positions.

Multiplex permanent magnet

Though there is a large scale use of permanent magnet in the antiproton stacking ring at FNAL, the permanent magnet with multiplex apertures required here has never been developed. It must be explored how the field uniformity is assured for all gaps.

Two-way multiplex normal conducting magnet for the main driver ring

A two-in-one magnet with two apertures is rather popular in a superconducting collider ring such as LHC. However, the two-way multiplex magnet with 10 apertures has never been demonstrated. Field adjustment for an individual aperture should be important. Independent iron-core quadrupole magnets with 10 apertures may be technically difficult from its mechanical size. A superconducting 2x5 aperture quadrupole magnet is alternative. Otherwise, the iron-core gradient magnet is another choice.

Two-way multiplex induction acceleration system and Beam loading

This device is new one too. The induction acceleration device, which accommodate 10 beam ducts with ceramic acceleration gaps, is shared by the forward/backward beams. The beam power per 1 bunch is 350 kW, which is twice of 1 bunch beam power in the Hyper Kamiokande experiment. At the last stage of bunch compression in the ring, the bunch length is expected to be order of 60 ns. Beam loading on the induction system is significant [7]. In addition, multiple beam loading effects have to be considered with our sufficient concern.

Final focusing

The final focusing region is placed in the central facility, the center of which is occupied by the fusion reactor. The final focusing region consists of the vertical bending magnet and a pair of focusing quadrupole magnets. The latter mimics the mini-beta insertion of a collider. A structure consisting of 100 sets will be a really gigantic scene beyond that of NIF. Residual dispersion functions are concerned here. It will depend on beam spot requirement on a fusion target whether the dispersion function has to be set completely null or not.

Space-charge effects

As well known, achievable beam intensity and emittance (or beam size) is determined by space-charge effects. In the massive ion beam driver, the effects become significant at the lowest energy in the injector and at the last stage of bunch compression in the main driver ring and through succeeding drift compression. Precise effects must be evaluated by a complementary approach of the use of complete computer simulations and the beam envelope equation with Gaussian beam corrections [8].

3.2 Target and Fusion reactor

Target physics

We assume direct irradiation of massive ions on a spheric fusion target that has a layer structure consisting of a tamper of Pb or Au, ablator of Al, and DT fuel. 20 massive ion beam spots hit the target with an equal distance in azimuthal angle at 0, ± 30 , and ± 60 degrees in elevation angle. So far it has not been systematically studied what happens as a result of this direct irradiation. Recently, a preliminary study has been initiated at NagaokaTech [9,10]. It suggests various interesting implosion processes strongly depending on the target structure geometry. Hereafter, the optimization study of target geometry and driver beam profile parameters must be systematically done by extensive computer simulation works. Recent paper reviewing issues of the HIB direct drive target [11] should be instructive in our case.

Reactor technology

There are two fusion reactor designs for LDIF scenario [12,13]. Some parts of these designs are quite

helpful to us. Energy conversion from the fusion fragments such as 14.5 MeV neutrons and α particles, and high speed fusion debris originated from tamper and ablator materials to the liquid wall using LiPb, which is assumed in Phase III of the laser fusion scenario (see Page 87 in Ref. 13), is the most important process. Most of technical issues there including target injection are common among the LDIF reactor and MDIF reactor. We will address an undesired feature of the MFIF reactor that a fraction of products generated after ignition radially propagates to necessarily enter into the massive ion beam ports, which open from the liquid wall.

4. Conclusions

At this moment, we don't conclude that the proposed MIDF scheme is promising, because there are a lot of issues left unsolved, although the proposed scheme has a potential to explore a new era of inertial fusion science. Our research forum will continue the necessary analysis and further studies. Once an appropriate research grant for R&D works is acquired, demonstration of the driver related key technology will make a start in addition to systematic computer simulations on target physics and reactor technology.

References

[1] K. Takayama *et al.*, "A massive-ion beam driver for high-energy-density physics and future inertial fusion", *Physics Letters A* **384**, 126692 (2020).
 [2] O. Hahn and F. Strassmann, "Concerning the existence of alkaline earth metals resulting from neutron irradiation of uranium", *Naturwissenschaften* **26**, 755 (1938).
 [3] J. D. Lawson, "Some criteria for a power producing thermo nuclear reactor", *Proc. of Phys. Soc. B* **70**, 6 (1957).
 [4] R. D'E. Atkinson and F. G. Houtermans, "Transmutation of the lighter elements in stars", *Nature* **123**, 567 (1929).
 [5] D. Kramer, "Livermore ends LIFE", *Physics Today* **67**(4), 26 (2014).
 [6] K. Takahashi, private communication (2021).
 [7] 高山健、岡村勝也、由元崇、"誘導加速セルに

於けるビーム負荷の評価", KEK Report 2020-3 (2020).

[8] T. Ebisawa and K. Takayama, "Gaussian macro-particle and beam-envelope approaches for an asymmetric beam in a solenoid channel with space-charge effects", submitted to *Phys. Lett. A* (2021).
 [9] 林哲浩 他, "イオンビーム直接照射型慣性核融合燃料標的のタンパー形状の検討", this meeting
 [10] 渡辺直人 他, "重イオン慣性核融合燃料ペレットの低密度層での半径方向輻射輸送が爆縮速度へ与える影響", this meeting
 [11] S. Kawata, "Direct-drive heavy ion beam inertial confinement fusion: a review, toward our future energy source", *Advances in Physics X* **6**, 1873860 (2021).
 [12] W. R. Meier *et al.*, "Fusion technology aspects of laser inertial fusion energy (LIFE)", *Fusion Engineering and Design* **89**, 2489 (2014).
 [13] 高速点火レーザー核融合実験炉概念設計委員会報告、平成 27 年 3 月 31 日 (2015).

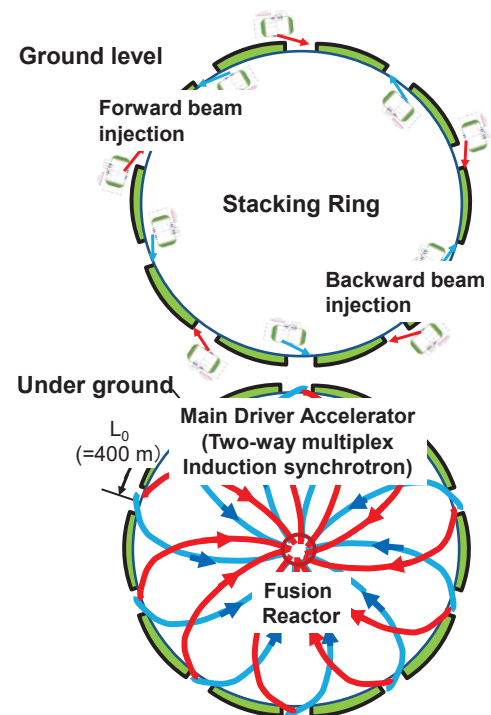


Fig.1 Massive Ion Driver

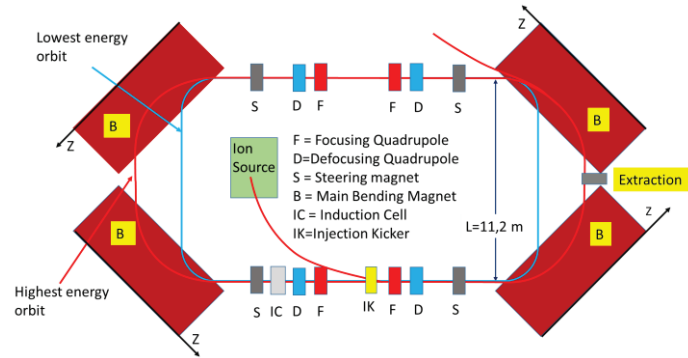


Fig. 2 Induction Microtron (Injector)

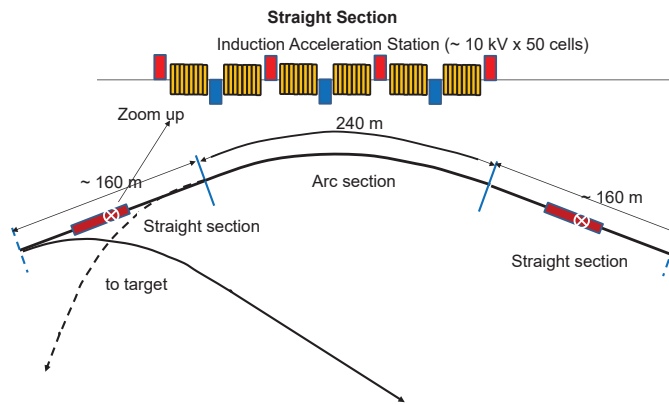


Fig. 3 1/10 of the main driver ring with the extraction lines for forward/backward beams

Table 1
Machine and Beam Parameters.

Circumference		C_0 (m)	4000
	1 super-period	$C_0/10$ (m)	400
	Arc/Straight section		240/160
Normal bending magnet (ramping time 0.5 sec)		B (Tesla)	0.05–1.5
Curvature		ρ (m)	224.3
Betatron tune		Q_x/Q_y	25.91/25.22
Transition gamma		γ_T	20.7
Acceleration cycle		f (Hz)	1
Acceleration voltage/turn		$V_{acc} = \rho C_0 (dB/dt)$ (MV)	2.6
Rep-rate of induction acceleration system		$(f_{IAC})_{max}$	~250 kHz
Cluster ion Si-100		A	28×100
		Q	10
Energy change in the MR		E_{inj} (GeV)	0.35
		E_{final} (GeV)	120
		N_0	5×10^{12}
Number of particles/pulse transferred from the Injector to the SR			4
Number of pulses injected from the Injector to create 1 superbunch in the SR			10
Number of superbunches/beam in the SR/MR			5/5
Number of forward/backward beams in the SR/MR			
Total number of particles guided to the target		$N = 2 \times 5 \times 10 \times 4 \times N_0$ $= 4 \times 10^2 \times N_0$	2×10^{15}
Beam energy/shot		$E_{shot} = N \times E_{final}$ (MJ)	38.4
Average beam power deposited on the target		$P = E_{shot} \times f$ (MW)	~ 40

Characteristics of pulsed ion beam emitted from plasma focus device with different anode shapes

Yuto Sagano, Takuho Yamada, Takanori Nunome, Hiroaki Ito and Taichi Takezaki

University of Toyama, 3190 Gofuku, Toyama 930-8555, Japan

ABSTRACT

Characteristics of the ion beam produced in a plasma focus device has been studied. In this experiment, a Mather type plasma focus device was used and was pre-filled with H₂ gas. The effect of four different anode shapes, cylindrical tip with a hollow top, tapered tip with a hollow top, and two different tapered-angle tips with a flat top, on the proton beam characteristics was investigated. When the plasma focus device with the tapered flat-end with the taper angle of 45° was driven by a capacitor bank of 41.6 μF and charging voltage of 30 kV, the discharge current reached a peak current of 670 kA, and after the current dip, an ion current density of 8.3 kA/cm² was obtained 110 mm downstream from the top of the anode on the axis. The ion current density with the tapered anodes tended to be higher as compared with the cylindrical anodes. The results on the ion energy indicated that the ion beam with a maximum energy of 2 MeV was obtained in the tapered hollow-end anode with the taper angle of 10°.

Keywords

Plasma focus device, Pinch plasma, Pulsed ion beam, Ion beam energy

1. Introduction

Plasma focus device is fundamentally a simple device, consisting of a capacitor bank and coaxial electrodes in a low-pressure chamber. Plasma focus device belongs to the class of Z-pinches, in which a self-induced magnetic field strongly constricts the plasma to produce a hot (> 1 keV) and high-density ($> 10^{19}$ cm⁻³) plasma column with a lifetime of about 50–100 ns. This device has attracted much attention as a remarkable source of hard and soft x-rays, neutrons, energetic ions and relativistic electrons [1-4] in applications such as electron and soft x-ray lithography [5], x-rays backlighting [6], biological radiography [7], processing and deposition of thin films [8]. Further, many researchers have devoted to investigating various physical phenomena such as current sheath dynamics, instability growth, and pinch formation etc. along with on the emission of x-rays and neutrons by changing experimental conditions such as electrode geometry, capacitor bank energy, working gas type and pressure.

Plasma focus device has an interesting phenomenon, in which generated energetic ion beams with energy more than a few hundred of keV to tens of MeV far in excess of the capacitor-bank charging voltages [9,10]. Emission of the energetic ions is considered to occur as the phenomena that give rise to a localized high electric field, such as rapid compression during the radial pinch phase and instability. In recent studies, an asymmetric angular distribution of ions energy and density in a plasma plume after a pinch formation has been explained by the fact that ions are originated from different micro-sources which are created inside a dense pinched plasma column [11,12]. Furthermore, the dependence of electrode geometry, capacitor bank energy, working gas type and pressure on the ion flux angular distribution of the ion beam in plasma focus devices has been investigated. However, the physical mechanism leading to the ion acceleration remain a room for investigation.

The evaluation of ion beam characteristics such as ion energy and angular distribution is very important

not only for understanding the physics behind generation of the energetic ions but also for optimizing the plasma focus device for the applications such as material processing and thin film deposition. In spite of remarkable efforts to investigate neutron and x-ray signals in different anode shapes, little research was done on the energy of the ion beam produced by the plasma focus device with different anode shapes. In this study, we evaluate the intensity and energy of the hydrogen ion beam produced by the plasma focus with four different anode shapes, cylindrical tip with a hollow top, tapered tip with a hollow top, and two different tapered-angle tips with a flat top.

2. Plasma focus operating principle

Figure 1 shows the operating principle of the plasma focus. The plasma focus is composed of coaxially arranged anode and cathode electrodes in the vacuum vessel. An insulator surrounds the bottom end of the anode, separating the electrodes. When a high voltage pulse is applied between the electrodes after filling a gas in the chamber, the discharge current due to the dielectric breakdown flows on the insulator, which leads to the ionization of the filling gas and formation of the current sheath. The current sheath forms on the insulator surface or radially bridges the electrodes at the end of the insulator. In the axial run-down phase, the self-generated $J \times B$ force (Lorentz force) causes the current sheath to move along the anode to the open end of the electrodes. As the current sheath is accelerated to reach many times the speed of sound in the ambient gas, the shock wave is generated in front of the current sheath. The gas that is cumulated by the moving shock front is ionized and converts into plasma by the current flow, generating pairs of radial filaments in the process. When the current sheath reaches the electrodes end, the plasma is compressed in the radial direction by the inward Lorentz force. Then a hot and dense plasma column is formed on the top of the anode. This plasma column is quite unstable and collapses due to the growth of instabilities such as sausage instability, etc., which leads to an emission of soft x-rays and an induced electric field. With this electric field, electrons are accelerated towards the

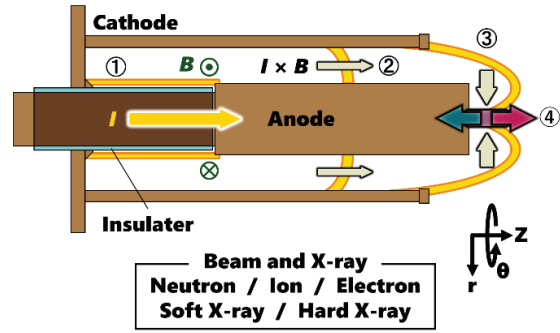


Fig.1 Operation principle of plasma focus

anode, while ions are accelerated in the opposite direction.

3. Experimental setup

The plasma focus device used in the present study is a Mather-type device. The electrode arrangement is composed of a central copper anode with 270 mm in length and 50 mm in diameter and a cathode made up of 24 copper rods arranged in a circle of 100 mm in diameter. The length and diameter of 24 cathode rods are 245 mm and 10 mm, respectively. A Pyrex glass insulator sleeve with 100 mm long and 60 mm in outer diameter is rigidly fixed at the bottom end of the anode separating the electrodes.

In order to investigate the effect of the anode tips on the intensity and energy of the ion beam, we used four different geometries, i.e., cylindrical with a hollow top, tapered with a hollow top, and two tapered with a flat top having taper angles of 10° and 45° , respectively. Figure 2 shows the design of four anode tips. The total length of the anode is 270 mm and the

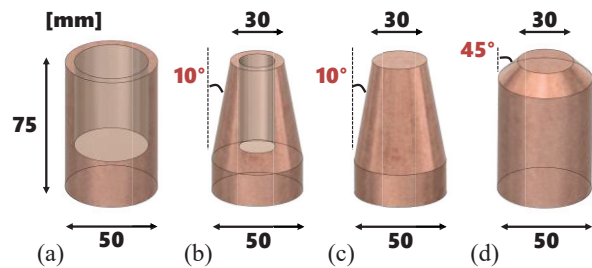


Fig. 2 Design of four different anode tips: (a) cylindrical hollow-end anode, (b) 10° tapered hollow-end anode, (c) 10° tapered flat-end anode, and (d) 45° tapered flat-end anode.

effective length of all these tips is 75 mm. The diameter of tapered anode tip is 30 mm. To reduce the production of impurity ions and the damage of the electrode, the anode has a hollow shape top. The hollows of cylindrical and tapered anodes have 50 mm in depth and 39 mm and 20 mm in diameter, respectively.

Figure 3 shows the experimental arrangement of the plasma focus. The plasma focus device consists of a pulsed power driver (capacitor bank), coaxial electrodes, a stainless-steel chamber with a diffusion pump package and a measurement system. The vacuum chamber is evacuated to $< 7 \times 10^{-3}$ Pa and then filled with hydrogen gas. The filling pressure was changed in the range of 300 to 1200 Pa in steps of 100 Pa. The charging voltage of the capacitor bank with a capacitance of 41.6 μ F was fixed to 30 kV, which corresponded to the discharge energy of 19 kJ. The discharge current and ion current density were measured with a Rogowski coil and a biased ion collector (BIC), respectively. The BIC is a simple and inexpensive diagnostic, which generally consists of a small aperture and a deep collector biased at a negative potential to remove any electrons accompanying the ion beam. In order to evaluate the angular distribution of proton beam emitted from the plasma focus device, an array of nine BICs located at angular positions -80° , -60° , -40° , -20° , 0° , 30° , 50° , 70° and 90° with respect to the anode axis and 110 mm away from the anode tip was used, where 0° is the axis of anode. The energy evaluation of ion beam was performed using a magnetic field deflecting energy analyzer placed at the axis of anode. A hard x-ray radiated from the anode due to electron bombardment was also measured by a scintillation probe with a combination of plastic scintillator and photomultiplier located at 6 m away from the anode tip.

Figure 4 shows a magnetic field deflecting energy analyzer used in this study to measure the energy spectrum of the ion beam. The energy spectrometer consists of a 1st pinhole, a 2nd pinhole, a permanent magnet and a solid state nuclear track detector CR-39. A small portion of the ion beam is collimated by a pair of pinholes with aperture diameters of 0.3 mm and 0.2

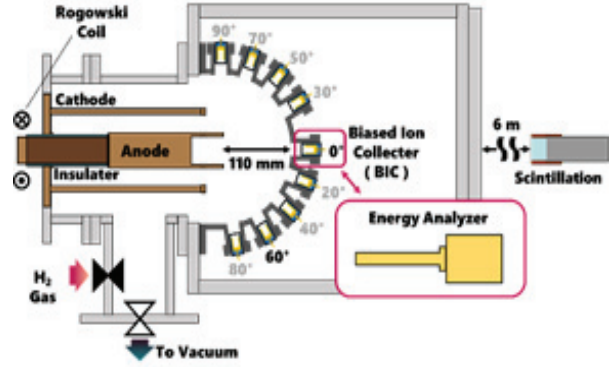


Fig.3 Experimental arrangement

mm, respectively. The collimated beam is passed through deflection part with a magnetic field of $B = 0.6$ T perpendicular to the beam direction. The deflection distance D_B due to the magnetic field is expressed in Eq. (1)

$$D_B = \frac{ZeBL L_d}{mv}, \quad (1)$$

where Z is the charge state of the ion, e is elementary charge, m is the ion mass, v is the ion velocity, L is the length of the magnet, and L_d is the distance from the center of the magnet to the detector. The beam diameter on the detector D_3 is obtained from Eq. (2)

$$D_3 = D_2 \left(1 + \frac{L_2}{L_1} \right) + D_1 \frac{L_2}{L_1}, \quad (2)$$

where D_1 and D_2 are diameters of the first and second pinholes, respectively, and L_1 and L_2 are distances between the two pinholes, and between the second pinhole and detector, respectively. Using the

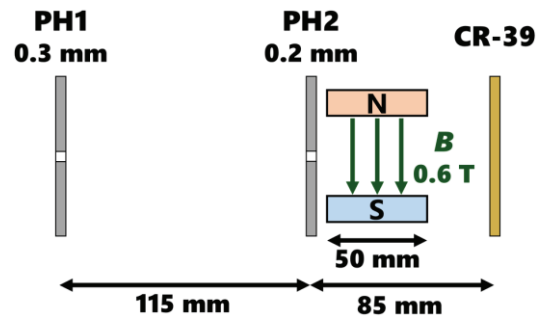


Fig.4 Schematic diagram of magnetic field deflecting energy analyzer

experimental parameters, the beam diameter on the detector plane is $D_3 = 0.57$ mm.

4. Experimental result and discussion

Figure 5 shows typical waveforms of the discharge current, the ion current density at angular positions of 0° and -60° , and the hard x-ray in the cylindrical hollow-end anode, where the gas pressure is 500 Pa. As seen in Fig. 5, the discharge current reaches a peak value of 670 kA at 1.8 μ s, and after the peak, a 270 kA current dip is observed, which indicates the strong induced electric field after the disruption of plasma column. Both hard x-ray and ion current density rise sharply with the current dip ($t = 1.7$ μ s). The ion current density on the axis (0°) has a peak value of 7.0 kA/cm² with a pulse duration of 50 ns (FWHM), while at 60° , a peak value of 1.4 kA/cm² is observed with a pulse duration of 1.0 μ s. The time difference between the peaks of the ion current density is 100 ns, which suggests that ions traveling towards the axis have the highest energy.

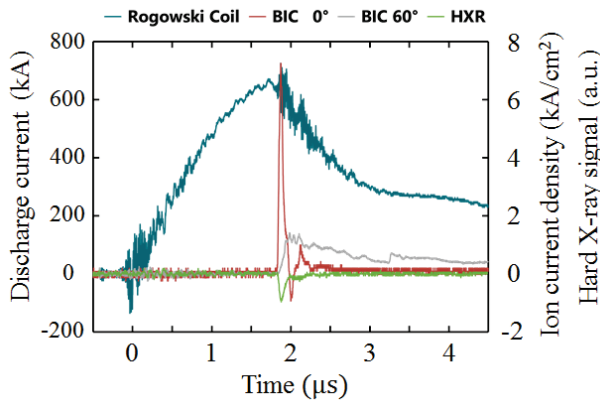


Fig.5 Typical waveforms in plasma focus device

Figure 6 shows the ion current density on the axis as a function of the filling gas pressure for four different anode tips. Each point is the average of five shots. The maximum ion current density is 6.6 kA/cm² at 500 Pa for the cylindrical hollow-end anode, 7.3 kA/cm² at 600 Pa for the 10° tapered hollow-end anode, 7.4 kA/cm² at 600 Pa for 10° tapered flat-end anode and 8.3 kA/cm² at 500 Pa for the 45° tapered flat-end anode. The ion current density was the highest for the 45° tapered anode followed by the 10° tapered and the cylindrical anodes in that order. It is turned out

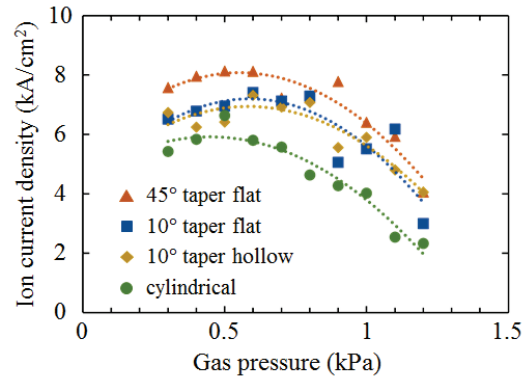


Fig.6 Ion current density as a function of filling gas pressure for 4 different anode geometries

from Fig. 6 that the tapered anode has higher ion current density than the cylindrical one and that little significant effect of the hollow is given to the ion current.

Figure 7 shows the angular distribution of the ion current density at each optimal gas pressure for four different anode geometries. Each point is the average of five shots. The ion current density is maximum on the axis and decreases with the increase of the angular angle. The effect of the anode shape on the ion current density is the same result as Fig. 6. As seen in Fig. 7, the ion beam at the larger angle is higher for the flat anode than for the hollow one, which suggests that with the flat anode the ion beam tends to propagate with more divergence.

The averages of five shots hard x-ray signal for four different anode geometries and different gas pressures are shown in Fig. 8. Both optimal gas pressure and influence of the hollow shape on the hard x-ray for

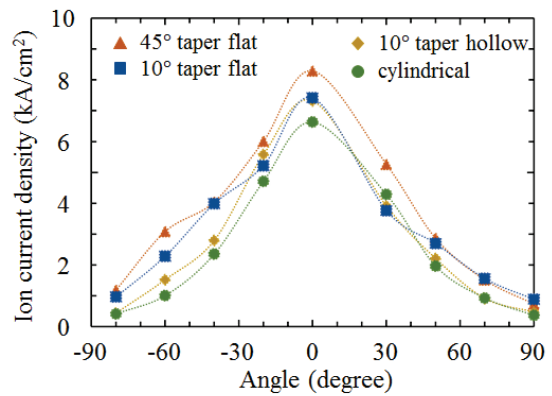


Fig.7 Angular distribution of ion current density for 4 different anode geometries

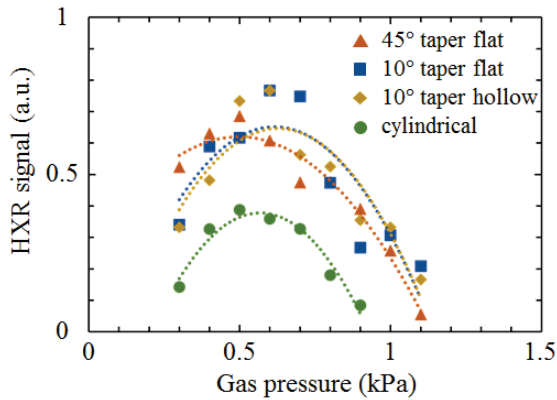


Fig.8 Hard x-ray signal as a function of filling gas pressure for 4 different anode geometries

each anode geometry are similar to that of the ion current density. The ion current density was the highest for the 45° tapered anode while the hard x-ray signal was the highest for the 10° tapered anode. The scintillation emission of a plastic scintillator is proportional to the number and energy of incident photons. It is considered from Fig. 6 that the number of electrons generated in the plasma device with the 45° tapered flat-end anode is higher than with the 10° tapered flat-end and 10° tapered hollow-end anodes. Thus, Fig.8 suggests that the charged particles with the 10° tapered anode have higher energy.

Figure 9 shows the example of the ion track on the detector obtained with the magnetic field deflecting energy analyzer mounted at the angular position of 0°. Three anode geometries, cylindrical hollow-end, 10° tapered hollow-end and 45° tapered flat-end anode were chosen, since from above results, the effect of the hollow anode on the ion beam was confirmed. The gas

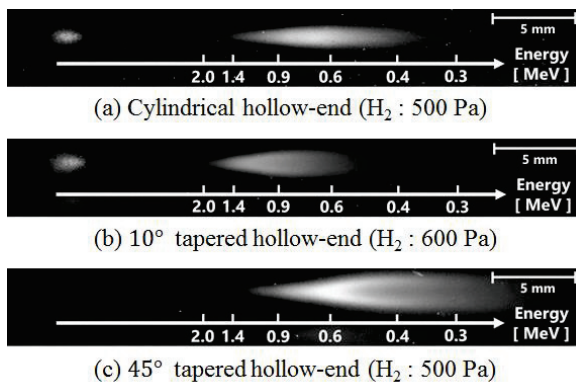


Fig.9 Energy distribution of ion beam for 3 different anode geometries

pressure for each anode was set to the optimum. The track on the left in the figure is formed by undeflected charge-exchange neutral beams and is useful for an orientation to calculate the energy. The energy band of the ion beam is 0.35~1.4 MeV for the cylindrical hollow-end anode, 0.5~2.0 MeV for the 10° tapered hollow-end anode, and 0.2~1.2 MeV for the 45° tapered flat-end anode. Thus, the ion beam energy is seen to be maximum for the 10° tapered hollow-end anode, while it is the lowest in the 45° tapered flat-end one. On the other hand, it is evident that the longitudinal deflection in Fig. 9 depends on the electrode shape. In general, the longitudinal width is considered to be equal to the beam diameter of 0.57 mm geometrically calculated by Eq. (2), which is the width of the neutral point. The maximum width is 1.72 mm at the ion energy of 650 keV for the cylindrical hollow-end anode, 1.94 mm at 900 keV for the 10° tapered hollow-end anode, and 2.46 mm at 400 keV for the 45° tapered flat-end anode. The reason for this deflection has not been understood yet.

It was confirmed from the experimental results that both the current density and the energy of the ion beam were enhanced by using the tapered anode. The reason may be explained in the following way. In the radial implosion phase, when the imploding front of the shock wave in front of the current sheath coalesces onto the axis, a reflected shock front emerges from the central axis and collides with the current sheath moving toward the center of the anode [13]. After the collision, the radially inward motion of the magnetic piston is reversed. Thus, the axisymmetric boundary of the pinch plasma column is formed. Decrease in the radius of the anode end reduces the time for the

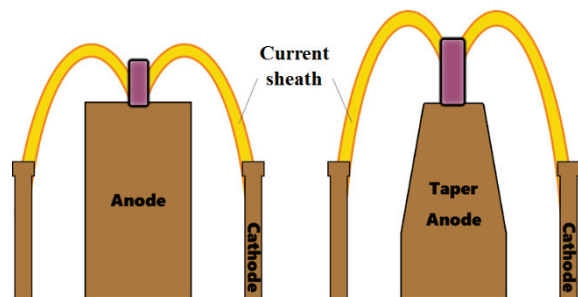


Fig.10 Influence of anode geometry on current sheath and plasma column

reflected shock wave to collide the current sheath. A suppression of rapid changes in the current sheath motion at the transition increases the symmetry of the accelerating current sheath, the swept mass introduced into the pinch phase, and the plasma lifetime before instabilities [14]. Thus, as shown in Fig.10, in the case of the tapered anode, the front part of the current sheath in contact with the anode elongates axially. The plasma column is strongly and stably pinched and the induced electric field is enhanced.

5. Conclusions

The intensity and the energy of proton beam emitted from a plasma focus device with four different anode tips was investigated at various pressures. The tapered anodes significantly enhanced the intensity and the energy in comparison with conventional cylindrical one. Reduction in the radius of the anode end leads to a suppression of rapid changes in the current sheath at the transition phase from axial acceleration to radial implosion phase and a generation of dense and hot pinch plasma, and consequently increase the induced electric field. These results indicates that the plasma focus device could be improved to a great extent for optimal ion beam intensity and ion energy by using an appropriate anode tip.

Acknowledgement

This work was supported by JSPS KAKENHI Grant Number JP19H02126.

References

- [1] M.A. Mohammadi, *et al.*, “The effect of anode shape on neon soft X-ray emissions and current sheath configuration in plasma focus device”, *J. Phys. D*, **42**, 045203 (2009).
- [2] A. Vladimir, *et al.*, “Examination of a chamber of a large fusion facility by means of neutron activation technique with nanosecond neutron pulse generated by dense plasma focus device PF-6”, *Fusion Eng. Des.*, **125**, pp.109–117 (2017).
- [3] H.R. Yousefi, Y. Nakata, H. Ito, K. Masugata, “Characteristic observation of the ion beams in the plasma focus device”, *Plasma Fusion Res.*, **2**, S1084 (2007).
- [4] A. Patran, *et al.*, “Spectral study of the electron beam emitted from a 3 kJ plasma focus”, *Plasma Sources Sci. Technol.*, **14**, pp.549-560 (2005).
- [5] P. Lee, *et al.*, “Electron lithography using a compact plasma focus”, *Plasma Sources Sci. Technol.*, **6**, pp.343-348 (1997).
- [6] M. Zakaullah, *et al.*, “Scope of Plasma Focus With Argon as a Soft X-Ray Source”, *IEEE Trans. Plasma Sci.*, **30**, pp.2089-2094 (2002).
- [7] F. Castillo-Mejia, *et al.*, “Small Plasma Focus Studied as a Source of Hard X-Ray”, *IEEE trans. Plasma Sci.* **29**, pp.921-926 (2001).
- [8] I.A. Khan, *et al.*, “Deposition of zirconium carbonitride composite films using ion and electron beams emitted from plasma focus device”, *Nucl. Instru. Meth. Phys. Res. B*, **268**, pp.2228-2234 (2010).
- [9] H. Kelly, *et al.*, “Analysis of the Nitrogen Ion Beam Generated in a Low-Energy Plasma Focus Device by a Faraday Cup Operating in the Secondary Electron Emission Mode”, *IEEE Trans. Plasma Sci.*, **26**, pp.113-117 (1998).
- [10] H. Ito, Y. Nishino, K. Masugata, “Emission characteristics of a high-energy pulsed-ion-beam produced in a dense plasma focus device”, *J. Korean Phys. Soc.*, **59**, pp3674-3678 (2011).
- [11] M. Bhuyan, N.K. Neog, S.R. Mohanty, C.V.S. Rao, P.M. Raole, Temporal and spatial study of neon ion emission from a plasma focus device, *Phys. Plasmas*, **18**, 033101 (2011).
- [12] Morteza Habibi, “Angular distribution of ion beam emitted from a 3.5 kJ plasma focus device using different shapes of anodes”, *Phys. Lett. A*, **380**, pp.439-443, (2016).
- [13] S. Lee, “Energy balance and the radius of electromagnetically pinched plasma columns”, *Plasma Phys.*, **25**, pp571-576 (1983).
- [14] M. Zakaullah, I. Ahmad, A. Omar, G. Murtaza, M.M. Beg, “Effects of anode shape on plasma focus operation with argon”, *Plasma Sources Sci. Technol.*, **5**, pp.544-552 (1996).

One-dimensional PIC-MCC Analysis of Inertial Electrostatic Confinement Plasma

Kazuhiro Matsuda, Jun Hasegawa

Laboratory for Advanced Nuclear Energy, Tokyo Institute of Technology

ABSTRACT

To simulate particle dynamics in an inertial electrostatic confinement fusion device, a 1D PIC-MCC code was developed and tested. It took account five major collisional processes occurring in glow-discharge hydrogen plasma and partly reproduced the dependency of discharge starting voltage on background gas pressure, which is predicted by the Paschen's law.

Keywords

Neutron Source, Inertial Electrostatic Confinement Fusion, Glow Discharge, PIC-MCC Simulation

1. Introduction

Neutrons are one of the nucleons that compose the atomic nucleus together with protons, and has no electric charge. Therefore, neutrons do not interact electromagnetically with charged particles and have very high material permeability. X-rays are also well known as radiation with high material permeability, but there is a big difference in the way they interact with matter. X-rays lose energy mainly by interacting with electrons in the atom, so they are well shielded by atoms with large atomic numbers. In contrast, neutrons lose energy due to elastic collisions with atomic nuclei, so they are well shielded by atoms with small atomic numbers. X-rays can be easily generated by irradiating a solid target with an electron beam of several keV to several tens of keV. On the other hand, to generate neutrons, it is necessary to use a nuclear reaction. Therefore, while X-rays have been used in various fields such as X-ray photography and baggage inspection at airports, the industrial use of neutrons has been limited.

In recent years, the application of neutron rays in various fields is expected with the development of accelerator-driven high-intensity neutron sources such as J-PARC and Riken RANS. High-intensity neutron sources based on huge particle accelerators and nuclear fission reactors can provide neutron

production rates (NPR) more than 10^{13} neutron/s, but costs of construction and operation are extremely high. On the other hand, neutron sources that use radioisotopes such as ^{252}Cf are less intense than other neutron sources, despite their high management costs.

Inertial electrostatic confinement (IEC) fusion neutron sources are small, inexpensive, and highly portable neutron sources[1]. Its principle is schematically shown in Fig. 1. In the IEC fusion neutron source, deuterium ions are generated by glow discharge in low-pressure (~ 1 Pa) deuterium gas. After accelerated by the electric field between the electrodes, some deuterium ions and neutral particles collide with deuterium molecules in the background gas and cause D-D fusion reactions to generate 2.45 MeV neutrons.

One of the most important issues of the IEC fusion

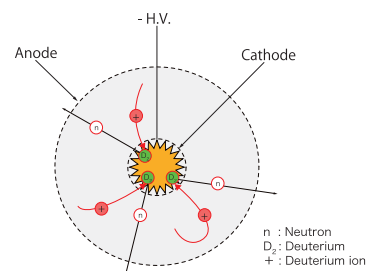


Fig. 1. Principle of inertial electrostatic confinement fusion neutron source.

neutron source is improving the neutron production efficiency. NPRs of $\sim 10^6$ to 10^8 n/s have been achieved in previous researches on IEC neutron sources. In order to achieve NPRs more than 10^9 n/s, it is inevitable to increase the electric input power, which probably brings serious problems to the discharge electrodes due to excessive heat load originating from high-energy particle bombardment. Therefore, it is very important to understand the behavior of energetic particles in the IEC device and feedback that knowledge to the device design.

Our research group has also been studying particle behavior in an originally developed IEC device by combining Doppler spectroscopy and numerical analyses based Monte Carlo simulation. In those analyses we assumed a vacuum potential because the degree of ionization of background gas in the IEC device was quite low. However, if the input power is increased, the potential modulation due to the space charge effect will be remarkable. In this study, in order to perform numerical analyses including the space charge effects, we developed a one-dimensional simulation model based on the particle-in-cell – Monte-Carlo collision (PIC-MCC) method and performed preliminary analyses.

2. Analytical method

The PIC-MCC method is one of the PIC methods including particle collisions based on the Monte-Carlo method. In principle, the PIC method treats the electromagnetic interactions among charged particles via spatially averaged electric and magnetic fields induced by the charged particles themselves[2]. Although it can solve the collective behavior of a large number of charged particles at the same time with simple algorithms, it is applicable only to “collisionless” plasmas with very low collision frequencies. Thus, the PIC simulation cannot treat close binary interactions between neighboring charged particles. However, in most glow-discharge plasmas such as the IEC plasmas, collisions between charged particles and background neutral particles are not ignorable. Those collisions determines the electron mobility in the plasma and affects the populations of various types of particles (ions and neutral particles) through numerous collisional reactions such as

ionization, recombination and charge exchange.

On the other hand, the MC method is used to find solutions to complex problems based on statistical processes. In typical cases, a test particle is first generated by determining its position and velocity randomly based on the distribution function, and then whether or not it collides with another particle during its motion is also determined randomly based on the cross section data for each collisional reaction. The test particle is tracked until it is finally lost in the system and all collisional processes and secondary particles generated by the particles are recorded. By repeating this procedure for considerable number of test particles and secondary particles, we can simulate the phenomena with sufficient statistical accuracies.

The PIC-MCC method uses the MC algorithm to take into account collisional processes in the PIC plasma simulation[3], which has been often used to examine the behavior of low-temperature plasmas[4]. In electrostatic cases, the calculation procedure of the PIC-MCC method is as follows:

1. Generate initial particles.
2. Distribute the charges of particles to grids.
3. Solve the Poisson equation based on the charge densities on grids.
4. Calculate electric fields at particle positions.
5. Accelerate particles by the electric field and move them.
6. Judge whether or not particles collide with background gas molecules using the MC method.
7. Repeat above from the second step.

In the present study, the following five major collisional processes were considered:

- $e + H_2 \rightarrow e + H_2$ (elastic)
- $e + H_2 \rightarrow 2e + H_2^+$ (ionization)
- $H_2^+ + H_2 \rightarrow \text{fast } H_2 + H_2^+$ (charge exchange)
- $H_2^+ + H_2 \rightarrow \text{fast } H_2^+ + H_2^+ + e$ (ionization)
- $H_2 + H_2 \rightarrow \text{fast } H_2^{(+)} + H_2^{(+)} + e$ (ionization)

To calculate the probabilities of these collisions, we used the cross-section data compiled by Phelps[5] and Tabata, *et al.*[6]

In the present study, we started the PIC-MCC simulation with few couples of electrons and H_2^+ ions randomly located in the gap, and then tracked all particles including secondary particles produced through the above reactions. Backscattering of

energetic electrons incident to the anode was also taken into account[7].

3. Results and Discussion

In Fig. 2, the velocities and positions of the particles 2.8 μs and 5.6 μs after discharge ignition are plotted in phase diagrams. This simulation was performed by assuming that a voltage of 100 kV was applied between plain electrodes and the gap was filled with a hydrogen gas of 1.25 Pa. As you can see in the figures, the number of ions increases rapidly with time due to ionization reactions caused by electrons and ions. The number of fast atoms also increases drastically with time due to charge exchange reactions between ions and background neutral molecules. Since electrons are very light compared with ions and neutral particles, they are easily accelerated by the electric field and quickly move towards the anode (left boundary). So, at beginning of the calculation ($t = 2.8 \mu\text{s}$), almost all electrons are lost at the cathode immediately after their productions and much heavier ions and neutral particles are left behind. However, the

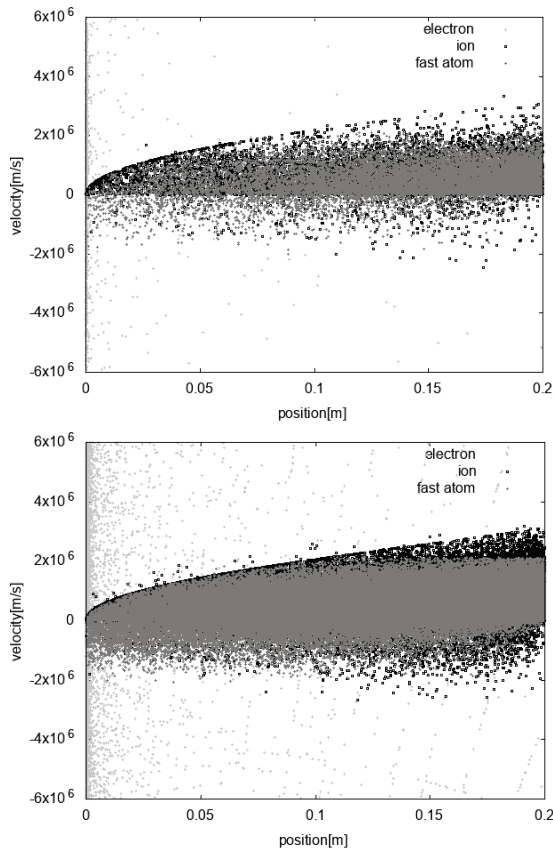


Fig. 2. Typical particle distributions in the gap (upper: $t = 2.8 \mu\text{s}$, lower: $t = 5.6 \mu\text{s}$).

electrostatic potential in the gap gradually rises, eventually suppressing the loss of electrons to the cathode. Due to this effect, it can be seen that the number of electrons near the cathode is increasing at $t = 5.6 \mu\text{s}$.

Figure 3 plots the electrostatic potential profiles at 2.8 μs and 5.6 μs in the discharge gap. One can see that the potential gradually rises with time due to space charge effect of ions in the gap. If we continue the calculation, the potential will rise beyond zero, and then the electrons will be trapped in the potential well to cancel the positive charge of ions. In other words, a plasma will begin to form near the cathode.

3.2 Characteristics of basic IECF setup

Figure 4 shows the relationship between the discharge starting voltage and the background gas pressure based on the PIC-MCC calculations in this study. The discharge starting voltage decreases with increasing gas pressure, which is similar to the tendency of the Paschen's curve with pd products smaller than $pd_{(\text{min})}$. Here, p is the gas pressure and d

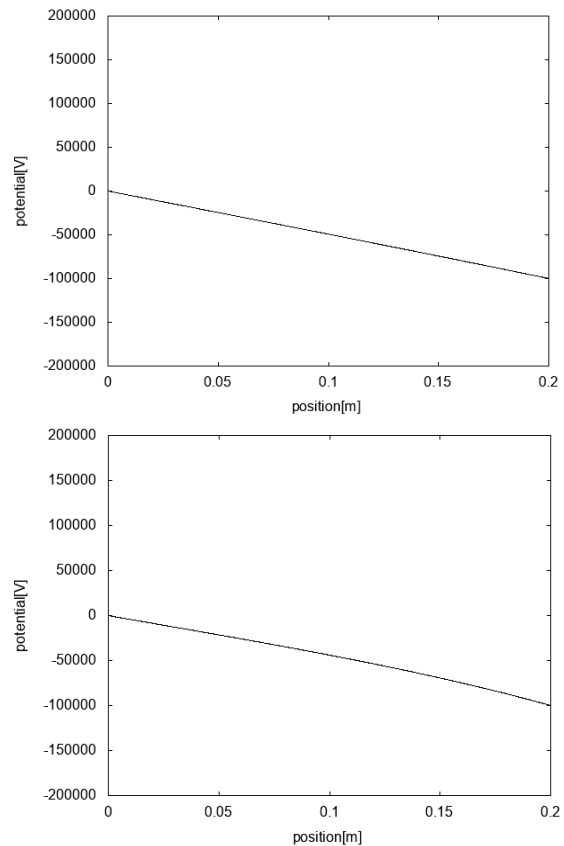


Fig. 3. Typical profiles of electrostatic potential in the gap (upper: $t = 2.8 \mu\text{s}$, lower: $t = 5.6 \mu\text{s}$).

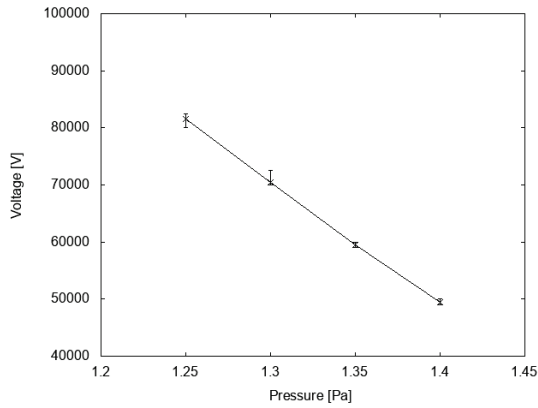


Fig. 4. Calculated dependency of discharge starting voltage on gas pressure.

is the gap length, and $pd_{(\min)}$ is a value where the discharge starting voltage becomes minimum.

Although there remain some discrepancies between the experiment results and the simulation results, we could qualitatively reproduce the high-voltage glow discharge properties with our PIC-MCC code.

4. Conclusions

In this study, we analyzed particle motions and interactions in a one-dimensional glow discharge gap while considering the space charge effect by using an originally developed 1D PIC-MCC code. The PIC-MCC simulations quantitatively reproduced the Paschen's theoretical curve, which is commonly used to predict the voltage with which the discharge initiates in low-pressure gas. However, there are still some problems to be solved. In the future, we will improve the PIC-MCC code by considering the other particles such as H, H⁺, H⁻, and H₃⁺. In addition, conservations of energy and momentum in each collisional process should be satisfied more strictly. To compare the simulation results with those obtained with actual IEC device in our lab, the simulation must consider the multidimensional effects and the external circuit. These improvement will be done based on the present PIC-MCC code in near future.

References

- [1] Jun Hasegawa, et al., "Recent progress on inertial electrostatic confinement fusion neutron sources", *Reza Kenkyu*, **46**, 589 – 593 (2018).
- [2] C. K. Birdsall and A. B. Langdon, "Plasma Physics

via Computer Simulation", *CRC Press*, (2004).

- [3] C. K. Birdsall, "Particle-in-cell charged-particle simulations, plus Monte Carlo collisions with neutral atoms, PIC-MCC", *IEEE Transactions on Plasma Science*, **19**, pp.65–85, 1991

- [4] Liang Xu, et al., "Investigation of the Paschen curve for helium in the 100 – 1000 kV range", *Physics of Plasmas*, **24**, 093511 (2017).

- [5] A.V. Phelps, "Cross sections and swarm coefficients for H⁺, H₂⁺, H₃⁺, H, H₂, and H⁻ in H₂ for energies from 0.1 eV to 10 keV", *Journal of Physical and Chemical Reference Data*, **19**, 653–675 (1990).

- [6] Tatsuo Tabata and Toshizo Shirai, "Analytic cross sections for collisions of H⁺, H₂⁺, H₃⁺, H, H₂, and H⁻ with hydrogen molecules", *Atomic Data and Nuclear Data Tables*, **76**, 1–25 (2000).

- [7] E. H. Darlington. Backscattering of 10-100 keV electrons from thick targets. *Journal of Physics D: Applied Physics*, **8**, 85-93(1975).

Numerical simulation for behavior of multi-ion-species plasma in perpendicular magnetic field

Taichi Takezaki¹, Kyohei Osawa¹, Seigo Kato¹, Takuya Oguchi¹,
Kazumasa Takahashi², Toru Sasaki², Takashi Kikuchi², and Hiroaki Ito¹

¹*University of Toyama, Gofuku 3190, Toyama Toyama 930-8555, Japan*

²*Nagaoka University of Technology, Kamitomioka 1603-1, Nagaoka Niigata 940-2188, Japan*

ABSTRACT

We have investigated the behavior of the collisionless multi-ion-species plasma flowing into a perpendicular magnetic field by using a numerical simulation based on an electromagnetic hybrid particle-in-cell method. The plasma parameters as initial conditions, resulting from the compact pulsed-power discharge experiment, are the drift velocity of 30 km/s, the ion number density of 10^{20} m^{-3} , and the ion temperature of 3 eV. The behavior when the multi-ion-species plasma, consisting of helium and argon, injects into the perpendicular magnetic field has been calculated. The numerical results showed that the maximum velocity of the accelerated helium ion increases by mixing the argon ion. The results indicate that the effect of the multi-ion-species improve the efficiency of the particle acceleration in collisionless shocks.

Keywords

Collisionless plasma, multi-ion-species, hybrid particle-in-cell

1. Introduction

Understanding of the energy dissipation process of a plasma flow and the generation process of high energy particles in collisionless plasma with electromagnetic fields is an interesting issue in space plasma physics. Shock phenomena occurring in collisionless plasma have an important role for generating high energy particles in outer space, called as cosmic rays (CRs) [1,2]. Bell and Blandford have explained that the velocity difference between the upstream and the downstream caused by the shock structure statistically accelerates charged particles, and the energy distribution becomes the non-thermal power-law spectrum [3-5]. However, the detailed processes of the formation of the shock structure with the electromagnetic fields and/or the injection problem of the charged particles to ride the electromagnetic waves have been not clarified [6,7].

Experimental simulations of collisionless shocks in laboratory-scale experiments provide the in-situ

observation of the plasma behavior and the electromagnetic fields [8,9]. The experiments using high-power laser facilities drive a collisionless plasma flow with the drift velocity of around 1000 km/s, which is same order as supernova remnants. Recently, the high-power laser experiments have been energetically carried out, and the observation results of the collisionless shocks such a electrostatic shock [10,11], a Weibel-mediated shock [12,13], and a magnetized shock [14,15] have been reported. On the other hands, we have proposed an experiment for simulating collisionless shocks using a compact pulsed power discharge device [16-18]. The tapered cone plasma focus device (TCPFD) is able to drive a quasi-one-dimensional fast plasma flow with the velocity of 30 km/s in a helium gas discharge [17]. The velocity of the plasma flow driven by the TCPFD is very low compared with the high-power laser experiment. However, the phenomenon driven by the pulsed power experiment is able to compare with the

results in the high-power laser experiment by applying a suitable strength of a magnetic field to the plasma flow. Moreover, the gas discharge experiment is easily able to control the ion-species, the mixing ratio, and the ion number density of the plasma. And thus, it is easy to experimentally investigate the effect of the multi-ion-species on the plasma behavior compared with the high-power laser experiment.

In this study, we have numerically investigated the behavior of the collisionless multi-ion-species plasma flowing into a perpendicular magnetic field by using an electromagnetic hybrid particle-in-cell (PIC) method. The effect of the multi-ion-species on the plasma behavior driven by the TCPFD are predicted.

2. Setup of Numerical Simulation

To investigate the behavior of the plasma flow generated by the TCPFD in the external magnetic field, we have performed the numerical simulation based on the electromagnetic hybrid PIC method [17,18]. In the hybrid PIC method, ions are treated as particles and electrons are treated as a massless fluid. Since the ions are treated as particles, the hybrid PIC method is able to discuss the kinetic effect of ions. Moreover, since the electrons are treated as the massless fluid, the time step of the calculation is decided by the time scale of the ion motion, and the calculation load is small compared with a full PIC method.

The numerical simulations are carried out the four dimensional phase space (x, v_x, v_y, v_z) . Figure 1 shows the initial conditions of the numerical simulations. The calculation region is from -10 mm to 20 mm. Super particles representing the ions are placed from -10 mm to 0 mm. The velocity distribution function of the ions is decided by a drift Maxwellian distribution with the drift velocity of $U_x = 30$ km/s and the ion temperature of $T_p = 3$ eV. The region from 0 mm to 20 mm indicates the ambient vacuum region. The external perpendicular magnetic field B_z with the peak of 25 mT at 10 mm is applied to the ambient region.

To discuss the effect of the multi-ion-species, we calculated the behavior of the plasma flow consisting of helium (He) ions and argon (Ar) ions. The charge state of both He and Ar is $Z = 1$. The total ion number

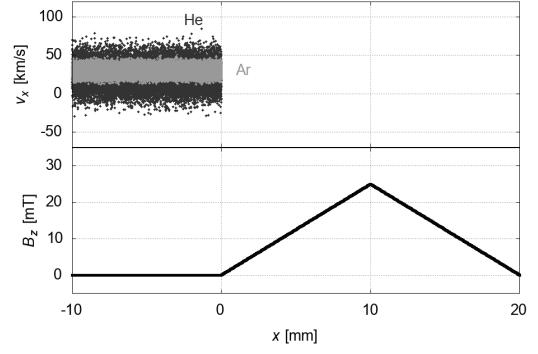


Fig. 1 Initial conditions for simulating the multi-ion-species plasma driven by the compact pulsed-power device.

density is constant at $n_p = 10^{20} \text{ m}^{-3}$. The relation between n_p , He ion number density n_{He} , and the Ar ion number density n_{Ar} is described as below:

$$n_p = n_{\text{He}} + n_{\text{Ar}} \quad (1)$$

We define a mixing ratio η as below:

$$\eta = \frac{n_{\text{Ar}}}{n_p} \quad (2)$$

Therefore, the He ion number density n_{He} and the Ar ion number density n_{Ar} are decided by the η as below:

$$n_{\text{Ar}} = \eta n_p \quad (3)$$

$$n_{\text{He}} = (1 - \eta) n_p \quad (4)$$

3. Results and Discussion

Figure 2 and Fig. 3 show the behavior of the single-ion-species plasma and the multi-ion-species plasma in the perpendicular magnetic field, respectively. In the both cases, the accelerated He ions exist in front of the plasma flow with the compression of the perpendicular magnetic field. In the comparison of Fig. 2(b) and Fig. 3(b), the maximum velocity of the accelerated He ion of around 140 km/s in the multi-ion-species plasma is higher than the maximum velocity of around 130 km/s in the single-ion-species plasma. Moreover, the peak of the compressed magnetic field of 43 mT in the multi-ion-species plasma is higher than one of 36 mT in the single-ion-species plasma.

When the plasma flowed into the perpendicular magnetic field, the magnetic field are compressed. The

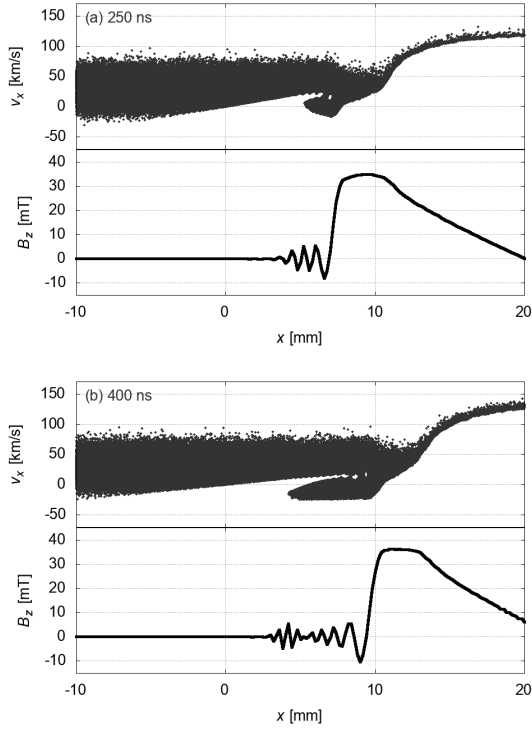


Fig. 2 Time evolution of the x - v_x ion phase space and the magnetic field in the single-ion-species plasma of He ($\eta = 0$).

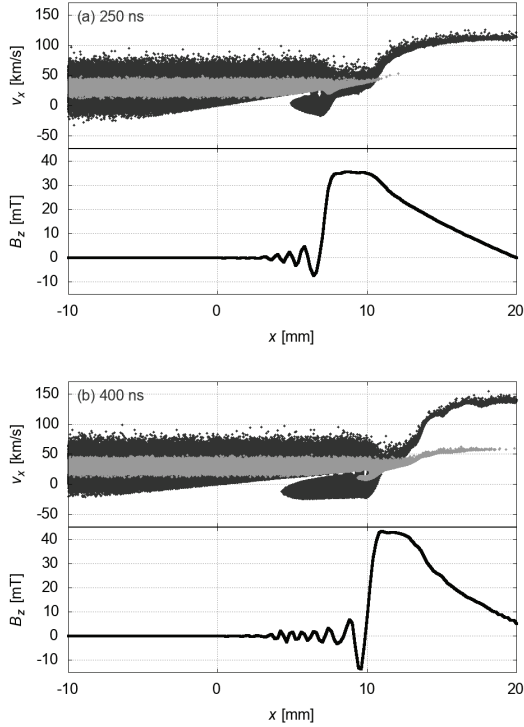


Fig. 3 Time evolution of the x - v_x ion phase space and the magnetic field in the multi-ion-species plasma of He and Ar ($\eta = 0.5$).

modulated magnetic field induces the electric field, and the electric field accelerates some ions [18]. The peak of the compressed magnetic field is decided by the balance between the plasma kinetic pressure and the magnetic pressure. By mixing the Ar ions into the He ion plasma, the peak of the compressed magnetic field increased with increasing the kinetic pressure of the plasma. And thus, the induced electric field increased with increasing the compressed magnetic field, and the maximum velocity of the accelerated ions increased. The results indicate that heavy ions (Ar) affects the efficiency of the particle acceleration of light ions (He) in collisionless shocks.

4. Conclusions

The numerical results calculated by the hybrid PIC method showed that the maximum velocity of the accelerated He ion increases by mixing the Ar ion. By mixing the Ar ions into the He ion plasma, since the peak of the compressed magnetic field increased with increasing the plasma kinetic pressure, the induced electric field also increased. The results indicate that heavy ions (Ar) affects the behavior of behavior of light ions (He) through the electromagnetic field, in collisionless multi-ion-species plasma.

References

- [1] R.P. Drake, “High-energy-density physics: fundamentals, inertial fusion, and experimental astrophysics”, Springer, 2006.
- [2] W. Baumjohann, *et al.*, “Basic Space Plasma Physics”, World Scientific Publishing Company, 2012.
- [3] S.P. Swordy, “The energy spectra and anisotropies of cosmic rays”, *Space Sci. Rev.* **99**, 85, 2001.
- [4] A.R. Bell, “The acceleration of cosmic rays in shock fronts - I”, *Mon. Not. R. Astron. Soc.* **182**, 147, 1978.
- [5] R.D. Blandford, *et al.*, “Particle acceleration by astrophysical shocks”, *Astrophys. J.* **221**, L29, 1978.

- [6] R. Treumann, “Fundamentals of collisionless shocks for astrophysical application, 1. non-relativistic shocks”, *Astron. Astrophys. Rev.* **17**, 409–535, 2009.
- [7] Y. Ohira, “Cosmic ray acceleration mechanism”, *JPS Conf. Proc.* **15**, 011002, 2017.
- [8] R.P. Drake, “The design of laboratory experiments to produce collisionless shocks of cosmic relevance”, *Phys. Plasmas* **7**, 4690, 2000.
- [9] D.D. Ryutov, *et al.*, “Magnetohydrodynamic scaling: From Astrophysics to the laboratory”, *Phys. Plasmas* **8**, 1804, 2001.
- [10] T. Morita, *et al.*, “Collisionless shock generation in high-speed counterstreaming plasma flow by a high-power laser”, *Phys. Plasmas* **17**, 122702, 2010.
- [11] Y. Kuramitsu, *et al.*, “Time evolution of collisionless shock in counterstreaming laser-produced plasmas”, *Phys. Rev. Lett.* **106**, 175002, 2011.
- [12] C.M. Huntington, *et al.*, “Observation of magnetic field generation via the Weibel instability in interpenetrating plasma flows”, *Nat. Phys.* **11**, 173-176, 2015.
- [13] F. Fiuza, *et al.*, “Electron acceleration in laboratory-produced turbulent collisionless shocks”, *Nat. Phys.* **16**, 916-920, 2020.
- [14] C. Niemann, *et al.*, “Observation of collisionless shocks in a large current-free laboratory plasma”, *Geophys. Res. Lett.* **41**, 7413, 2014.
- [15] D.B. Shaeffer, *et al.*, “Direct observations of particle dynamics in magnetized collisionless shock precursors in laser-produced plasmas”, *Phys. Rev. Lett.* **122**, 245001, 2019.
- [16] T. Sasaki, *et al.*, “Laboratory scale experiments for collisionless shock generated by taper-cone-shaped plasma focus device”, *JPS Conf. Proc.* **1**, 015096, 2014.
- [17] T. Takezaki, *et al.*, “Accelerated ions from pulsed-power-driven fast plasma flow in perpendicular magnetic field”, *Phys. Plasmas* **23**, 062904, 2016.
- [18] T. Takezaki, *et al.*, “Particle acceleration mechanism due to interaction between one-dimensional fast plasma flow and perpendicular magnetic field”, *High Energy Density Phys.* **33**, 100698, 2019.

Relaxation Process of Electron Beam Injected into a Malmberg–Penning Trap

Ishii Hiroshi, Yukihiro Soga, Youngsoo Park*, Nozomi Suzutani**, and Takashi Kikuchi**

Kanazawa University, Kanazawa, 920-1192, Japan

**National Institute of Technology, Anan College, Tokushima, 774-0017, Japan*

***Nagaoka University of Technology, Nagaoka, 940-2188, Japan*

ABSTRACT

Relaxation process of a pure electron plasma generated by injecting an electron beam into a Malmberg–Penning trap is experimentally investigated in this article. An abrupt broadening of the axial energy distribution function was observed at a holding time of 1 μ s. This relaxation occurred faster than the expected time scale of Coulomb collisions. As shown by the experiments, the broadening of the energy profile was enhanced by the weak confinement electric field at the axial reflection point of electrons.

Keywords

Pure Electron Plasma, Malmberg–Penning Trap, Space-Charge Dominated Beam, HIF, Relaxation Process

1. Introduction

A heavy-ion beam inertial confinement fusion (HIF) system is a promising energy source for the next generation. In the HIF system, an abrupt pulse compression operation of heavy-ion beams is required in the final stage of the energy driver to provide adequate energy to a target [1,2]. A rapid increase in the current density generates a high space-charge effect, which increases the beam emittance, preventing the efficient fusion reaction. A method for controlling the increase in beam emittance after the dramatic compression is yet to be studied. However, the experimental study on such space-charge dominated beam [3] in a large accelerator complex is expensive.

Pure electron plasma (PEP) is a population of only electrons and can be confined for a long time in the Malmberg–Penning trap. The technique to observe its dynamics has been established [4,5]. As shown in Fig. 1, it has been theoretically shown that the dynamics of PEP in the magnetic field cross-section are equivalent to those of a charged particle beam seen from the beam coordinate [6]. However, no experiments have been

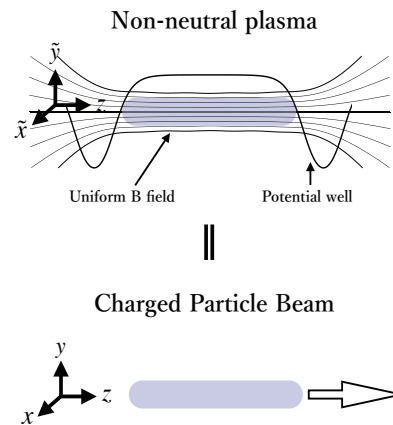


Fig. 1 Dynamics of a pure electron plasma trapped in a uniform magnetic field and potential well are equivalent to those of a charged particle beam.

performed using PEPs trapped in the Malmberg–Penning trap to simulate a charged particle beam.

To understand the dynamics of the space-charge dominated beam, we conducted simulated experiments by observing energy transport in PEPs to find the appropriate beam-handling system in a HIF

system, exploiting the fact that PEPs behave equivalently to heavy-ion beams. In this article, we performed preliminary experiments to observe the time evolution of the axial energy profile of PEP generated by injecting an electron beam. The PEP has two opposite streams in the confinement region, which is equivalent to a charged particle beam in the pulsed compression process required for the energy driver of the HIF system.

2. Experimental Setup and Method

The experiment was conducted using a Malmberg–Penning trap of Kanazawa University (Fig. 2). A uniform magnetic field with a flux density of 0.1 T was generated via a series of pancake-type coils. A potential well is created by applying voltage of up to a -80 V to the ring electrodes at both ends [5].

Figure 3 shows the experimental procedure for injection, confinement, and observation of PEP. An electron beam emitted from a thermionic cathode at an acceleration voltage of 20 V is introduced into the confinement region (Fig. 3(a)). The observed PEP had electron density of $1.3\text{--}1.6 \times 10^{\text{m}^{-3}}$, diameter of 1.5 mm, and length of 230 mm. In the initial stage of confinement, PEP flows back and forth in the axial direction between the confinement potentials, forming two streams (Fig. 3(b)). After confinement for an arbitrary time, the potential barrier became shallower on one side, and the number of escaped electrons overcoming the barrier was observed from the brightness intensity of the phosphor screen (Fig. 3(c)).

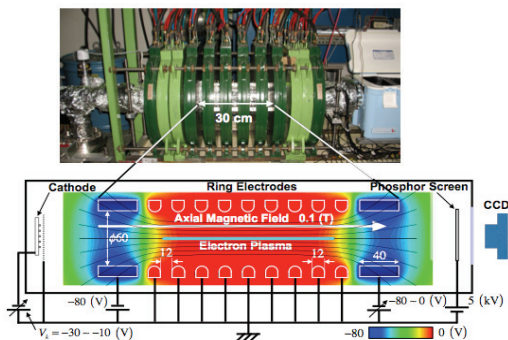


Fig. 2 External view (top) and cross-sectional view (bottom) of the experimental setup. The gray scale shows a typical confinement potential distribution.

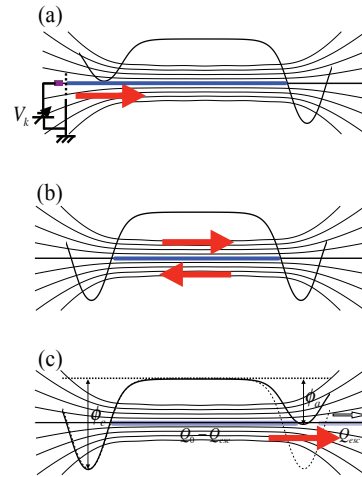


Fig. 3 (a) Electrons are injected with constant energy from the electron gun while the potential barrier is temporarily eliminated, (b) back and forth movement between the potential barriers while it is confined, and (c) flow out after an arbitrary time to observe the energy distribution function.

We repeated the above destructive measurements for another PEP with the same parameters, varying the potential barrier, and the escaping electrons were measured as a function of the barrier voltage. The axial energy distribution function can be obtained by differentiating the escaping electron data using barrier energy [7]. The relaxation process of PEP injected as an electron beam into an equilibrium state was traced via observing the time evolution of the axial energy distribution function.

3. Results

3.1 Long-time evolution of energy distribution

Figure 4 shows the long-time evolution of the axial energy profile of PEP injected at an acceleration voltage of 20 V. Initial distribution was assumed to be a drifting Maxwell distribution with drifting energy of 20 eV and thermionic cathode temperature of 0.05 eV (Fig. 4(a)). Boltzmann distribution was achieved in 50 ms after initializing the confinement, indicating that the thermal equilibrium state was realized (Fig. 4(d)). Because Coulomb collision time was estimated to be several ms, we concluded that the relaxation to the thermal equilibrium state was because of the Coulomb

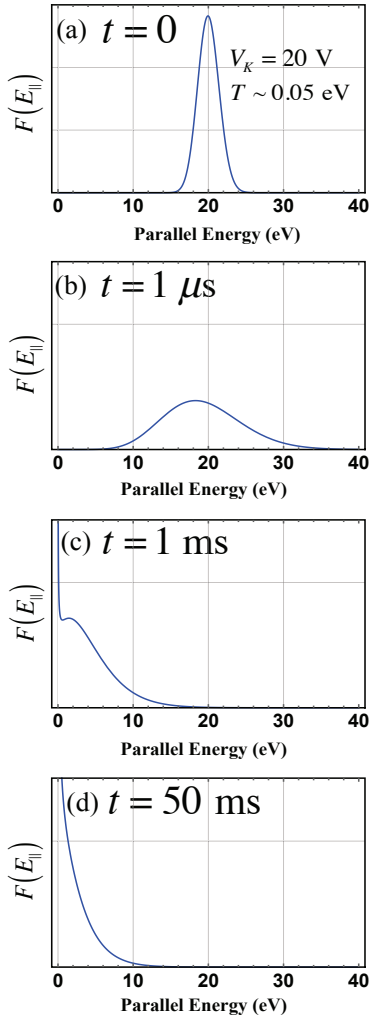


Fig. 4 Time evolution of the energy distribution function of PEP injected with an acceleration voltage of 20V. Significant relaxation of the distribution function is observed at $1 \mu\text{s}$, which is faster than the Coulomb collision time (b).

collisions.

Moreover, rapid relaxation was observed at $1 \mu\text{s}$, which occurred much faster than the Coulomb collision (Fig. 4(b)). The energy distribution suddenly broadened from the one estimated by making use of the beam injection conditions shown in Fig. 4(a). The mechanism of this anomalously rapid relaxation of the energy distribution was unclear.

3.2 Relaxation immediately after beam injection

Preliminary simulation calculations suggested that the mechanism of the anomalous rapid relaxation

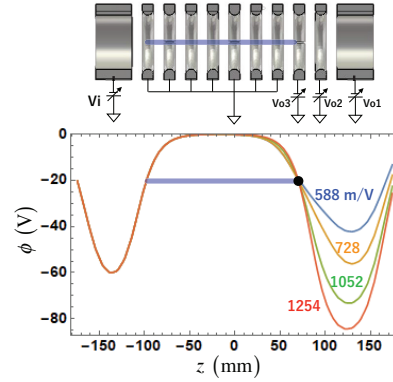


Fig. 5 Confinement potential configurations generated by independently applying voltage to the electrodes.

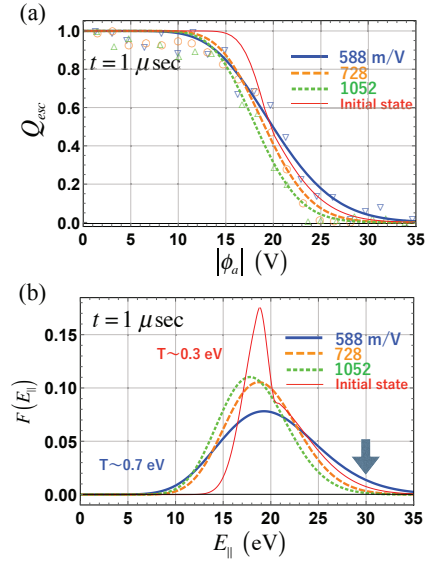


Fig. 6 Normalized escaping electrons as a function of the barrier voltage during energy analysis for PEP with a confinement time of $1 \mu\text{s}$ (a), and the energy distribution function (b).

observed in this study depends on the confinement electric field strength. To experimentally verify the dependence of the rapid relaxation on the electric field strength, we prepared four different confinement field distributions, where the electric field strengths at one reflection point were varied (Fig. 5). Figure 6 shows the results of the energy distribution function of PEP after $1 \mu\text{s}$ confined under these conditions. At 588 V/m, which is the lowest electric field strength, there were significantly more electrons overcoming the barrier potential of -30 V than in other electric field strength conditions (Fig. 6(a)). The energy distribution

function, which was obtained by differentiating the data of Fig. 6(a), showed a difference in the tail of the distribution, and the weaker the electric field at the reflection point, the more the energy distribution function extended to higher energies (Fig. 6(b)). The observation clearly showed that the rapid relaxation at 1 μ s was enhanced under the weak electric field at the reflection point.

4. Discussion

It was found that PEP injected as an electron beam had an abrupt spread in axial energy distribution function at a holding time of 1 μ s, and the weaker the electric field at the reflection point, the more energetic particles were generated. A quantitative evaluation of this relaxation process using the temperature defined from the dispersion of the axial velocity showed that the temperature increased from 0.3 eV at the initial state to 0.7 eV with a field strength of 588 m/V. Although the relaxation proceeded rapidly in terms of the temperature increase, the quantitative relationship between the electric field strength and the temperature, average axial energy, and change in radial energy were unclarified.

The observed dependence of the rapid relaxation on the confinement field was qualitatively consistent with the preliminary results of the 3D particle simulation. Other simulations of fast particle generation in PEPs using the same calculation method reproduced the experimental results [8,9]; therefore, the calculation results for this rapid relaxation phenomenon could be reliable. However, the mechanism of the relaxation is unclear.

5. Conclusions

The anomalous rapid relaxation process of PEP injected as an electron beam into the Malmberg–Penning trap was experimentally observed in this article. Energy distribution function at a holding time of 1 μ s was measured by experimentally controlling the electric field strength at the reflection position. It was found that the weaker the electric field, the more energetic particles were produced. The observation clearly shows that the rapid relaxation is enhanced

under the weak electric field at the reflection point.

References

- [1] T. Kikuchi et al., “Beam dynamics during longitudinal bunch compression of high-current heavy-ion beams”, *Nucl. Instr. Meth. Phys. Res. A577*, pp.103-109 (2007).
- [2] K. Horioka, “Progress in particle-beam-driven inertial fusion research: Activities in Japan”, *Matter and Radiation at Extremes*, 3, pp.12-27 (2018).
- [3] M. Reiser, “Theory and Design of Charged Particle Beams”, Wiley (1994).
- [4] J. H. Malmberg et al., “Experiments with Pure Electron Plasmas”, *Physica Scripta T2*, 288 (1982).
- [5] Y. Soga et al., “Mechanisms of $E \times B$ Drift Rotation of a Vortex String in a Pure Electron Plasma”, *Plasma Fusion Res.* 8, 2401034 (2013).
- [6] H. Okamoto et al., “Proposed experiments for the study of beam halo formation”, *Nucl. Instr. Meth. Phys. Res. A* 437, pp.178-187 (1999).
- [7] D. L. Eggleston et al., “Parallel energy analyzer for pure electron plasma devices”, *Physics of Fluids B: Plasma Physics*, 4, pp.3432-3439 (1992).
- [8] Nozomi Suzutani et al., “Numerical Analysis of Relaxation Process with Fast Particle Generation in Malmberg–Penning Trap Experiment for Ion Beam Inertial Fusion”, *High Energy Density Physics Volume 36*, 100828 (2020).
- [9] Nozomi Suzutani et al., “Study on Softening Parameter for Multi-Particle Simulation in Malmberg–Penning Trap Experiment”, *Transaction of the Japan Society for Simulation Technology*, 12, 1, pp.15-20 (2020).

Analysis of cluster ions directly generated from laser ablation plasma cooled in ambient helium gas

Takuma JINNAI, Jun HASEGAWA

Tokyo institute of technology, Ookayama Meguro-ku, Tokyo 152-8550, Japan

ABSTRACT

In this study, we performed mass spectrometry and ion flux measurement of cluster ions supplied directly from a laser ablation cluster source. By applying a high voltage pulse to the acceleration gap of the TOFMS, the signal of such “pre-charged” aluminum cluster ions was successfully observed. The result showed that the pre-charged cluster ions were distributed in the smaller size compared to the neutral clusters. In addition, the TOFMS and ion flux measurements revealed that the beam bunch was composed of two components having different drift velocities. The faster component was found to contain more monoatomic ions and pre-charged cluster ions, while the slower one contains more neutral atoms and neutral clusters.

Keywords

Cluster, Ion source, Laser ablation plasma, Supersonic jet, Time-of-flight mass spectrometry, Delayed extraction

1. Introduction

When giant cluster ions such as C_{60} fullerenes are incident on a solid material, peculiar phenomena such as crater formation[1], improvement of sputtering yield[2], and increase of stopping power[3], are known to occur. Although many studies have been conducted on the irradiation effects of cluster ion beams, the energy per nucleon is limited to at most 100 keV/u due to the upper limit of the terminal voltage of electrostatic accelerator. Therefore, previous cluster ion irradiation experiments with bulk material targets were limited to surface interactions. On the other hand, if giant cluster ions are accelerated to energies more than 1 MeV/u and irradiated into the bulk target, an extremely high energy density state is considered to be formed in the target, which cannot be achieved with conventional monoatomic ion beams. This property of energetic cluster ions is expected to be applied to new ion implantation technology and ultimately to energy drivers of inertially confined fusion reactors.

To accelerate charged particles to such high energies, it is necessary to accelerate them repeatedly using a circular accelerator. However, in conventional circular accelerators such as synchrotrons, the mass-to-charge

ratio of the ions that can be accelerated is strictly limited by the bandwidth of the RF power supply. Therefore, it has been impossible to accelerate ions with extremely low charge-to-mass ratio ($q/m < \sim 10^{-2} - 10^{-3}$), such as fullerene ions.

In recent years, however, Takayama *et al.* demonstrated that ion circular acceleration without bandwidth constraints is possible by combining semiconductor switching technique with inductive acceleration cells[4], and pointed out that this method can accelerate also large cluster ions such as C_{60} to energies as high as order of MeV/u[5]. The circular induction accelerator requires the cluster ion source to repeatedly provide high flux cluster ions in a period of $\sim 10 \mu\text{s}$. The controllability of the cluster size is also required to the cluster source to efficiently supply cluster ions having a specific charge-to-mass ratio as many as possible.

In our previous studies, we investigated the flux waveforms of silicon or aluminum clusters supplied from a laser ablation cluster source in detail by time-of-flight mass spectrometry (TOFMS)[6]. In this study, only neutral clusters transported from the cluster source were analyzed after ionizing them by a pulsed

UV laser in the acceleration gap of the TOFMS system. On the other hand, it has been reported that in the laser ablation cluster source, in addition to the neutral cluster, pre-charged cluster ions are also generated at the same time[7,8]. If the amount of these pre-charged cluster ions is sufficiently high, we can provide them directly to the post accelerator, which means that the process of ionizing neutral clusters becomes unnecessary and particle loss due to the dissociation of clusters can be prevented.

The purpose of this study is to measure the mass distribution and the flux waveforms of pre-charged cluster ions generated in the laser ablation cluster source. The mass distribution of the cluster ions is investigated by the TOFMS combined with a delayed extraction method. We also investigate the flux waveforms of the cluster beam by using a Channeltron detector.

2. Experimental Setup

Figure 1 shows the cross-sectional view of the laser ablation cluster source developed in this study. A frequency-doubled Nd:YAG laser ($\lambda=532$ nm, 5 ns FWHM, 5 Hz) was adopted to irradiate an aluminum cylindrical target and generate aluminum vapor. The laser spot was elliptical and typically has an area of $0.2 \times 0.4 \pi \text{ mm}^2$. The fluence of the ablation laser was fixed at 41 J/cm^2 throughout this study. To improve the reproducibility of the vapor generation, the target was rotated at about 12 rpm by a motorized rotational stage. This function suppresses unstable vapor generation due to the large deformation of the target surface. Helium gas was supplied to the waiting room with a pressure of $\sim 1 \text{ MPa}$ for 1 ms through a fast solenoid valve prior to the laser irradiation. The timing of the laser irradiation with respect to the valve opening (typically $750 \mu\text{s}$) was controlled by a delay pulse generator so that the vapor generation could occur when the waiting room was pre-filled by high-pressure helium gas and a supersonic helium gas flow was established in the nozzle section. The aluminum vapor containing aluminum cluster particles was transported downstream by the supersonic flow through a conical nozzle with an opening angle of 3 degrees.

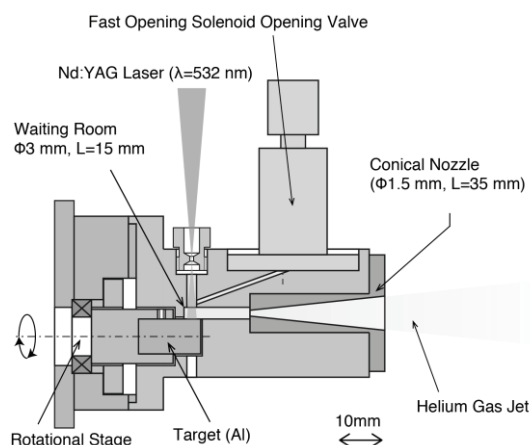


Fig. 1. The cross-sectional view of the laser ablation cluster source developed in this study.

Figure 2 shows the whole structure of the experimental equipment consisting of three vacuum chambers: a cluster source chamber, a drift chamber, and an analyzer chamber. During the operation, the background pressures of these chambers were, respectively, maintained at $\sim 10^{-2} \text{ Pa}$, $\sim 10^{-4} \text{ Pa}$, and $\sim 10^{-6} \text{ Pa}$ by turbo molecular pumps. To sustain the large pressure difference between the source chamber and the drift chamber, they were separated by coaxially arranged two skimmers ($\phi 1.5 \text{ mm}$ and $\phi 3 \text{ mm}$), which work also as collimators of the cluster beam supplied from the supersonic nozzle. An aperture ($\phi 3 \text{ mm}$) was additionally located in front of the analyzer chamber, so only the cluster particles with good directivity were delivered to the TOFMS section.

In the mass spectrometry of neutral clusters, a deflection voltage of about -500 V was constantly

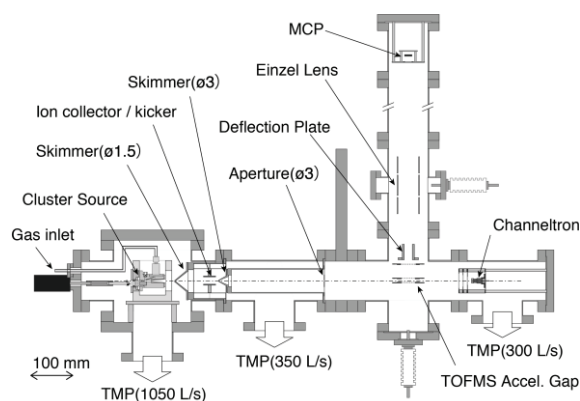


Fig. 2. Experimental setup for mass spectrometry and flux waveform measurement.

applied to a beam kicker placed between the two skimmers to remove the charged particles supplied from the cluster source. As a result, only neutral particles were introduced into the acceleration gap of the TOFMS system. When the center of the acceleration gap was irradiated by a KrF excimer laser ($\lambda=248$ nm, 30 ns FWHM), a fraction of neutral particles in the beam were ionized and then accelerated perpendicularly to the beam axis. After two-stage acceleration (1.25 kV and 18.5 kV), these ions were accelerated to around 20 keV and then focused by an einzel lens onto a MCP detector.

In measuring pre-charged clusters, a part of the cluster beam was sliced in the time domain with the kicker and then introduced into the acceleration gap of the TOFMS system. In this case, no acceleration voltage was applied until the beam reaches the accelerating gap. Shortly after the beam particles including pre-charged clusters enter the accelerating gap, a pulsed high voltages (3.24 kV and 3.00 kV) were applied to the two-stage gap and only pre-charged particles were accelerated perpendicularly to the beam axis and analyzed.

In addition to the TOFMS system, a Channeltron detector was installed coaxially with the beam axis 15.5 cm downstream of the TOFMS acceleration gap so as to measure the flux waveform of charged and neutral particles supplied from the cluster source.

3. Results and Discussion

Figure 3 shows typical TOF signals obtained by the TOFMS system using the delayed extraction method. The lower horizontal axis shows the TOF of the detected particles from the acceleration gap to the MCP detector, and the upper one shows the cluster size (number of Al atoms) corresponding to the TOF. The upper waveform was obtained without ionization laser irradiation, so it is considered due to pre-charged cluster ions directly generated in the cluster source. The lower waveform was obtained with ionization laser irradiation to the acceleration gap of the TOFMS system. In this case, neutral clusters probably dominate the signal. Although there is room for improvement in the mass resolution and the S/N ratio,

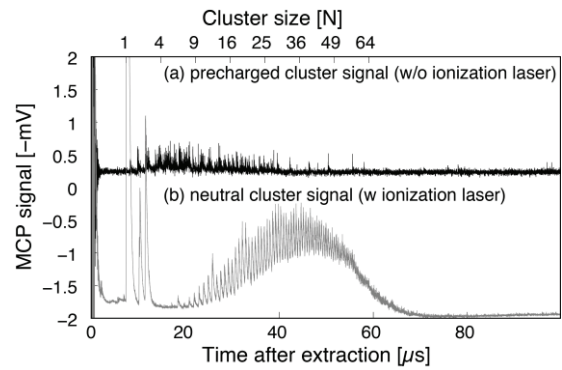


Fig. 3. Typical TOF signals obtained by the delayed extraction method: (a) pre-charged cluster ions, (b) neutral clusters.

we successfully observed the cluster ions directly

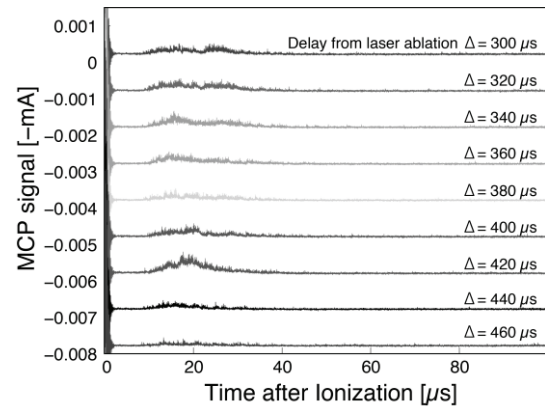


Fig. 4. TOF signals observed with various extraction delays from 300 to 460 μ s.

generated from the laser ablation cluster source using the delayed extraction method. Compared to the mass distribution of neutral clusters, the pre-charged clusters are found to have relatively small sizes.

Figure 4 shows the TOF signals of pre-charged clusters with various extraction delays from 300 μ s to 460 μ s with respect to the ablation laser irradiation at the cluster source. This is corresponding to comparison of the mass distributions of pre-charged clusters among various parts of the cluster beam bunch supplied from the cluster source. The result shows that the amount of pre-charged ions is relatively high around 300 μ s and 420 μ s after the laser ablation.

A typical waveform measured by the Channeltron detector is shown in Fig. 5 (dashed curve). A flux waveform of Al atoms, which was reconstructed from the yields of Al atoms in the TOFMS signals is also

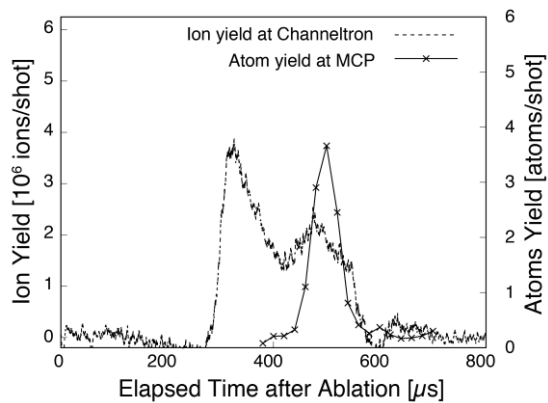


Fig. 5. An ion flux waveform observed by the Channeltron detector and a flux waveform of aluminum atoms reconstructed from TOFMS signals.

shown in the figure (solid curve). From the reconstructed waveform, we found that the neutral Al atom reached the acceleration gap around 450 μs to 550 μs after the laser ablation at the cluster source. From these results, the ion bunch is considered to be roughly divided into two components having different drift velocities. The faster component contains more monoatomic ions and pre-charged cluster ions, while the slower one contains more neutral atoms and neutral clusters.

4. Concluding Remarks

In this study, we successfully obtained the mass distribution of pre-charged clusters supplied from the laser-ablation cluster source by using the TOFMS system combined with the pulsed ion extractor. From the results of mass spectrometry with various extraction delays, we also found that the cluster beam bunch consists of two components having different drift velocities and different kinds of cluster particles.

In this paper, the operating conditions of the cluster source such as background gas pressure, laser fluence, ablation laser irradiation timing, and nozzle shape, were fixed. It is interesting to investigate how these operating conditions affect the flux waveform and yields of pre-charged clusters. We plan to conduct the experiments to investigate these dependencies in the future.

References

- [1] I. Yamada, *et al.*, “Materials processing by gas cluster ion beams”, *Mat. Sci. Eng. R*, **34**, pp.231–295 (2001).
- [2] A. Brunelle, *et al.*, “Enhanced secondary-ion emission under gold-cluster bombardment with energies from keV to MeV per atom”, *Phys. Rev. A*, **63**, 2, 022902 (2001).
- [3] K. Narumi, *et al.*, “Energy losses of B clusters transmitted through carbon foils”, *Nucl. Instrum. Meth. B*, **135**, pp.77–81 (1998).
- [4] K. Takayama, *et al.*, “All-ion accelerators: An injector-free synchrotron”, *J. Appl. Phys.*, **101**, pp.063304 (2007).
- [5] K. Takayama *et al.*, “Racetrack-shape fixed field induction accelerator for giant cluster ions”, *Phys. Rev. Accel. Beams*, **18**, pp.050101(2015).
- [6] Y. Ishikawa, *et al.*, “Mass separated particle flux from a laser-ablation metal cluster source”, *Laser Part. Beams*, **37**, pp.324-331 (2019).
- [7] H. Tsunoyama *et al.*, “Fabrication method for nanocluster superatoms with high-power impulse magnetron sputtering”, *J. Vac. Soc. Jpn*, **60**, 9, pp.352-361 (2017).
- [8] S. Maruyama, *et al.*, “Direct injection supersonic cluster beam source for FT - ICR studies of clusters”, *Rev. Sci. Instrum.* **61**, pp.3686-3693 (1990).

Influence of Frequency on Electrostatic Potential with Space Charges Generated by Rectangular AC Corona Discharges

Kakeru UCHIMIDO*, Katsuyuki TAKAHASHI**, Koichi TAKAKI**,
Nozomi TAKEUCHI***, Shinichi YAMAGUCHI****, Hidemi NAGATA****

**Faculty of Science and Engineering, Iwate University*

***Agri-Innovation Center, Iwate University*

****Energy support Corporation*

***** Shishido Electrostatic, Ltd.*

ABSTRACT

Influence of frequency on electrostatic potential with space charges generated by rectangular AC corona discharge is investigated. A corona discharge is generated using needle to ring electrodes with high voltage rectangular AC. The ratio of positive polarity in a cycle of the rectangular wave is varied from 10% to 90%. Compressed air is supplied to an air nozzle to generate air flow from the needle electrode to an ion trapping metal plate. The average plate voltage potential is the minimum when the positive ratio is 50~60%. When the positive ratio is higher and lower than it, the average plate voltage has positive and negative values, respectively, and is the minimum at a frequency of approximately 250 Hz. The plate voltage becomes less affected by the frequency when the positive ratio approaches 50~60%. An ion distribution model in the space between the needle and plate electrode is proposed and suggests that the quasi-neutralization region in the space is produced by mixing positive and negative ions produced by corona discharge just after polarity switching. Assuming that the quasi-neutralization region is not affected by the frequency, when the polarity switching is unbalanced, the net charge is also unbalanced with increasing frequency. Therefore, the plate voltage potential is significantly affected by the frequency with unbalanced positive polarity ratio.

Keywords

Corona discharge, ionizer, potential, ion balance

1. Introduction

The corona discharge ionizer has been widely used for elimination of electrostatic charges because of its good operability [1]. The corona discharges are produced at the high voltage electrodes in the ionizer, which enable the production of positive and negative ions such as H_3O^+ , CO_3^- , NO_3^- and their cluster ions [2]. The ions produced by the corona discharges are transported by the electric field or blown air to insulators, and the charges on insulators are neutralized

by the ions. The time required for the electrostatic elimination depends on the amount of ions transported to the insulators.

For the ionizer performance, not only the short electrostatic elimination time, i.e., the large amount of ions flow to the insulators, but also the good ion balance, i.e., a low voltage potential, the balance between the amounts of ions of both polarities, is required [1]. The bad ion balance causes ESD problem on the latest electronic devices has the high sensitivity

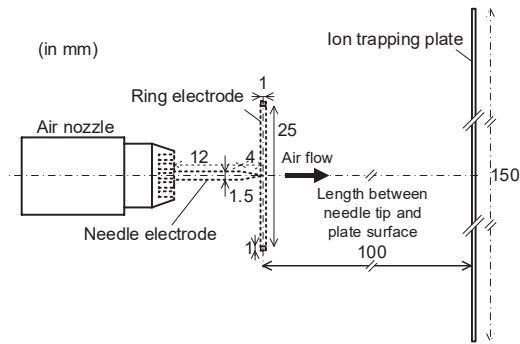


Fig. 1 Schematic of corona discharge electrode.

to ESD damage. For example, the ion balance is limited less than 25~100 V in the manufacturing process of electric devices, and only several volts in that of hard disc heads which has a very high sensitivity for ESD [3]. To control the ion balance, the distribution of ions and their behavior in the electrostatic elimination space must be clarified.

In this study, the influence of the applied voltage frequency on the ion density and the distribution of voltage potential in the space in the front of the corona discharge electrode is investigated. A corona discharge is generated using needle to ring electrode with high voltage rectangular AC. The voltage potential is measured using an ion measuring system utilized by a high voltage operation amplifier with a high input impedance.

2. Experimental Setup

Fig. 1 shows the schematic diagram of the corona discharge electrode. The corona discharge electrode consisted of a tungsten needle (16 mm in length, 0.75 mm in diameter, 20 degree in taper angle of 0.075 mm in curvature radius) and a stainless-steel ring (12.3 mm in inner diameter and 13 mm in outer diameter). The tip of needle electrode is placed in the center of the ring electrode. A compressed air nozzle (Ikeuchi, 1/4MTF-R8-010PP-IN) is placed behind the needle electrode to transport ions, generated by the corona discharges at the needle tip, toward to an ion trapping plate

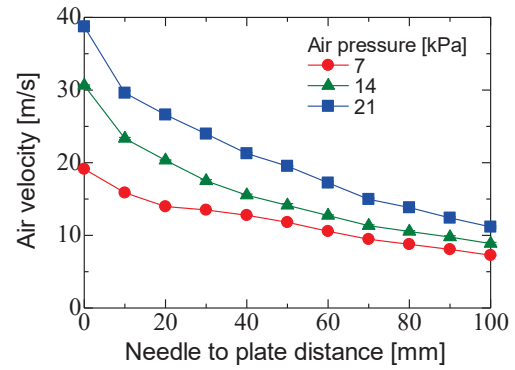


Fig. 2 Distribution of air velocity between corona and plate electrodes.

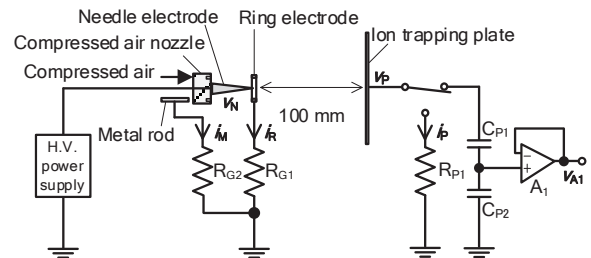


Fig. 3 Schematic of ion measuring system.

(Stainless-steel, $150 \times 150 \text{ mm}^2$ area) placed in front of the electrodes with a needle to plate distance of 100 mm. The compressed air is supplied to the nozzle using an air compressor (Hitachi, 0.75LE-8SB) with an air pressure of 7-21 kPa. Fig. 2 shows the air velocity toward to the plate as a function of the distance from the needle to the plate for three air pressures, measured using an air velocity meter (Testo, 512-2).

Fig. 3 shows the schematic diagram of the evaluation system for neutralization of electrostatic charges by corona discharges [4]. A rectangular AC voltage is generated using a high voltage power supply (Trek, Model 20/20C-HS) controlled by a function generator (nF, WF1947), and is applied to the needle electrode. Fig. 4 shows a typical waveform of the applied voltage. The positive ratio (PR) is defined as the ratio of positive phase in one cycle, and is calculated by following equation,

$$PR = t_{POS} / t_{CYCLE} \times 100\% \quad (1)$$

where, t_{POS} is time of positive phase and t_{CYCLE} is time of one cycle. PR varies from 10% to 90%. The voltage

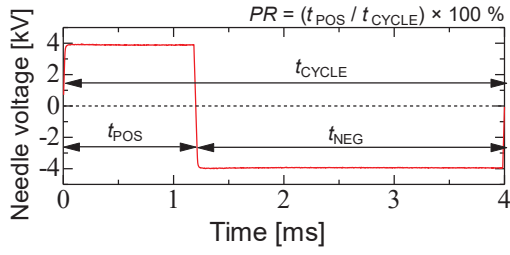
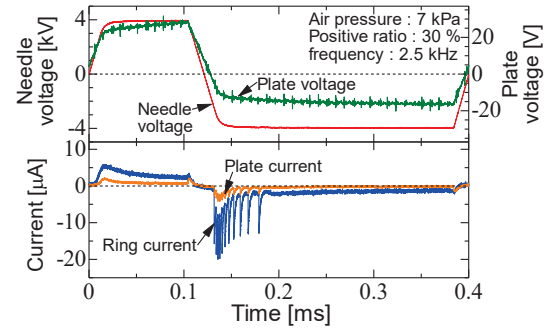


Fig. 4 Waveforms of applied voltage to needle.

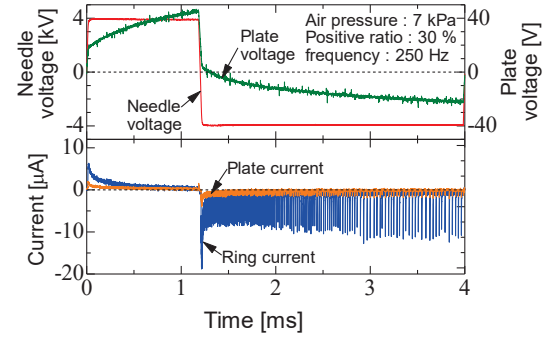
amplitude is ± 4 kV, and the frequency ranges from 10 Hz to 5 kHz. The voltage slew rate is 0.35×10^6 V/s and is not affected by experimental conditions. A current flow in the ring electrode (i_R) is measured by measuring the voltage drop across a $100 \text{ k}\Omega$ resistor connected between the ring electrode and grounded terminal. To eliminate a displacement current induced by the applied voltage to the needle electrode, a brass rod (100 mm length) connected to the grounded terminal via a $100 \text{ k}\Omega$ resistor is placed near the high voltage power supply. The displacement current flow in the brass rod (i_M) is measured by measuring the voltage drop across the resistor, and the discharge current flows in the ring electrode is estimated by subtracting i_R from i_M . As the same manner, a current flow in the ion trapping plate (i_P) is measured by the voltage drop across the $100 \text{ k}\Omega$ resistor connected to the plate, and the ion current flow into the plate is estimated by subtracting i_M .

The voltage potential on the ion trapping plate (v_P) is measured using a buffer circuit consisted of a high voltage operational amplifier (Texas Instruments, OPA454), capacitors C_{P1} consisted of 3 capacitors (WIMA, FKP2-33/1000/10) connected in series, which has a total capacitance of 11 pF , and C_{P2} (KEMETPHE448SB4100JR06, 1 nF). v_P is divided by C_{P1} and C_{P2} . The ratio between the output voltage of the operational amplifier (v_{A1}) and v_P is 85:1. The capacitance of the plate including a stray capacitance is 21.8 pF .

To estimate the amount of charge flow in the plate, charge neutralization time of the ion trapping plate which is charged to $\pm 1.1 \text{ kV}$ using a high voltage DC



(a) 2.5 kHz



(b) 250 Hz

Fig. 5 Waveforms of needle and plate voltages and ring and plate currents

power supply (Shishido electrostatic, Statiller 35S) is evaluated. Charge neutralization time is defined as time required for decreasing the plate voltage from $\pm 1 \text{ kV}$ to $\pm 100 \text{ V}$. The PR is adjusted so that the time averaged voltage potential on the plate after charge neutralization is 0 V .

3. Results and Discussion

Fig. 5 shows waveforms of needle and plate voltages, ring and plate currents after rejecting displacement current for a frequency of (a) 2.5 kHz and (b) 250 Hz. PR is 30% and air pressure is 7 kPa. The plate voltage increases to same polarity with the needle voltage by charging current flow to the plate. Phases of the discharge current in the ring electrode and ion current flows in the plate electrode are synchronized. From the discharge current waveform, the positive glow corona in positive phase and Trichel-pulse corona in negative phase are observed. The current value just after phase switching is high and then decays during

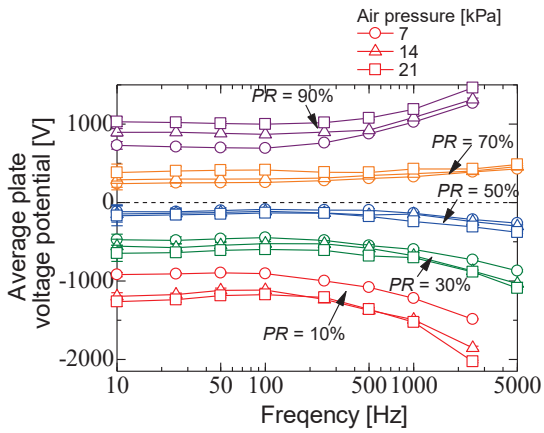


Fig. 6 Average plate voltage potential as a function of frequency for various positive ratios and air pressures.

approximately 0.5 ms. The frequency of Trichel-pulses decreases with time and has a constant value approximately 3 ms after phase switching. Air ions generated by the corona discharge are driven by an electrostatic force according to the electric field, and a blown air from the air nozzle. Just after phase switching, the electric field at the needle tip is enhanced by a space charge potential produced in the previous phase, which increases the discharge current.

Fig. 6 shows time-averaged plate voltage potential as a function of frequency with various PR and air pressures. The plate voltage potential increases to positive with PR ranged from 70% to 90% and increases to negative with that from 10% to 50%, with increasing the frequency. The increment of the plate voltage potential is the minimal at 50~60%, and increases with increasing and decreasing PR . The absolute value of the voltage potential increases with increasing air pressure.

Fig. 7 shows typical waveforms of plate voltage when the ion trapping plate is charged to + 1.1 kV. The plate voltage fluctuates with phase switching of applied voltage, and decays exponentially because air ions produced by corona discharges move toward to the ion trapping plate. Fig. 8 shows charge neutralization time as a function of frequency for three gas pressures when the plate is charged to (a) positive and (b) negative. PR

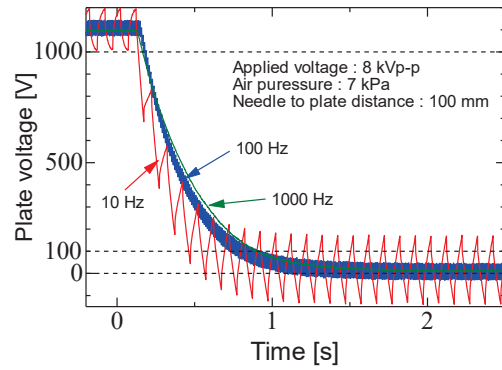


Fig. 7 Typical waveforms of plate voltage for measurement of charge neutralization time.

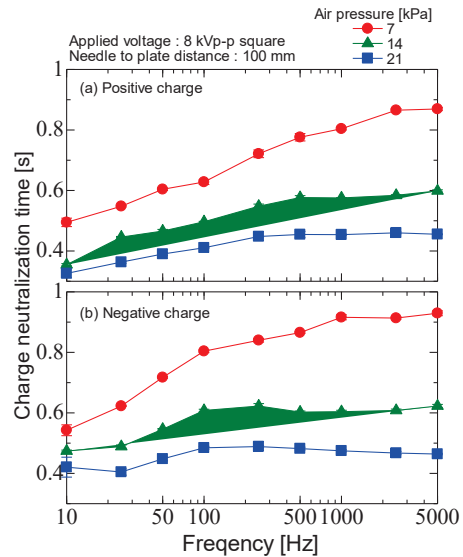


Fig. 8 Charge neutralization time as a function of frequency for various air pressures.

is adjusted so that the time averaged plate voltage potential after neutralization and ranges from 50% to 60%. The charge neutralization time increases, i.e., the current flows to the plate decreases, with increasing frequency. This increment decreases with increasing air pressure. Fig. 9 shows the average ring current for positive or negative half cycle and average current for one cycle as a function of frequency. The current for half cycle increases with increasing frequency, which is the contradictory with the result shown in Fig.8.

The polarity of ions produced by the corona discharges and transported to the front of the needle tip is synchronized to the applied voltage phase. The slew

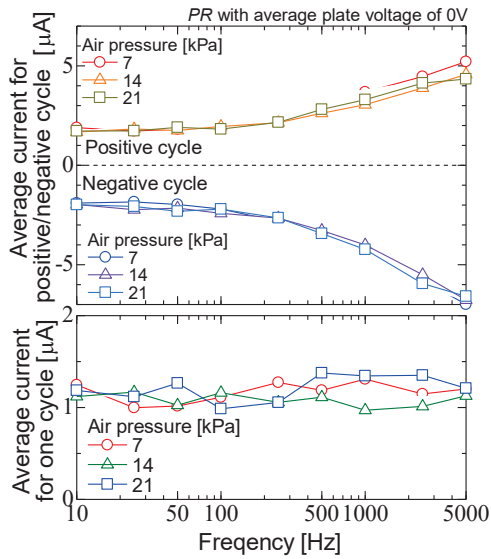


Fig. 9 Average currents for positive or negative half cycle and for one cycle as function of frequency for various air pressures.

rate of the applied voltage is sufficient high, the ions which have an opposite polarity are remained near the needle tip, which affects the corona discharge just after phase switching until approximately $0.5 \mu\text{s}$ in positive phase and $3 \mu\text{s}$ in negative phase as shown in Fig. 5. Because the drift velocity is higher than the air velocity at the vicinity of the needle tip, the ions which have an opposite polarity to the applied voltage can be dragged back to the needle electrode. Thus, ions with both polarities are mixed and a quasi-neutralized region is formed. The quasi-neutralized region does not contribute to the current flow to the plate. Furthermore, in this region, the ions are lost by recombination reactions. The ion density in the ionization region of corona discharge is in order of $10^{16-17} \text{ m}^{-3}$, and the recombination coefficient is approximately $1.6 \times 10^{12} \text{ m}^3/\text{s}$, so that a lifetime of ions is in order of 10^{5-4} s , which decrease the ions density in the space. The percentage of the total quasi-neutralized region in the space in the electrode system increases with increasing frequency. Therefore, the charge neutralization time increase with increasing frequency. The increment of air velocity by increasing the air pressure contribute to

decreasing the ion recombination reactions.

In the space in the electrode system, the positive and negative regions are defined as the space occupied by positive and negative ions, respectively. Assuming that the ion velocity and ion density just after phase switching are not affected by the frequency, the extent of quasi-neutralized region is not also affected by the frequency. When PR is lower or higher than 50%, the percentage of the total quasi-neutralized region in the space in the electrode system increases with increasing frequency. When the frequency is sufficient high, only positive or negative region apparently exists, which leads the unbalanced net charges. Therefore, the time-averaged ion trapping plate voltage increases to positive or negative with increasing frequency as shown in Fig.6.

4. Conclusions

The influences of the frequency and the positive phase ratio in a cycle on the voltage potential of the ion trapping pate placed in the front of corona electrodes. When the frequency is higher than 250 Hz and the positive phase ratio is lower or higher than 50~60%, the voltage potential increase to positive or negative with increasing frequency. The charge neutralization time increases with increasing the frequency because the quasi-neutralized region formed by mixing both-polarities ions is extended and loss reactions increase. The extension of the quasi-neutralized region leads the apparent omnipresence of an ion polarity in the space between the electrode system and the increase in the ion trapping plate voltage potential.

Acknowledgments

A portion of work this work was supported by a Grant-in-Aid for Scientific Research (S) from the Japan Society for the Promotion of Science (grant number 19H05611).

References

- [1] K. Takahashi *et al.*, “Development of a Corona

Discharge Ionizer Utilizing High-Voltage AC Power Supply Driven by PWM Inverter for Highly Efficient Electrostatic Elimination”, *IntechOpen Ltd., London* (2019)

- [2] K. Nagato *et al.*, “An analysis of the evolution of negative ions produced by a corona ionizer in air”, *Int. J. Mass Spectrom.* **248**, pp. 142–147 (2006)
- [3] Y. Mizoh *et al.*, “Soft ESD phenomena in GMR heads in the HDDmanufacturing process”, *J. Electrostat.*, 64, pp. 72-70 (2006)
- [4] K. Takahashi *et al.*, “Development of an ion measuring system for AC corona discharge”, *IEEJ Trans. Fund. Mater.*, **138**, 11, pp.551-552 (2018)

Comparison of Plasma Characteristics of High-Power Pulsed Sputtering (HPPS) Glow Discharge and Hollow-Cathode Discharge

Shoki Abe, Katsuyuki Takahashi*, Seiji Mukaigawa, Koichi Takaki*, and Ken Yukimura

Iwate University, Japan

** Agri-innovation Center, Iwate University, Japan*

ABSTRACT

A high-power pulsed sputtering (HPPS) discharge source was evaluated experimentally as the ion sources for droplet-free plasma processes. The basic principle of the HPPS is a hollow cathode arrangement of two targets on the same potential facing each other. The magnetic field is also used to reduce electron losses through the electron trapping in the gap between the targets. In the HPPS discharge source, two opposing targets consisting of a rectangular plate target made of titanium (Ti) with a length of 60 mm, a height of 20 mm and a thickness of 5 mm was used, and the gap length was set to be 10 mm. A rectangular pulse voltage with amplitude ranged from -330 to -1,200 V and pulse width of 600 μ s was applied to the target. Six permanent magnets were used to confine the charged particles and were located behind the targets. The magnetic field at the gap between the target was 0.2 T and was parallel to electric field in the ion sheath. The charged particles of the glow discharge plasma were successfully confined between the target plates by setting the magnets. The current density on the target with the magnets (HPPS) was about 15 kA/m² and was one order higher than that without the magnets (hollow-cathode discharge). The ion density of HPPS discharge was approximately 3.4×10^{18} m⁻³ at 30 mm apart from the electrode edge and decreased to 2.2×10^{17} m⁻³ by changing from the HPPS to the hollow-cathode discharges.

Keywords

HiPIMS, HPPS, HCD, Glow Discharge, Sputtering

1. Introduction

Surface modification of a material by a metal film or a ceramic film is an important process for various applications of the material.[1,2] High-power impulse magnetron sputtering (HiPIMS) is one of the promising methods of droplet-free surface deposition because of its high power density and high ionization rate of sputtered metals.[3] However, its low target utilization efficiency and large size, limits installation in a practical use. A high-power pulsed sputtering (HPPS) discharge generated by parallel electric and magnetic fields at the ionization region was developed to overcome some disadvantage of HiPIMS.[4] In this paper, the influence of magnetic field on the electrical

characteristics of the HPPS discharge (with magnets) is investigated and are compared with those of the hollow cathode discharge (without magnets).

2. Experimental Setup

Figure 1 shows a schematic diagram of the HPPS discharge ion source. The HPPS discharge unit is compact in size ($60 \times 67 \times 86$ mm³). A pair of rectangular Ti plates with a length of 60 mm, a height of 20 mm and a thickness of 5 mm was used as the sputtering target cathode. Two Ti target plates were placed on the opposite side with a gap length of 10 mm and set the permanent samarium-cobalt magnets (540 mT) in the magnet holders behind the targets. A

magnetic field was produced perpendicular to the targets. The strength of the magnetic field in the gap was approximately 0.2 T.

A cylindrical vacuum chamber was evacuated to 5×10^{-3} Pa and the argon gas was fed into the chamber with the gas pressure of 9.5 Pa. A rectangular pulsed voltage with a pulse width of 600 μ s and amplitude of -1000 V was applied to the target cathode using a high-voltage negative pulse power supply (PEKURUS KJ06-3265; -3 kV, 100 A, 1 kHz, 1 ms). The repetition rate was fixed at 50 Hz. A 20 Ω resistor was connected in series to the cathode. To extract ions from plasma, a stainless steel (SUS304) disk electrode with a diameter of 3.85 cm (Surface area; $A = 11.6$ cm²) was placed in the chamber at a distance L away from the HPPS discharge ion source. L was varied from 30 to 90 mm. A negative DC voltage of -80 V was applied to the disk electrode using a power supply (PEKURUS; PEK6-0001-06). The target voltage V_T [V], the voltage applied to HPPS discharge ion source and the disk electrode voltage V_D were measured by a high-voltage probe (Tektronix P-5100; 2.5 kV, 500 MHz). The current flowing into the target cathode I_T [A] and the disk electrode I_D [A] were observed by current transformers (Pearson 110A). The waveforms of the voltage and current were monitored with a digital oscilloscope (Tektronix TDS 3014B). The integrated OES during the plasma generation are measured using a spectrometer (Blue-WAVE model UVN-25, StellarNet, 600 Gr mm⁻¹ grating). The observation point was focused on the gap center using a condenser lens with a focal length of 400 mm. The exposure time was 100 ms. When a Bohm sheath criterion and a quasi-static Child-Langmuir current are assumed, the behavior of the ion sheath d and the density n_i can be estimated from the following by calculating the holder current density j from the measured holder current I_D . When ions with a density n_i move with a Bohm velocity u_B , the ion current is expressed based on the continuity as follows

$$n_i = j / 0.61eu_B \quad (1)$$

where e is an elementary charge. The ion sheath thickness d is expressed according to the Child-Langmuir law

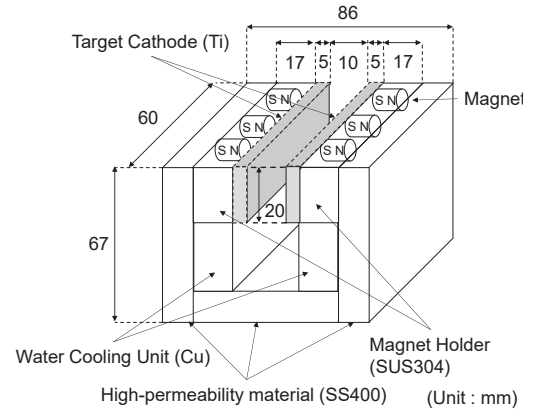


Fig. 1 the HPPS discharge ion source

$$d^2 = \frac{4\epsilon_0}{9} \left(\frac{2e}{m} \right)^{\frac{1}{2}} \frac{V_D^{\frac{3}{2}}}{j} \quad (2)$$

where ϵ_0 is the dielectric constant in vacuum, m is the ion mass, and V_D is the applied voltage of the disk electrode.[5]

3. Results and Discussion

3.1 Electrical Characteristics

Figure 2 shows the waveforms of voltage applied to the target and plasma current with and without magnets. The current density on the target with the magnets (HPPS discharge) was approximately 15 kA/m² and was one order of magnitude higher than that without the magnets (hollow-cathode discharge; HCD). The consumed power of the HPPS discharge is 12 kW (=1.0 kW/cm²), while those of the HCD is 0.6 kW. The rise time of the plasma current has a delay of 100 μ s in the HCD, whereas there is almost no delay time in the HPPS discharge. In the HPPS discharges, the magnetic field perpendicular to the target surface contributes to the increase in the travel distance of the electron through the gyration motion by the Lorentz force. As a result, plasma is effectively produced by increasing the electron collision frequency. On the other hand, in the HCD, the electrons are only accelerated by the electric field, so the number of collisions is smaller than that in the HPPS discharge. As a result, the delay time of the discharge ignition from the applied voltage increases by removing the magnets. The glow discharge plasma is confined

between the rectangular target plates by setting the magnets behind the target plates.

3.2 Optical Characteristics

Figure 3 shows the emission spectra of HCD (a; without magnets) and the HPPS discharge (b; with magnets) plasmas at an applied voltage of -1000 V. The intensity of the spectrum from the HPPS discharge plasma is approximately one order larger than that from the HCD plasma. Both spectra include light emissions from sputtered Ti species [neutral excitation states (Ti I), and ions (Ti II)] and Ar gas particles [neutral excitation states (Ar I) and ions (Ar II)]. In the case of the HPPS discharge, a singly ionization emission of Ti is remarkably observed at wavelengths of 323.45 and 344.94 nm. These intensities are larger than those of Ar ions at a wavelength of 454.51 nm and the excited state of Ti at a wavelength of 519.40 nm. On the other hand, in the HCD, the emission intensities of singly ionized Ti are less than those of Ar ions and the excited state of Ti. Thus, it is confirmed that Ti is sputtered and actively ionized in the HPPS discharge plasma. Also, in the HCD, the intensity of the excited state of Ar at a wavelength of 750.4 nm is higher than that of the HPPS plasma. In the HPPS discharge, electrons are trapped in the gap by the Lorentz force because of the movement in the vertical direction of the magnetic field. As the diffusion loss of electrons decreases, the electron collision rate increases in the plasma. The input energy of the HPPS is approximately one order higher than that of the HCD. The ratio of transition from excitation (Ar I) to ionized states (Ar II) by electron collision and the electron collisional excitation (Ar I) increases with increasing input power.[6] Therefore, in the HPPS, the intensity of the excited state of Ar decreases and the intensity of singly ionized Ar increases in comparison to HCD.

3.2 Ion Densities

Figure 4 shows the calculated ion density and ion sheath thickness as a function of the holder electrode position L for (a) the HCD (without magnets) and (b) the HPPS discharge (with magnets) plasmas. In the calculation, the holder current at $580 \mu\text{s}$ after applying

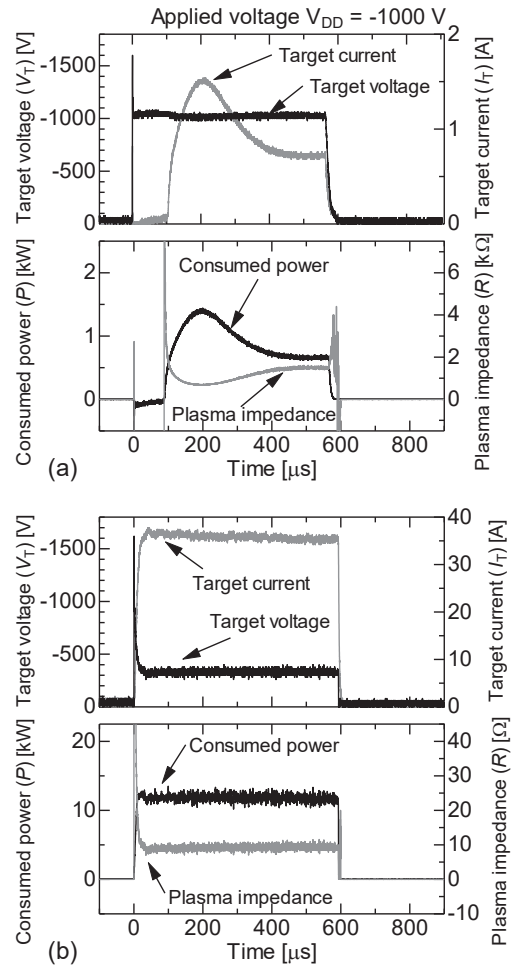


Fig. 2 Waveforms of voltage applied to the target and plasma current with and without magnets.

a voltage is used as the ion saturation current I_D . The ion saturation current density j is obtained by I_D/A , ($A = 11.6 \text{ cm}^2$; surface area of the disk electrode). When the electron temperature is assumed to be 1 eV, the Bohm velocity u_B is calculated to be 1500 m/s. Both ion densities decrease with the holder position L . The ion sheath thickness gradually increases with the holder position L . The ion density of the HPPS discharge plasma is almost one order higher than that of the HCD plasma. The ion densities at 30 mm of the holder position are 3.4×10^{18} and $2.2 \times 10^{17} \text{ m}^{-3}$ for the HPPS discharge and the HCD, respectively. The ion density of the HPPS discharge plasma decreases to $1.4 \times 10^{17} \text{ m}^{-3}$ with increasing the holder position L from 30 to 90 mm. These values and the trend are

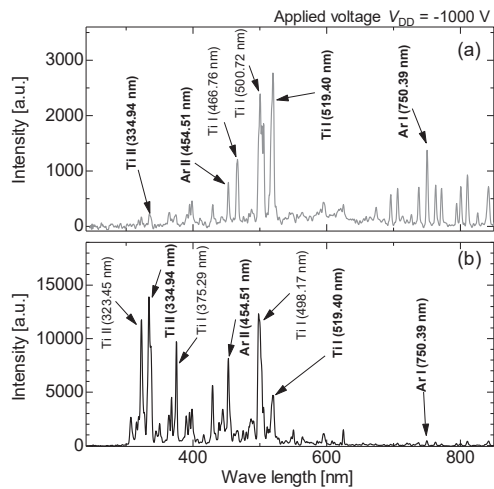


Fig. 3 Emission spectra of HCD (a; without magnets) and the HPPS discharge (b; with magnets) plasmas.

almost consistent with the result of the double-probe measurement reported by Azuma.[7] The ion density distribution in the diffusion region is different between the HCD and the HPPS discharge. In the HCD, ion density decreases linearly with increasing holder position L . In the HPPS discharge, it decreases exponentially.

4. Conclusions

The electric characteristics of a glow discharge plasma with six permanent magnets behind the hollow cathode targets (HPPS discharge) are obtained in comparison to those without magnets (HCD). The target current density of the plasma of the HPPS discharge is approximately 15 kA/m^2 and is one order higher than that of the HCD. Additionally, the rise time of the plasma current has a delay of $100 \mu\text{s}$ in the HCD, whereas there is almost no delay time in the HPPS discharge. The consumed power and the plasma impedance of the HPPS discharge plasma are 12 kW ($=1.0 \text{ kW/cm}^2$) and 9.0Ω , respectively, while those of the HCD are 0.6 kW and $1.5 \text{ k}\Omega$, respectively. The glow discharge plasma is confined between the rectangular target plates by setting the magnets behind the target plates. The light emissions from the singly ionized ions of Ti and Ar and the excited state of Ti are confirmed in the HPPS discharge plasma. The Ar II intensity of the HPPS discharge plasma increases

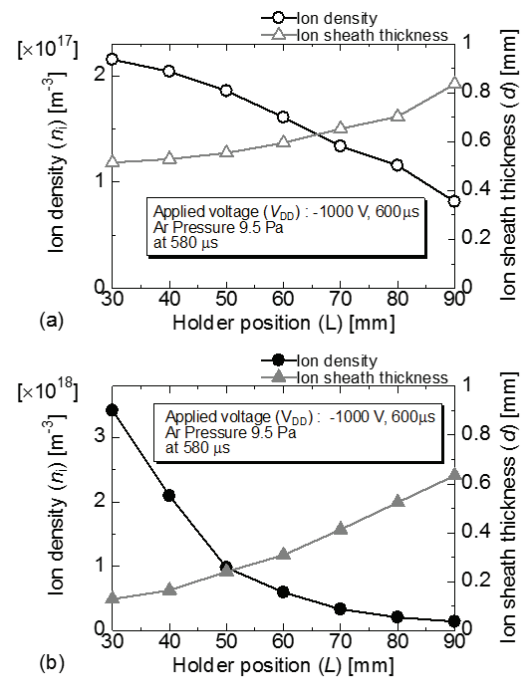


Fig. 4 ion density and ion sheath thickness as a function of the holder electrode position L for (a) the HCD (without magnets) and (b) the HPPS discharge (with magnets) plasmas.

exponentially with the Ar I intensity and is much larger than that of the HCD plasma. The emission threshold of Ti II (334.94 nm) in the HPPS discharge plasma is approximately 1 J (i.e. 0.14 kW/cm^2 power density on the target). The high-power consumption is a key factor for increasing the metallic ion density in the plasma. The ion density of the HPPS discharge plasma is approximately $3.4 \times 10^{18} \text{ m}^{-3}$ at 30 mm apart from the electrode and decreases to $2.2 \times 10^{17} \text{ m}^{-3}$ by changing the ion source from the HPPS discharge to the HCD. Both gas and sputtered metal particles are significantly ionized in the HPPS discharge mode compared with the HCD mode.

References

- [1] U. Helmersson "Ionized Physical Vapor Deposition (IPVD): A Review of Technology and Applications" *Thin Solid Films.*, **513**, 1-2, 1-24 (2006)

- [2] N. Huang “Surface modification of biomaterials by plasma immersion ion implantation” *Surface & Coatings Technology*, **186** 218–226 (2004)
- [3] A. Anders, “High power impulse magnetron sputtering: Current-voltage-time characteristics indicate the onset of sustained self-sputtering” *J. Appl. Phys.*, **102**, 113303, (2007)
- [4] K. Yukimura, “Electrical characteristics of arc-free high-power pulsed sputtering glow plasma” *Phys. Stat. Sol. (A)*, **205**, 5246-5250 (2008)
- [5] N. S. J. Braithwaite, “Introduction to gas discharges” *Plasma Sources Sci. Technol.*, **9**, 517 (2000).
- [6] Y. Saito “Global model analysis of Ar inductively coupled plasma driven by a 150 kHz-band high-power pulse burst” *J. Appl. Phys.*, **58**, SAAB06 (2019)
- [7] K. Azuma “Electrical and Optical Characteristics of High-Power Pulsed Sputtering Glow Discharge” , *IEEE Trans. Plasma Sci.* **44**, 3201 (2016).

Evaluation of Electron Beam Characteristics using a Virtual Cathode Oscillator

Michihiro Ohta, Kentaro Inui, Kazuki Nagao, Taichi Sugai, Weihua Jiang

*Extreme Energy-Density Research Institute,
Nagaoka University of Technology*

ABSTRACT

The principle of forming a virtual cathode and oscillating microwaves using a high-power pulse power generator, ETIGO-IV, has been theoretically elucidated. However, the principle has only been clarified theoretically. In this study, we experimentally clarified whether the virtual cathode is actually formed, using two detectors which were made and calibrated by ourselves. In the experiment where both detectors were put in at the same time and the distance between the large detector and the anode was varied, the formation of a virtual cathode was confirmed, although a steep current decrease and a long pulse problem occurred.

Keywords

Pulse power, Virtual Cathode Oscillator, ETIGO-IV, Electron beam

1. Introduction

Microwaves are electromagnetic waves with frequencies from 1 to 30 GHz, and high-power microwaves (HPM), which have a power of more than 100 MW, are expected to be applied to fields such as accelerators and wireless power transmission. There are various types of HPM sources such as Klystron and Magnetron, and Virtual Cathode Oscillator (Vircator) is one of them. Compared to other generators, the Vircator has the following advantages: no external magnetic field is required, the structure is simple, the frequency can be adjusted, and several MW to several GW can be generated. On the other hand, they also have the disadvantages of low conversion efficiency of only a few tens of percent at best and many unknowns in the oscillation mechanism [1]. This study aims to quantitatively clarify the oscillation mechanism of the Vircator by constructing an instrument to measure the electron beam current, and to experimentally clarify the virtual cathode formation.

2. Experimental Setup

Figure 1, 2 and Figure 3, 4 show the appearance and equivalent circuit of a detector (small) and a detector (large) for electron beam current measurement. One detector (small) is an anode plate connected to shunt resistors consisting of eighty 10 Ω resistor in parallel. This detector (small) measures the electron beam as it hits the anode. The other detector (large) has a 24 cm diameter electron beam collector at its tip. The collector is fixed with four screw pipes (parasitic inductance 127.8 nH), and the position of the collector can be changed by changing the length of the screw pipes. At the base, there are 150 parallel shunt resistors (metal film resistors, 10 Ω) in concentric circles. Thus, the electron beam current can be measured from the potential of the shunt resistors.

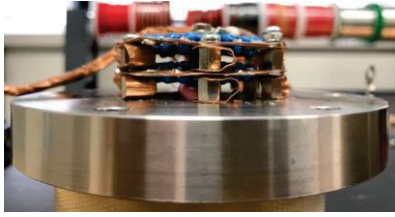


Fig.1 External view of detector (small)

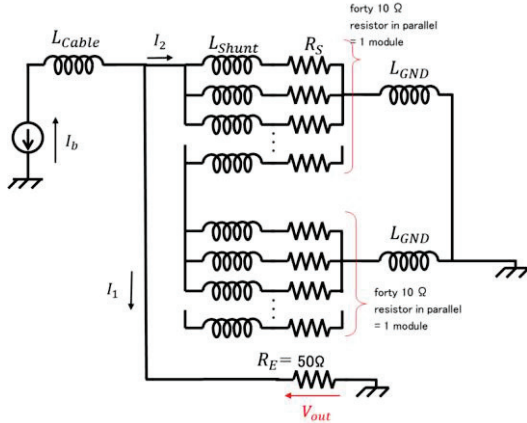


Fig.2 Equivalent circuit of detector (small)

3. Calibration Experiment

3.1 Calibration Experimental Setup

In this study, a virtual cathode oscillator is operated using a high repetition rate pulse power generator "ETIGO-IV" which shows Figure 5. The voltage rating is 400 kV, the current rating is 13 kA, the pulse width is 120 ns, and the repetition rate is 1 Hz [2]. Figures 6 and 7 show the schematic diagram of the virtual cathode oscillator, the detector (small) and the detector (large) installed at the output end of the ETIGO-IV in the calibration experiment. The cathode is a 12 cm diameter stainless steel disk gluing 10 cm diameter velvet.

In the calibration experiment of the detector (small), a copper plate with a thickness of 1 mm was used as the anode to check if all the electron beams can be measured correctly. In the calibration experiment of the detector (large), the anode is made of 12 μ m thick aluminum foil to check if all the transmitted electron beams can be measured correctly.

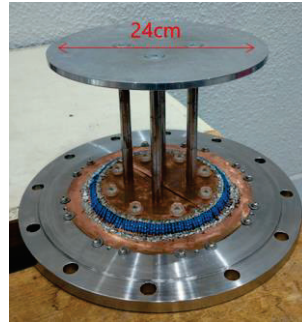


Fig.3 External view of detector (large)

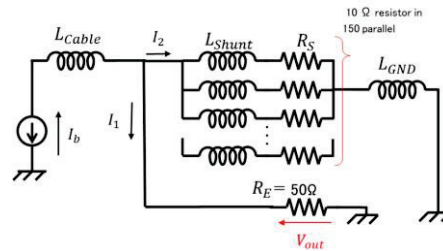


Fig.4 Equivalent circuit of detector (large)



Fig.5 Repetitive pulsed power generator "ETIGO-IV"

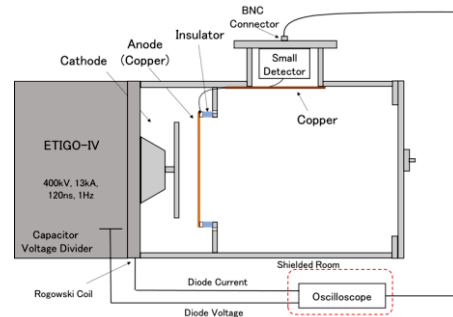


Fig.6 Schematic diagram of detector (small)

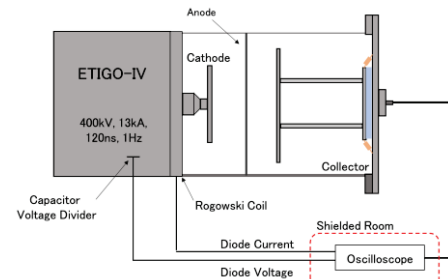


Fig.7 Schematic diagram of detector (large)

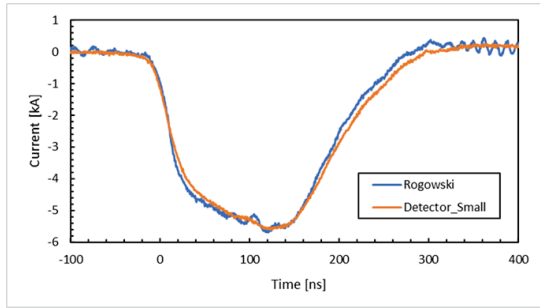


Fig.8 Waveform of Rogowski coil and detector (small)

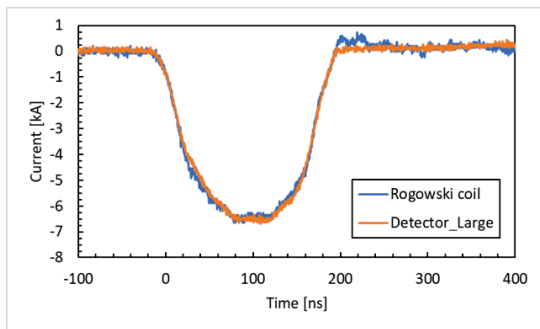


Fig.9 Waveform of Rogowski coil and detector (large)

3.2 Results of calibration experiments

Figure 8 and 9 show the experimental results. The results of the small and large detectors are in general agreement with those of the Rogowski coil. Therefore, the two detectors accurately measure the electron beam.

4. Experiment using two detectors

4.1 Experimental Setup

Figures 10 show the schematic diagram of the virtual cathode oscillator, the detector (small) and the detector (large) installed at the output end of the ETIGO-IV in the experiment. The anode is made of a stainless-steel mesh (transmittance: 65.8 %) cut out in a circular shape and fixed with a ring-shaped fixture. The anode-cathode gap is 22 mm. The voltage and the current upstream of the cathode are measured using the capacitance divider and Rogowski coil of the ETIGO-IV respectively, and the electron beam is measured using the detectors. Each signal is observed on an oscilloscope through a coaxial cable. The detector (large) is moved to increase the distance between the anode and the

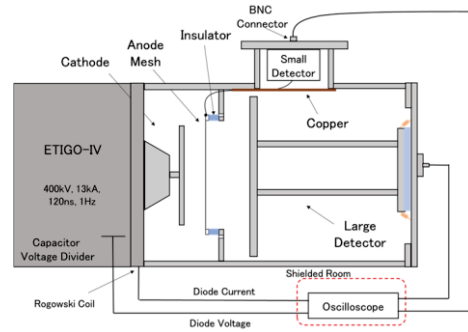


Fig.10 Schematic diagram of two detector

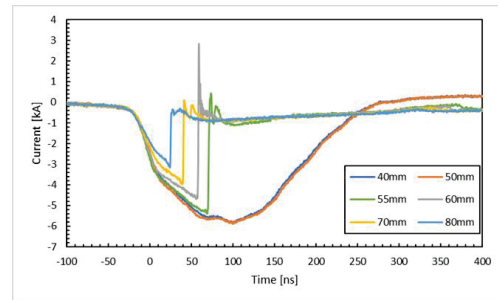


Fig.11 Results of all transmitted electrons measured by the detector (large)

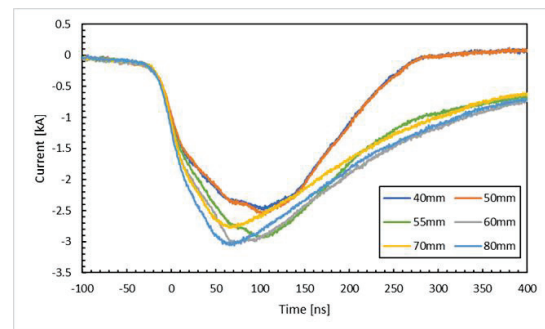


Fig.12 Measurement results of incident/reflected electrons by detector (small)

detector (large).

4.2 Characteristics of basic IECF setup

Figures 11 and 12 show the results when the distance between the anode and the detector (large) was changed to 40 mm, 50 mm, 55 mm, 60 mm, 70 mm, and 80 mm. It can be seen that the current of the detector (large) decreases drastically after the distance of 55 mm. This is due to the fact that the virtual cathode is formed before electrons arrive at the detector. In the results for the detector (small), the current increased after 55 mm as well, although it is not significant increase. In addition, there was a delay in the fall of the current after 55 mm.

5. Conclusions

In this study, two types of detectors were made to analyze the behavior of electron beams in a virtual cathode oscillator. The two types of detectors were calibrated to measure the electron beam accurately. In an experiment where the distance between the anode and the detector (large) was increased, the current in the detector (large) decreased rapidly, suggesting the formation of a virtual cathode. In the case of the detector (small), no significant increase in current was observed, and a long pulse was observed on the falling edge of the current.

Future experiments will be conducted to improve the frequency response of the detector (small).

References

- [1] W.Jiang, "Time-Frequency Analysis of Virtual-Cathode Oscillator", IEEE Trans. Plasma Science, Vol.38, No. 6 1325-1328 (2010).
- [2] A.Tokuchi, N.Ninomiya, W.Jiang, K.Yatsui, "Repetitive Pulsed-Power Generator "ETIGO-IV", IEEE Trans. Plasma Science, Vol 30, No. 5, 1637-1641(2002).

Electron Beam Shape Dependence of Output Microwave Characteristics in Reflex Triode Virtual Cathode Oscillator

R. Tanaka, Y. Fukada, and H. Ito

University of Toyama, Gofuku 3190, Toyama Toyama 930-8555, Japan

ABSTRACT

A virtual cathode oscillator, which can generate a high-power microwave, has been widely studied over the last four decades. In this paper, we present the electrode shape and material dependence of microwaves and electron beams generated in a reflex triode vircator. The experiments were conducted for aluminum and velvet cathodes and for two types of electrode shapes: (1) circular shape with a diameter of 46 mm and (2) elliptic shape with an aspect ratio of 2:3 and the same emitting area as the circular electrode. In addition, an X-ray pinhole camera with a beryllium window was used to evaluate the cross-sectional shape of the electron beam. These results show that the electrode shape is one of the important key parameters for designing the virtual cathode oscillator with a high-power performance.

Keywords

Virtual Cathode Oscillator, High-power pulsed microwave source, Pulsed power technology, High-intensity pulsed electron beam

1. Introduction

A high-power microwave (HPM) is expected to be applied in various fields such as power transmission technology in the space-based solar power concept, plasma heating of fuel in nuclear fusion, and high-power radar for industrial field [1,2]. Vircator is one of the promising sources that can generate the HPM by utilizing a high-current relativistic electron beam. The advantages of the vircator are its high-power capability, frequency tunability, and simple structure [2,3]. The vircator has some drawbacks in terms of low power conversion efficiency and wide frequency bandwidth. To overcome these disadvantages, experimental and theoretical research on efficiency improvement and oscillation frequency control has been conducted [4-6].

A typical vircator consists of an electron beam diode and a drift tube. Electrons are emitted from a cathode and accelerated toward a semitransparent anode by applying a negative high voltage pulse to the cathode. When the electron beam passing through the anode exceeds the space charge limiting current, a virtual cathode with the same potential as the cathode is formed behind the anode. The microwave is generated

both when the electrons oscillate back and forth between the cathode and the virtual cathode and when the virtual cathode oscillates in time and space. These two mechanisms occur at different frequencies and give rise to the high-power microwave. The reflex triode (RT) has received much attention due to its compact size and high peak power capability [7]. Recent research on the RT vircator has focused on the power conversion efficiency and the frequency stability for various electrode materials, anode-cathode gaps, and applied voltages. In the coaxial cylindrical type, it has been reported that the generated electron beam forms a virtual cavity and microwave cavity resonance occurs [8]. These experiments were carried out using symmetrical circular electrodes.

On the basis of abovementioned knowledge that extensive studies in the relevant fields have accumulated so far, we have initiated work on the RT vircator based on the assumption that the shape of electrodes has a potential to affect the cross-sectional area of the electron beam through the mechanism of beam-microwave interaction in vircator.

In this paper, effects of an elliptic electrode on HPM

performance in the RT vircator are studied. Specifically, the electrode shape dependence of the peak microwave power and the oscillation frequency is investigated in an empirical way, with the generated electron beam for two different cathode materials and each anode-cathode gap as significant physical quantities to be considered.

2. Experimental Setup

Figure 1 shows a schematic configuration of the experimental apparatus for the reflex triode vircator. A Marx generator with the stored energy of 240 J is used to drive the electron beam diode. The Marx generator is comprised of four-stage incorporating capacitors charged up to 50 kV, charging resistors for the capacitors and SF₆-filled field-distortion gap switches. The high-voltage positive pulse is applied to the anode of the electron beam diode. In the experiment the vacuum chamber is maintained at a vacuum level of 6.6×10^{-3} Pa with a diffusion pump package. The diode

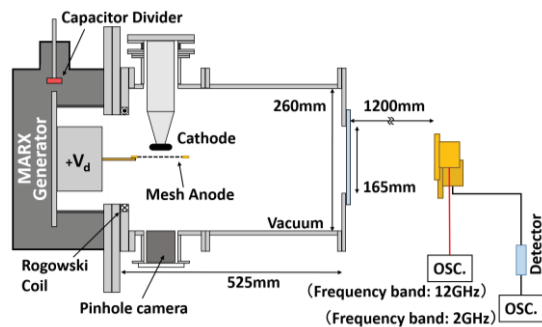


Fig. 1 Schematic configuration of Reflex Triode vircator

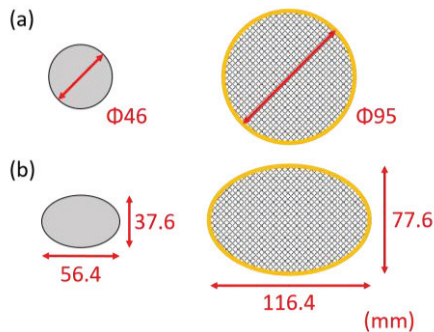


Fig. 2 Schematic diagram of (a) Circular electrode and (b) Elliptic electrode used in Reflex Triode vircator

voltage (V_d) and diode current (I_d) are measured by the capacitive voltage divider installed inside the Marx generator and Rogowski coil, respectively (see Fig. 1).

The electron beam diode consists of a pseudo-Rogowski type cathode and a meshed anode. Figure 2 shows a schematic diagram of the anode and cathode electrodes used in this experiment. Two types of electrode facing shapes, circular and elliptic types, were used. The elliptic electrode has the aspect ratio of 2:3. The two are equal in electron emission area at 1662 mm². Aluminum and velvet-surface cathodes were used as the electron emitter. The anode is a stainless-steel mesh with a transparency of 64.5 % and attached to a brass holder, which is consistent through all experiments. In these experiments, the gap distance (d_{AK}) between the anode and cathode electrodes was changed from 4 to 9 mm with the step of 1 mm.

The microwave pulse from the vircator is emitted into a free space through an acrylic window. The pulse is received with an open-ended rectangle waveguide antenna (WR-187:3.95-5.85 GHz) located on the central axis at a distance of 120 cm from the output windows. The temporal waveform of the microwave was measured by a high-speed digital oscilloscope with a sampling rate of 40 GS/s and a frequency band of 12 GHz through a coaxial RF cable. The oscillation frequency of the emitted microwave was evaluated by the time-dependent frequency analysis (TFA) [9] of the received temporal waveform. The output microwave was also detected by using a crystal diode and recorded together with the diode voltage and current by a digital oscilloscope with a bandwidth of 200 MHz and a sampling rate of 2 GS/s.

The X-ray radiated from the anode due to electron bombardment was measured by an X-ray pinhole camera in order to evaluate the cross-section of the electron beam. The X-ray pinhole camera comprises a beryllium window with a pinhole diameter of 0.6 mm and the film and was installed inside the vacuum vessel.

3. Results and Discussion

3.1 Typical waveforms

Figure 3 shows the typical waveforms of the diode

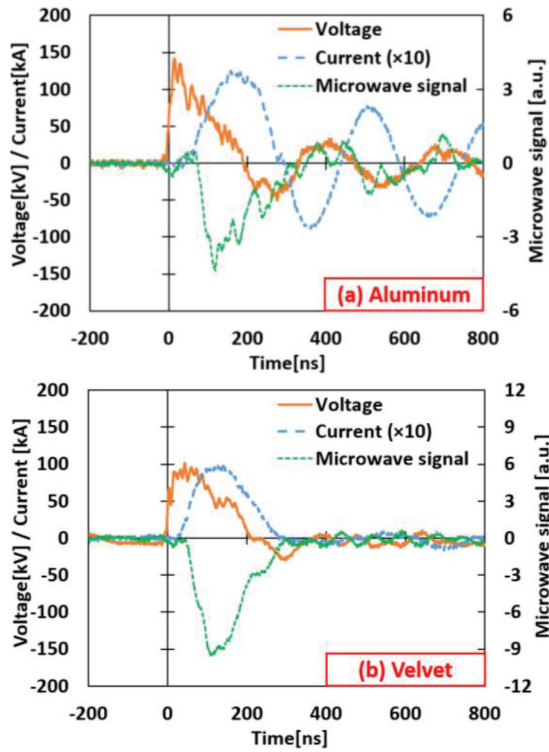


Fig. 3 Typical waveforms of diode voltage, diode current, and signal of output microwave recorded by diode detector for (a) aluminum and (b) velvet cathodes, where electrode shape and gap distance are ellipse and $d_{AK} = 5$ mm, respectively.

voltage, the diode current, and the signal of the output microwave recorded by the diode detector for the aluminum and velvet cathodes, where the electrode and the gap distance have the elliptic shape and $d_{AK} =$

5 mm, respectively. At both electrode materials, the diode current rises when the diode voltage reaches its peak. The microwave was emitted after the rise of the diode current and observed during the first oscillation period of the current. At the elliptic electrode, the discharge characteristics were similar to those of the circular electrode for each electrode material. The diode current oscillates at the aluminum electrode, but does not at the velvet electrode. However, even at the velvet electrode with the narrower gap distance of $d_{AK} \leq 4$ mm, the diode current oscillates like at the aluminum electrode. This is considered to be due to the change of the discharge parameters between the electrodes.

3.2 Oscillation frequency

The time-dependent frequency analysis (TFA) was carried out to obtain the time variation of the microwave spectrum. Figure 4 shows the results of TFA for two different electrode materials (aluminum and velvet) and the elliptic and circular electrodes, where the gap distance d_{AK} are set to 5 and 7 mm, respectively.

As shown in Figs. 4(a) and 4(b), for the velvet electrode, there is a frequency shift up in the rise time during microwave radiation, but it remains almost constant at 5 GHz. On the other hand, for the aluminum electrode (Fig. 4(c) a), we can see a shift up with time. The conditions under which this frequency shift-up occurred were the same as the conditions that caused the oscillation of the typical waveform shown in section 3.1. From these results, it is clear that the

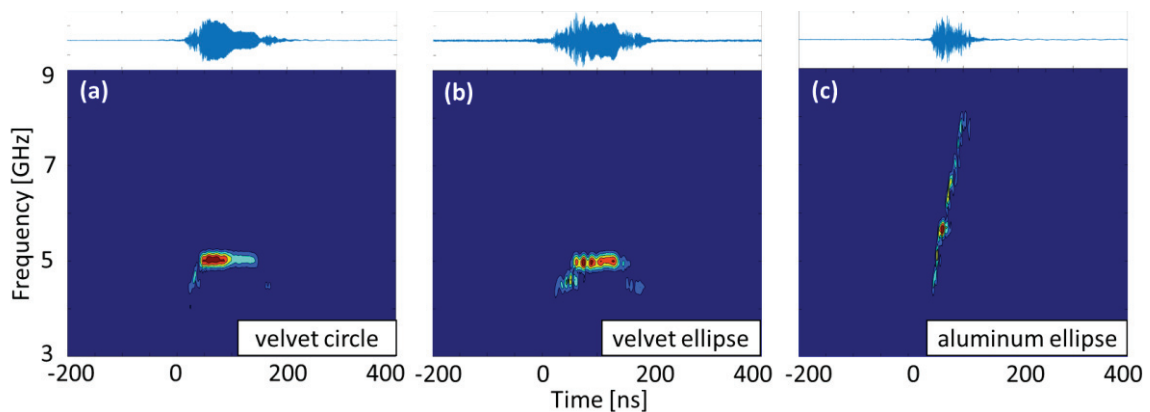


Fig. 4 TFA results for (a) velvet circle cathode, and $d_{AK} = 7$ mm, (b) velvet ellipse cathode, and $d_{AK} = 7$ mm, (c) aluminum ellipse cathode, and $d_{AK} = 5$ mm. Top and side views show the waveform of microwave pulse and the corresponding FFT, respectively.

oscillation frequency is not affected by the electrode shape, but is greatly affected by the electrode material.

3.3 Electric field strength

Figure 5 shows the relative electric field strength of the emitted microwave as a function of the gap distance for the circular and elliptic electrodes and for the aluminum and velvet materials. The maximum power at the aluminum and velvet electrodes were obtained at $d_{AK}=5$ mm and $d_{AK}=6-7$ mm, respectively. It is found that the strength is higher at the velvet electrode than at the aluminum electrode. In this experiment, although the circular and elliptic electrodes are designed to have the same electron emitting area, the strength at the elliptic electrode is about 1.3 times as large as at the circular electrode.

The gap distance dependence of the microwave power for the orientation of the velvet elliptic electrode is also shown in Fig. 5. It turns out from these results that the strength for the long axis is slightly higher than for the short axis and that the dependence of the gap distance on the strength is the almost same at the two orientations of the elliptic electrode. Thus, the strength of the emitted microwave does not depend on the orientation of the elliptic electrode.

From the above-mentioned results, the electrode orientation due to the asymmetry does not significantly affect the frequency and the power of the emitted microwave. The most important point is that the RT type vircator with the elliptic electrode can

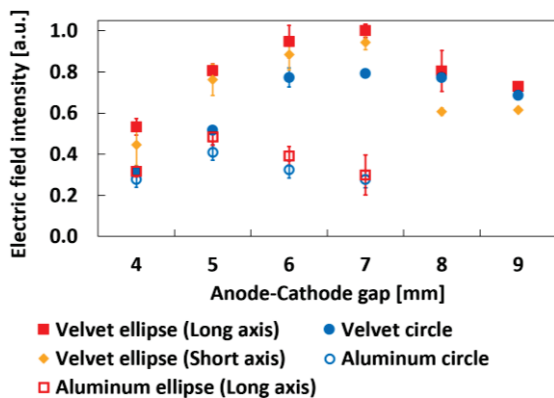


Fig. 5 Peak power of microwave as a function of gap distance for circular and elliptic electrodes and for aluminum and velvet materials.

generate higher microwaves than that with the circular electrode, which suggests the new possibility for improvement of the conversion efficiency.

3.4 Electron beam shape

Figure 6 shows the X-ray photograph recorded by the pinhole camera with a beryllium window. Five shots were made for each velvet circular and velvet elliptic electrode. The gap distance was $d_{AK} = 5$ mm. The yellow mark in the image indicates the outline of the X-ray image, i.e., the profile of electron beam bombardment on the anode. The flattening f is used as the index to evaluate the distortion of the X-ray image and $f = 0$ at a perfect circle. The X-ray image at the circular electrode (Fig. 6(a)) has the flattening of $f = 0.04$ and the area of about 50 mm^2 on the image. The X-ray images at the elliptic electrode (Figs. 6(b)) have the flattening of $f = 0.16$ and the area of about 58 mm^2 on the image, respectively.

It is confirmed from these results that the cross-section of the electron beam has the similar shape as the cathode electrode. The flattening of the elliptic beam became smaller than the cathode electrode of $f = 0.33$, which shows that the cross-sectional shape of the electron beam gets closer to a circle. Furthermore, the cross-sectional area of the electron beam was larger in elliptical than in circular shapes. The difference in the electron beam, which is an important factor in microwave oscillation, is considered to be a major factor in changing the characteristics of microwaves.

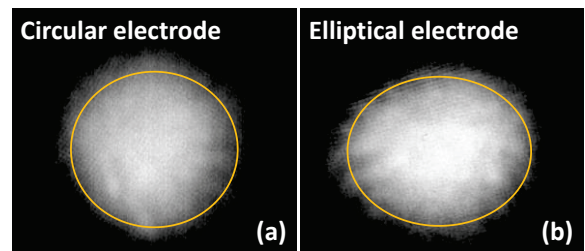


Fig. 6 X-ray pinhole photograph on anode at (a) velvet circular electrode and (b) velvet elliptical electrode. The gap distance is $d_{AK} = 7$ mm.

4. Conclusions

In this study, we evaluated the dependence of the

electron beam shape on the microwave radiated from RT vircator and the X-ray pinhole image due to the electron beam by using the circular and elliptic electrodes for two different cathode materials. The oscillation frequency did not make a difference between the circular and elliptic electrodes. In both electrodes, the frequency can be controlled stably by using the velvet cathode, however, the frequency rises with time during the microwave radiation. From the relative evaluation results of the electric field strength, it was evident that the higher microwave power was obtained at each AK gap by using the elliptic electrode. In this device, the highest microwave was observed at the velvet elliptic electrode with the AK gap of $d_{AK}=7$ mm. The X-ray pinhole image shows that the elliptical electron beam extends more in the direction of the elliptical minor axis than the cathode.

From these results, we conclude that the electrode geometry has a significant effect on the oscillating microwaves.

Acknowledgement

This work was partially supported by JSPS KAKENHI Grant Number JP19H02126.

References

- [1] J. Benford, "Space Applications of High-Power Microwaves," *IEEE Trans. Plasma Sci.* **36**, 569–581 (2008).
- [2] J. Benford, J. Swegle, and E. Schamiloglu, *High Power Microwaves*, 2nd ed. (Taylor & Francis, Boca Raton, 2007).
- [3] L. E. Thode, "Virtual cathode microwave device research: Experiment and simulation," in *High Power Microwave Sources*, edited by V. Granastein and I. Alexeff (Artech House, Norwood, 1987).
- [4] L. Li, L. Liu, X. Zhang, J. Wen, H. Wan, and Y. Zhang, "Efficiency Enhancement of Reflex Triode Virtual Cathode Oscillator Using the Carbon Fiber Cathode," *IEEE Trans. Plasma Sci.* **35**, 361-368 (2007).
- [5] V. Baryshevsky, A. Gurinovich, E. Gurnevich, and P. Molchanov, "Experimental Study of a Triode Reflex Geometry Vircator," *IEEE Trans. Plasma Sci.* **45**, 631-635 (2017).
- [6] A. Saxena, N. M. Singh, Y. Shambharkar, F. Kazi, "Modeling of Reflex Triode Virtual Cathode Oscillator," *IEEE Trans. Plasma Sci.* **42**, 1509-1514 (2014).
- [7] P. Appelgren, M. Akyuz, M. Elfsberg, T. Hurtig, A. Larsson, S. E. Nyholm, and C. Möller, "Study of a compact HPM system with a reflex triode and a Marx generator," *IEEE Trans. Plasma Sci.* **34**, 1796-1805 (2006).
- [8] X. Chen, J. Dickens, J. Mankowski, L. L. Hatfield, E. H. Choi, M. Kristiansen, "Microwave Frequency Determination Mechanisms in a Coaxial Vircator," *IEEE Trans. Plasma Sci.* **32**, 1799-1804 (2004).
- [9] W. Jiang, "Time-frequency analysis of virtual cathode oscillator," *IEEE Trans. Plasma Sci.* **38**, 1325-1328 (2010).

Analysis of Observation Signal of Microwave Discharge in Rectangular Waveguide

T. Sugai, Z. Shaw*, J. Dickens*, A. Neuber*

Extreme Energy-Density Research Institute, Nagaoka University of Technology

**Center for Pulsed Power and Power Electronics, Texas Tech University*

ABSTRACT

Multipactor is a damaging RF discharge in vacuum caused by repeated secondary emission of electrons. In previous experiments, multipactor was directly observed in a copper waveguide of 2.1 mm height via an integrated electron multiplier tube (EMT) setup. The detected multipactor signal was analyzed using a numerical simulator “Spark3D” with the same geometry and conditions as the experiment. For the simulation, a SEY (secondary emission yield) curve, whose first crossover with $SEY = 1$ was adjusted based on experimental multipactor threshold value, was imported into Spark3D. The rising slope of the experimental EMT signals was reproduced in the simulation and exhibited the same microwave power dependence. Overall, the simulated/experimental signal is consistent with the simulated average SEY and multipactor order. Thus, electron energy and electron motion expressed in the Spark3D are deemed accurate, and the imported SEY is considered close to the actual SEY of the wall material found in the experiment.

Keywords

Multipactor, High power microwave, Electric discharge, Vacuum

1. Introduction

High power microwave radiation has found use in various applications, e.g., satellite, accelerator, fusion, radar, etc. In these applications, microwaves are transmitted via vacuum region, i.e., a waveguide or cavity in vacuum, or space. The associated high microwave electric field and the large electron mean free path make secondary electron emission possible due to the impact of primary electrons on metallic or dielectric boundaries. Further, within particular physical conditions, electron impact and emission are repeated, resulting in electron multiplication. This phenomenon is called multipactor, MP, and brings negative effects for the aforementioned applications, introducing undesired phase noise, detuning of resonant cavities, power loss, or physical damage. In addition to preventing the negative effects, a fundamental physics interest has fostered many multipactor studies. Thus, credible MP theory has been

developed, and many numerical simulations were carried out^{[1],[2]}. On the other hand, MP diagnostics was chiefly focused on detecting the occurrence of multipactor, and a quantitative evaluation of the multiplication ratio and MP electron density found little attention.

Previously, we have suggested and carried out a direct electron multiplication observation method using electron multiplier tube (EMT) and succeeded in obtaining direct MP signals^[3]. In this study, we evaluated the multiplication ratio, secondary emission yield (SEY), and order quantitatively from the EMT signal, using the numerical simulation software “Spark3D”. This paper details the evaluation method and its result.

2. Multipactor Observation Experiment

In this section, the experimental method for direct observation of electron multiplication is outlined (See

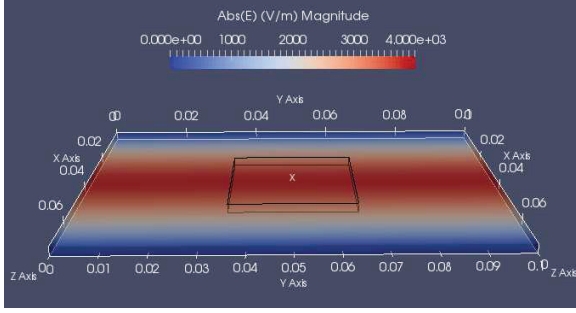


Fig. 1 A simulation model with RF field of 2.85 GHz-TE₁₀ mode (shown is the 10 cm long test section which is 2.1 mm tall and 7.2 cm wide; microwave propagation is from left to right in TE₁₀ mode). Color corresponds to the field magnitude. Multipactor was simulated in the black box region as indicated. The aperture position is marked with an “x” in the center of the geometry.

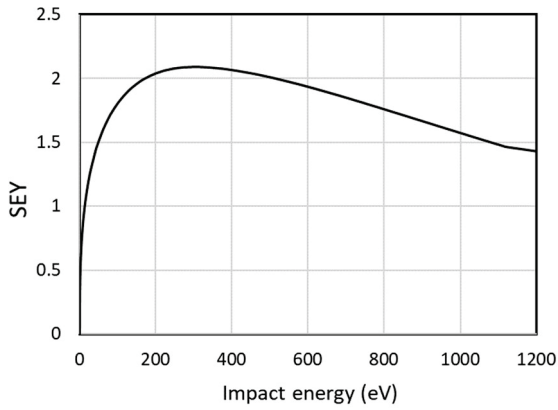


Fig. 2 SEY curve imported to Spark3D. First crossover point shifted from 47 eV [Baglin] to 13 eV.

[3] and [4] for more details). To cause MP at 2.85 GHz in TE₁₀ mode, the microwave output generated by a magnetron was delivered via WR284 rectangular waveguide into a rectangular copper test section whose height is 2.1 mm, that is same structure as a simulation model in Fig.1. At the center in the top, the broadside wall of the 2.1mm gap part, a 1mm aperture is located (Its position is marked as a “x” in Fig.1). An EMT is mounted above the aperture in the same continuing vacuum space such that a portion of the MP electrons at the center of the 2.1 mm gap enters the EMT, resulting in the output of the MP voltage signal.

3. Simulated EMT signal

For analysis of the experimental EMT signal, a theoretical EMT signal was obtained via the extensive usage of the simulator “Spark3D” and was compared with the experiment. The method of obtaining the theoretical EMT signal is provided below.

3.1 Simulation model

Spark3D computes MP based on the microwave RF field and the SEY curve, both imported from other software. The simulation model shown in Fig.1 has the same geometry as the experimental test piece and includes RF field of 2.85Gz-TE₁₀ mode whose power is set by the user. To focus on the location of the EMT probe aperture, the simulation region was restricted in a box region in Fig.1, where the RF field is almost constant spatially. For the SEY curve import, a SEY curve was drawn initially using the parametric model of Vaughan^[5], using the maximum SEY and its impact energy of an as-received/untreated copper surface, obtained from the experiment by Baglin et al.^[6]. Subsequently, the first crossover with SEY = 1 was shifted to the point at which the simulated multipactor threshold became 2.25 kW, which matched the experimental value, resulting in the SEY curve in Fig.2.

3.2 Derivation of theoretical EMT signal

Through extensive usage of Spark3D, the number of electrons as a function of time, $N_e(t)$, and the temporally and spatially averaged SEY (σ_{Ave}), in the model region, were obtained^[7] and were substituted into the following equations for deriving the theoretical EMT signals.

Generally, the number of electrons is expressed by

$$\begin{aligned} N_e(t) &= \sum_{k=1}^m (c_k - n_k) \Delta S \\ &= \sum_{k=1}^m (\sigma_k \cdot n_k - n_k) \Delta S, \end{aligned} \quad (1)$$

where c_k , n_k , σ_k are time-integrated densities of emission electrons, impact electrons, and SEY, respectively, for a k th small area of size ΔS . Averaging n_k spatially, converts Eq. (1) to

$$N_e(t) = N_{Imp}(t)(\sigma_{Ave} - 1), \quad (2)$$

where $N_{Imp}(t)$ is the total number of impacting electrons, which results in an impact current $I_{Imp}(t)$ expressed by

$$I_{Imp}(t) = e \frac{dN_{Imp}(t)}{dt}. \quad (3)$$

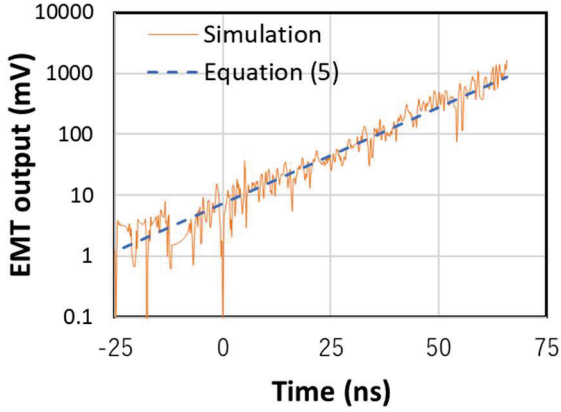


Fig. 3 Voltage evolution simulated EMT and Equation (5)

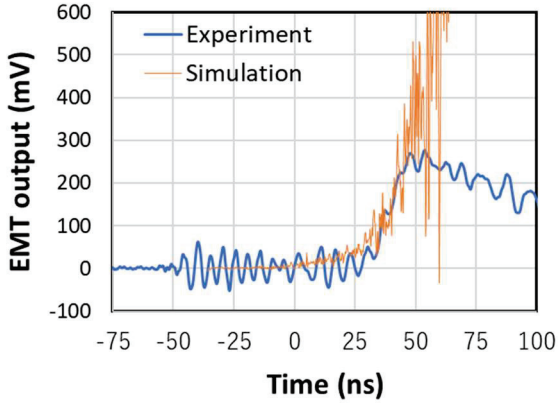


Fig. 4 Experimental and simulated EMT voltage waveforms

Assuming that impact current is constant spatially, the ratio of the EMT cathode current to the whole impact current is the same as the ratio of the aperture area to the surface area of one side of MP gap. Thus, the anode current of the EMT is expressed by

$$I_{EMT}(t) = G \frac{s_a}{S/2} I_{imp}(t), \quad (4)$$

where $I_{EMT}(t)$ is the anode current of the EMT, G is EMT gain ($\sim 5 \times 10^5$), s_a is area of 1 mm aperture, and S is the total surface area of both sides of multipactor gap. Note that the aperture is not included in the simulation model so that the decrease of electron density at the local place close to the aperture is not considered. Finally, the theoretical EMT voltage signal is obtained from the product of $I_{EMT}(t)$ and the 50Ω termination resistance of the diagnostics.

4. Simulation Result and Comparison with Experiment

4.1 EMT voltage evolution

The simulated EMT voltage evolution of multipactor by the microwave of input power 2.25 kW, obtained by the method of Section 3, is shown in Fig.3. Meanwhile the simulation showed 1.07 and 5.63 of average SEY and average order, respectively. The order means the number of half cycles between consecutive electron impacts. Using the averaged values, another voltage evolution line expressed by a general multipactor equation was added to Fig. 3, that is,

$$V_{EMT}(t) = V_{EMT}(0) \sigma_{Ave}^{2ft/\delta_{Ave}} \quad (5)$$

where f is frequency of input microwave and δ_{Ave} is average order. Both lines in Fig.3 are similar in slope, which indicates that the simulated EMT signal is consistent with the simulated SEY and order.

4.2 Comparison of evolution time with experiment

Noting that the simulation ignores saturation effects and that the experimental setup was intentionally designed to be highly sensitive to MP, a comparison between simulated and experimental signal is depicted in Fig.4. The rising edge of the experimental EMT signal pulses fits well with the simulated one. Further, the experimental threshold of multipactor breakdown is also consistent with the simulation. Thus, the electron energy and electron motion expressed in the Spark3D is deemed accurate, and the adjusted SEY is close to the actual SEY of the wall material in the experiment.

Beyond 50 ns, the experimental signal ceases growth due to the MP's effect on the sensitive experimental setup, and a direct comparison is no longer possible.

5. Conclusion

To analyze the experimental signal of the directly observed multipactor, expected theoretical values were obtained from the software "Spark3D". By slightly adjusting the SEY curve imported to Spark3D, the signal rising shape and threshold value in the experiment were consistent with those of the simulation. It proves the accuracy of the electron

energy and electron motion expressed in the Spark3D and the SEY. Overall, the simulated signal is consistent with the simulated average SEY and multipactor order. In general, through comparison of the experimental direct observation signal with Spark3D simulation results, one is expected to identify SEY curves for wall materials other than the copper discussed here.

References

- [1] R. A. Kishek, Y. Y. Lau, L. K. Ang, A. Valfells, and R. M. Gilgenbach, “Multipactor discharge on metals and dielectrics: Historical review and recent theories”, *Phys. Plasmas.*, **5**, 5, pp.2120–2126 (1998).
- [2] Valery D. Shemelin and Segey A. Belomestnykh, “Multipactor in accelerating cavities”, *Springer*, (2020).
- [3] Z. C. Shaw, A. Garcia, M. Powell, J. C. Dickens, J. J. Mankowski, and A. A. Neuber, “Direct observation of electrons in microwave vacuum components”, *Rev. Sci. Instrument.*, **90**, 5, 054702 (2019).
- [4] Z. Shaw, L. Silvestre, T. Sugai, B. Esser, J. Mankowski, J. Dickens, and A. Neuber, “On the limits of multipactor in rectangular waveguides”, *Phys. Plasmas*, **27**, 8, 083512 (2020).
- [5] J. Rodney and M. Vaughan, “A new formula for secondary emission yield”, *IEEE Trans. Electron Devices*, **27**, 8, 083512 (2020).
- [6] V. Baglin et al, “The secondary electron yield of technical materials and its variation with surface treatments”, in *Proc. EPAC*, p. 217 (2000).
- [7] T. Sugai, Z. Shaw, J. Dickens, and A. Neuber, “Analysis of multipactor in a rectangular waveguide using Spark3D software”, *Phys. Plasmas*, **27**, 11, 112108 (2020).

Droop Compensation in Marx generator

Shonosuke Matsumoto, Taichi Sugai, Akira Tokuchi, Weihua Jiang

*Extreme Energy-Density Research Institute pulsed power Japan Laboratory Ltd,
Nagaoka University of Technology*

ABSTRACT

In general, the Marx generator has a problem of a voltage decrease pronounced droop when relatively long pulse is output. There are several ways to compensate for droop, such as increasing the capacitor capacitance or using a chopper-type circuit. In this paper, we will introduce a compensation method by incorporating a CLC capacitance transfer circuit into a Marx generator to investigate its characteristics, aiming at droop compensation for small devices. In the CLC capacitance transition circuit. The sine waveform created by the CLC capacitance and is to the droop waveform created by the Marx circuit to achieve a flat waveform output. The circuit is built actually, set the switch timing and element values appropriately, and tested. We confirmed that the circuit improved the droop from about 25 % to about 8 %.

Keywords

Marx generator, droop, CLC capacitance transfer circuit.

1. Introduction

One of the conventional pulsed power generators is the Marx generator. The Marx generator obtains pulse output by parallel charging and series connection of capacitors. When the Marx generator has a relatively long pulse width it has the problem of a droop. In some pulse applications, a flat pulse shape is required, consequently this droop compensation is important to

expand the application. There are several methods of compensation, such as increasing the capacitor capacitance or using a chopper type, but these methods are not suitable for small devices. Therefore, we propose a new Marx generator incorporating a CLC capacitance transfer circuit as a droop compensation for small devices.

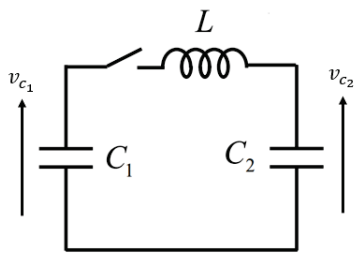


Fig. 1 CLC capacitance transfer circuit

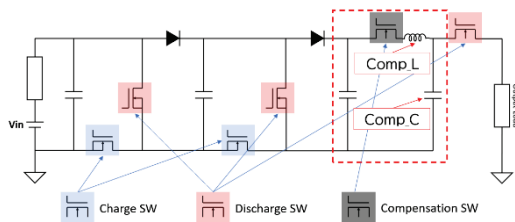


Fig. 2 Marx generator with embedded CLC capacitance transfer circuit

2. CLC capacitance transfer circuit

In Figure 1, after C1 is charged, when the switch is turned on, C2 starts to change, according to the following time function.

$$v_{c_2} = V_0 \left[\frac{C_1}{C_1 + C_2} (1 - \cos \omega_0 t) \right]$$

In other words, the output is a sine wave. By taking a portion of this sine wave and combining it with a droop waveform, we aim to create a flat waveform.

3. Circuit configuration

Figure 2 shows the CLC capacitance transition circuit incorporated into the final stage of the Marx generation circuit.

4. Results and Discussion

First, we checked the droop without the CLC capacitance transfer circuit, which serves as the compensation stage. Figure 3 shows the waveforms of three output stages under the conditions of 500V input voltage, 2.5 μs pulse width, 98 Ω load resistance, and 1 μF charging capacitor. As a result, we confirmed a droop of about 25 %.

Next, we conducted an experiment using the compensation stage. Figure 4 shows the 3-stage output waveform when the switch timing was set to be the flattest under the conditions of 500 V input voltage, 2.5 μs pulse width, 98 Ω load resistance, 1 μF charging capacitor, 0.44 μF compensation capacitor, and 13 μH compensation inductor. In this case, it was confirmed that the droop was reduced to about 8 % compared to the case without compensation.

In order to reduce it further, more appropriate elements should be selected. Also, since droop compensation has been confirmed only for a single output, it is necessary to consider how to deal with repeated outputs. In order to do so, it is necessary to completely discharge the capacitor between shots, so it is necessary to consider connected C1 in parallel of a resistor.

4. Conclusions

In this study, a CLC capacitance transfer circuit was incorporated into a Marx generator to investigate its characteristics for pulse-droop compensation for small Marx devices. Without compensation, 25 % droop was observed, but after compensation, it was reduced to 8 %. However, more appropriate device selection is needed to generate a flatter waveform. In addition, it is necessary to support not only one-shot output but also repetitive output in the future.

References

- [1] Yuki Kozaka, Sho Sato, Weihua Jiang, Akira Tokuchi, Mitsuo Akemoto, Hiromitsu Nakajima : “HIGH SPPED SWITCHING CIRCUITS FOR FUTURE ACCELERATORS”, 10th Annual Meeting of Particle Accelerator Society of Japan, pp.1028-1032(2013)

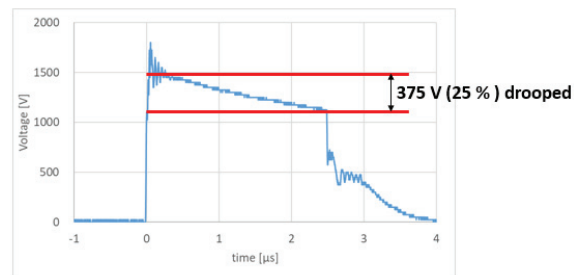


Fig. 3 3-stage output waveform without compensation

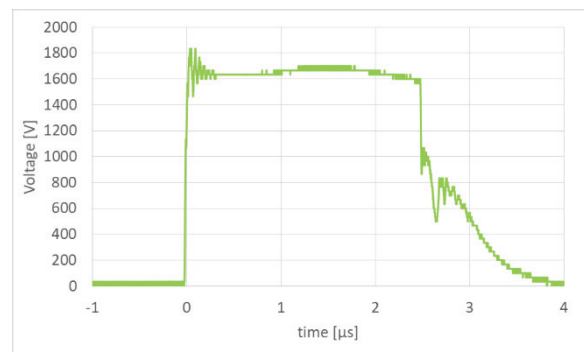


Fig. 4 3-stage output waveform with compensation

Development and evaluation of bipolar Marx circuits

Nguyen Huu Phat, Akira Kamada, Xiaojing Ren, Taichi Sugai, Akira Tokuchi*
and Weihua Jiang

Extreme Energy-Density Research Institute, Nagaoka University of Technology

** Pulsed Power Japan Laboratory Ltd.*

ABSTRACT

Based on full bridge circuit switching topology a type of bipolar Marx generator is shown in this paper. By using semiconductor devices as switches, this type of bipolar Marx generator can generalize both positive and negative pulses whose width, frequency, relaxation time between the positive and negative pulse and number per period are adjustable.

Keywords

MOSFET, bipolar, Marx generator, Pulsed power, FPGA

1. Introduction

Recently, pulsed power is used in many applications as wastewater processing, air-pollution control, laser excitation, and discharge physics research etc. To meet the demands of pulsed power applications, the Marx type pulsed power generators become to be used and developed more. Marx generators can generate a high voltage pulse from a low voltage DC supply by switching capacitor connection from parallel to series. Output voltage depends on the number of Marx stages. In addition, in some applications such as food processing and medical applications, the use of bipolar pulses is expected to bring higher efficiency. Thus, the development of bipolar pulse generators is necessary. Bipolar pulse voltages can be generated by the on-off process of switches, based on the Marx generators topology [1] [2]. In this article a bipolar Marx circuit using the principle of full-bridge circuit, detailed in Fig. 1 is introduced.

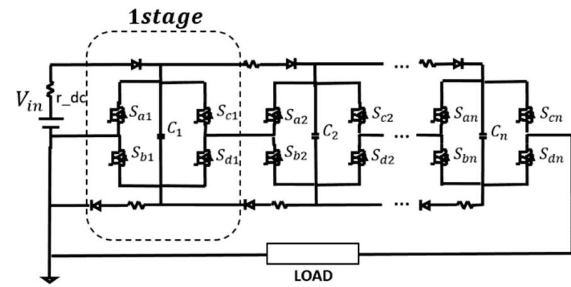


Fig. 1 Bipolar Marx generator based on full – bridge circuit

2. Experimental Setup

2.1 Circuit operation

The circuit in Fig.1 presents several operating modes depending on the semiconductor switching sequence and the required output into the load. During the capacitors C_i charging period all switches are off, as shown in Fig.2.

For negative pulse mode, switches S_{bi} and S_{ci} are on, as shown in Fig.3(a), and for positive pulse mode, switches S_{ai} and S_{di} are on as shown in Fig.3(b). During on period, capacitors C_i are connected in series and the voltage applied to the load is nearly $\pm nV_{in}$.

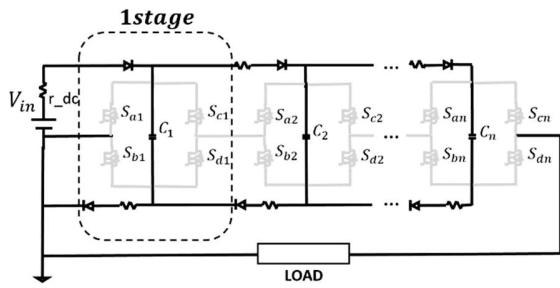
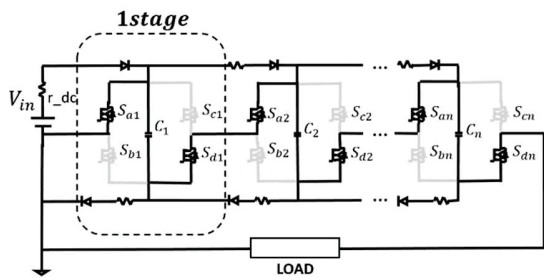
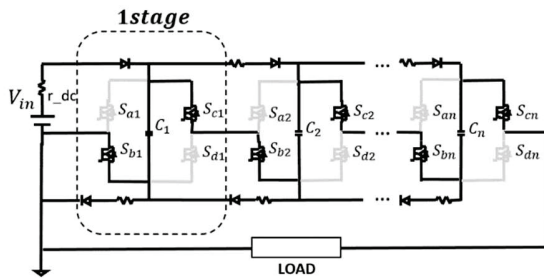


Fig. 2 Circuit in charged mode



(a)



(b)

Fig. 3 Bipolar Marx generator based on a) Positive pulse and b) Negative pulse

The time interval between the negative and positive pulses, called the relaxation time, can be adjusted. Otherwise the negative and positive pulse amplitudes are not always equal due to the voltage droop.

2.2 Simulation result

In order to confirm the operation of the circuit as well as to check the switching time of the switches, the circuit operation was simulated by the LTspice. The simulation conditions are input voltage $V_{in}=1000$ V, load resistor $R_L=2$ k Ω , and pulse width $pw=5$ μs . Simulation results are shown in Fig.4.

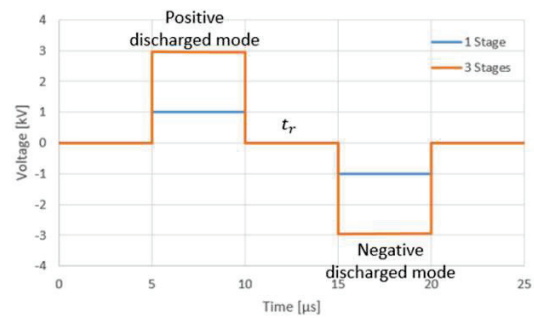


Fig. 4 LTspice simulation results

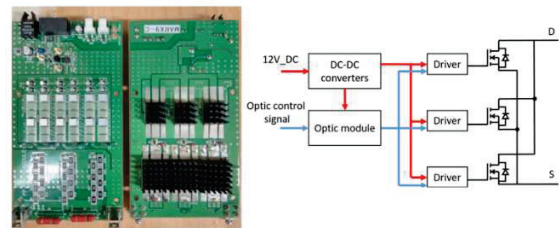


Fig. 5 Switching board used in experiment

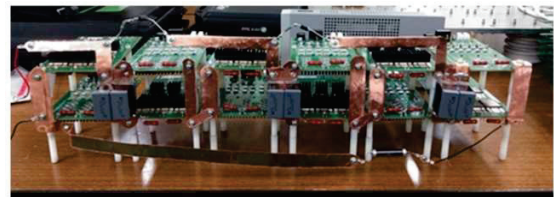


Fig. 6 Three stages bipolar Marx generator circuit

2.3 Experimental equipment

Regarding the equipment used for this experiment, a switching board shown in Fig.5 was used because of the ability of switching quickly as well as respond to high frequencies. The board includes three MOSFET (DE475-102N21A) connected in parallel, and three drivers (IXRFD630) connecting to each MOSFET. For a 3-stage test circuit, 12 switching boards are used and arranged as shown in Fig.6.

Regarding the switch circuit with the condition of $V_i=1000$ V and load resistor $R_L=2.3$ k Ω , the rise-time and fall-time of the switch circuit are ~ 10 ns and ~ 3 μs , respectively, shown in Fig.7.

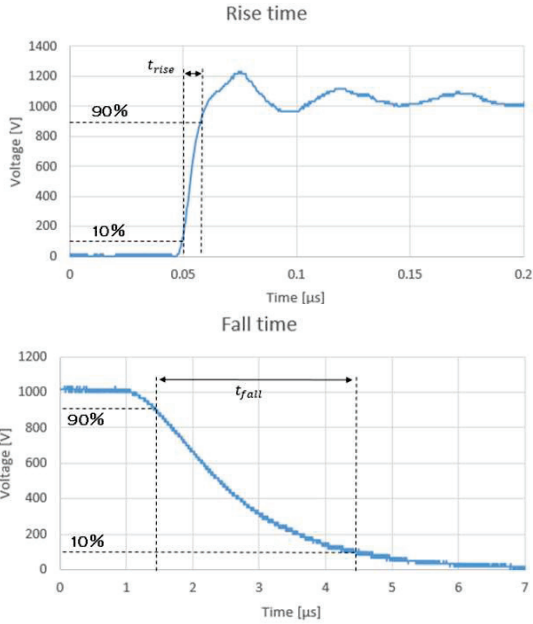


Fig. 7 Rise-time and fall-time by the switching board

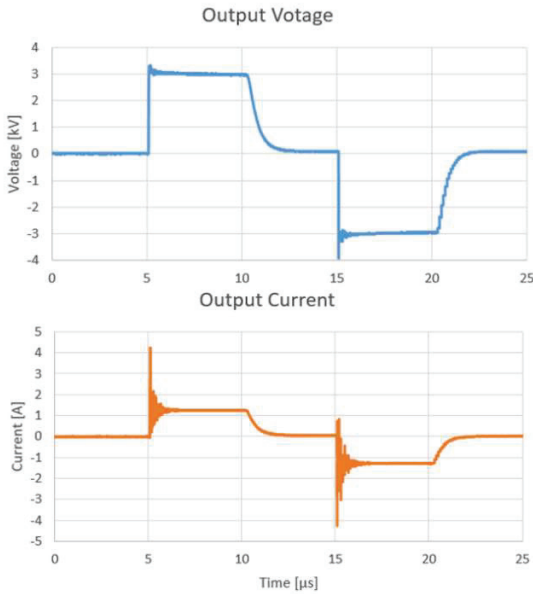


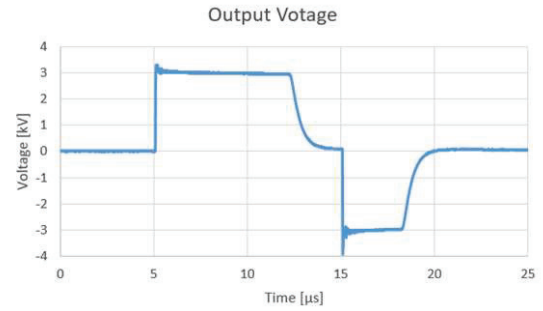
Fig. 8 Three stages bipolar Marx generator output

3. Results and Discussion

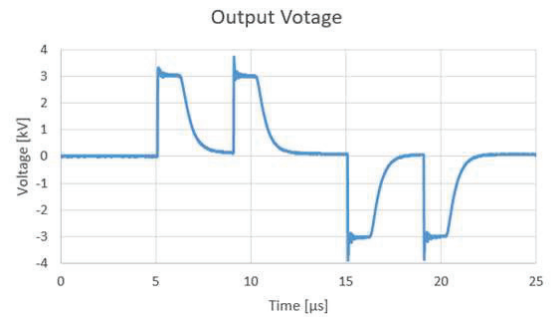
3.1 Output voltage and current

Using the circuit as shown in figure 6 with the experimental conditions $V_f=1000$ V, load resistor $R_L=2$ k Ω , and pulse width $pw=5$ μ s, the waveforms of voltage and current shown in Fig.8 were obtained.

The output voltage is 3 times higher than the supply voltage. The fall-time delay occurs due to the characteristics of the switch board.



a) Different pulse width



b) Double pulse

Fig. 9 Various types of output waveform

3.2 Output voltage waveform adjusted by FPGA

a. Pulse shape adjustment

Based on the principle of operation of the circuit, the pulse width is determined by the switch-on time and the pulse shape is also determined by combination of on-off of the switch. In this way it is possible to customize the output pulse waveform according to the required response.

To adjust switching, FPGA was used. FPGA is very convenient since switching process can be changed quickly by adjusting the parameters in programming codes.

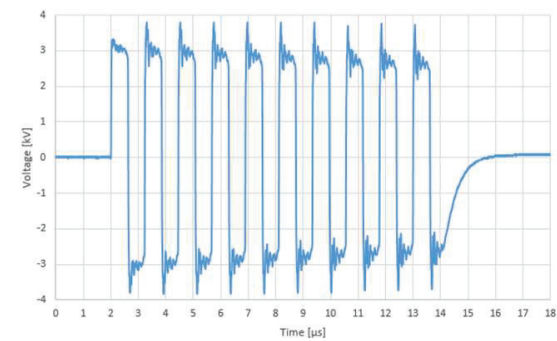
Under the above experimental conditions, test experiments on varying pulse width and number of pulses were performed. The results of the experiment are shown in Fig.9.

b. Burst mode

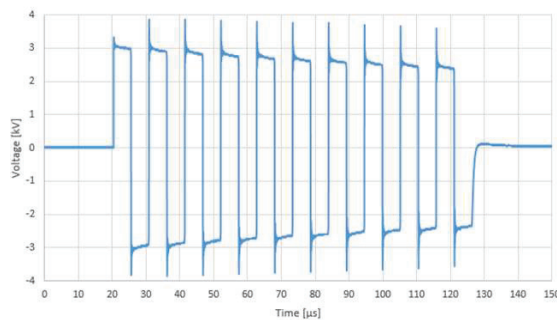
In some applications such as laser excitation or medical application, burst output is needed[3]. Burst is a waveform consisting of several pulses produced in succession. By using FPGA to adjust on-off timing of the switch, the number of pulses as well as the

frequency of the burst was adjusted. Experimental results for burst mode are shown in Fig.10. The slower fall-time seen in the last pulse is due to the characteristic of the switch.

By using fast switchable switches as well as using program to adjust the on and off time of the switches, we can customize the output pulse of the bipolar generator circuit as desired.



(a)



(b)

Fig. 10 10 pulse burst output by bipolar Marx circuit ($V_{in}=1000$ V) (a): 833.3 kHz and (b): 100 kHz

4. Conclusion

We suggested the one of the bipolar pulsed power generator. Through the usage of software such as FPGA, it is possible to control the on-off timing of the switches and then customize the output pulse waveform. However, the circuit still has had problems to improve for practical applications, which are voltage droop and circuit size etc. We will attempt to solve in future.

References

- [1] L. M. Redondo, H. Canacsinh and J. Fernando Silva et al., “Generalized Solid-state Marx Modulator Topology”, *IEEE Transactions on Dielectrics and Electrical Insulation Vol. 16, No. 4* (2009).
- [2] Rashmi V. Chaugule, Ruchi Harchandani , Bindu S. et al., “Solid state Bipolar Marx Generator Topologies: A Comparative study”, *Fr. C.R. Institute of Technology, Sector - 9A, Vashi, Navi Mumbai – 400 703* (2015).
- [3] L. M. Redondo et al., “Solid-State Generation of High-Frequency Burst of Bipolar Pulses for Medical Applications”, *IEEE TRANSACTIONS ON PLASMA SCIENCE*.

Publication List of NIFS-PROC. Series

- NIFS-PROC-106 Edited by Keiichi Kamada and Tetsuo Ozaki
Evolution of Pulse Power and its Peripheral Technology
Nov. 01, 2017
- NIFS-PROC-107 Edited by Hiroaki Ito and Tetsuo Ozaki
Recent Progress of Pulsed Power Technology and its Application to High Energy Density Plasma
Nov. 27, 2017
- NIFS-PROC-108 Edited by Yeong-Kook OH, Shigeru MORITA and Liqun HU
Proceeding of A3 Foresight Program Seminar on Critical Physics Issues Specific to Steady State Sustainment of High-Performance Plasmas November 22-25, 2016, Jeju, Korea
Jan. 11., 2018
- NIFS-PROC-109 Edited by Shigeru MORITA, Liqun HU and Yeong-Kook OH
Proceeding of A3 Foresight Program Seminar on Critical Physics Issues Specific to Steady State Sustainment of High Performance Plasmas 11-14 July, 2017, Sapporo, Japan
Jan. 12, 2018
- NIFS-PROC-110 Edited by Jun Hasegawa and Tetsuo Ozaki
Recent Developments of Pulsed Power Technology and Plasma Application Research
Jan. 12, 2018
- NIFS-PROC-111 Edited by Liqun HU, Shigeru MORITA and Yeong-Kook OH
Proceeding of A3 Foresight Program Seminar on Critical Physics Issues Specific to Steady State Sustainment of High Performance Plasmas 12 - 15 December, 2017, Chongqing, China
Jun. 11, 2018
- NIFS-PROC-112 Edited by E. Kikutani (KEK) and S. Kubo (NIFS)
Proceedings of the meeting on Archives in Fields of Natural Sciences in FY 2017
Oct. 18, 2018 (Written in Japanese)
- NIFS-PROC-113 Pulsed Power and High-Density Plasma and its Applications
Edited by Koichi Takaki and Tetsuo Ozaki
Feb. 6, 2019
- NIFS-PROC-114 The 7th Japan-China-Korea Joint Seminar on Atomic and Molecular Processes in Plasma (AMPP2018)
Edited by Daiji Kato, Ling Zhang, and Xiaobin Ding
May 10, 2019
- NIFS-PROC-115 CFQS TEAM
NIFS-SWJTU JOINT PROJECT FOR CFQS -PHYSICS AND ENGINEERING DESIGN-
VER. 2.1 2019. SEP.
Nov. 8, 2019
- NIFS-PROC-116 Satoshi Ohdachi, Editor of the Post-CUP Workshop proceeding
Collected papers at the 2019 Post-CUP Workshop & JSPS-CAS Bilateral Joint Research Projects Workshop,
24th-26th July, 2019, Nagoya, Japan
Feb. 21, 2020
- NIFS-PROC-117 Edited by E. Kikutani (KEK) and S. Kubo (NIFS)
Proceedings of the meetings on Archives in Fields of Natural Sciences in FY2018
June. 9, 2020 (Written in Japanese)
- NIFS-PROC-118 Edited by Tetsuo Ozaki and Sunao Katsuki
New Development of Beam Physics and the Application by New Generation Pulsed Power Technology
June. 29, 2020
National Institute for Fusion Science, National Institutes of Natural Sciences
Institute of Fusion Science, School of Physical Science and Technology, Southwest Jiaotong University
- NIFS-PROC-119 Hefei Keye Electro Physical Equipment Manufacturing Co. Ltd.
NIFS-SWJTU JOINT PROJECT FOR CFQS -PHYSICS AND ENGINEERING DESIGN-
VER. 3.1 2020. NOV.
Jan. 25, 2021
- NIFS-PROC-120 Edited by Izumi Tsutsui (KEK) and Shin Kubo (NIFS)
Proceedings of the meetings on Archives in Fields of Natural Sciences in FY2019
Feb. 25, 2021
- NIFS-PROC-121 Edited by Hiroaki Ito and Tetsuo Ozaki
Frontier of Advanced Pulsed Power Technology and its Application to Plasma and Particle Beam
Nov. 08, 2021